UC Berkeley
UC Berkeley Electronic Theses and Dissertations

Title

Adaptive Control Strategies in Systems with Nonprehensile Grippers

Permalink

https://escholarship.org/uc/item/9sc992qv

Author

Lee, Sebastian David

Publication Date

2024

Peer reviewed|Thesis/dissertation

Adaptive Control Strategies in Systems with Nonprehensile Grippers

by

Sebastian David Lee

A dissertation submitted in partial satisfaction of the

requirements for the degree of

Doctor of Philosophy

in

Engineering - Mechanical Engineering

in the

Graduate Division

of the

University of California, Berkeley

Committee in charge:

Professor Hannah Stuart, Co-chair
Professor Robert Full, Co-chair
Professor Ronald Fearing
Professor Koushil Sreenath

Summer 2024

Adaptive Control Strategies in Systems with Nonprehensile Grippers

Abstract

Adaptive Control Strategies in Systems with Nonprehensile Grippers

by

Sebastian David Lee

Doctor of Philosophy in Engineering - Mechanical Engineering

University of California, Berkeley

Professor Hannah Stuart, Co-chair

Professor Robert Full, Co-chair

This dissertation investigates adaptive control strategies for nonprehensile gripper contact in two distinct embodied systems: squirrels landing on branches and a suction cup haptically searching surfaces. Central to this work is the concept of embodied dexterity - the integration of morphological computation with adaptive control. Morphological computation leverages the body's design to assist in task execution, while adaptive control uses sensory input for real-time adjustments. Embodied dexterity is what enables agents to effectively interact with the physical world, where effective contact is crucial and varies with grasp type. Prehensile grasps for example, where the gripper wraps around the substrate, can rely on form closure, reducing the need for friction. However, nonprehensile grasps, necessary when the substrate is larger than the gripper, depend on high squeeze or suction forces for force closure, posing challenges in achieving contact stability.

The following studies highlight how positioning errors in grasping tasks can be dynamically compensated for by leveraging the physical design and sensory feedback of embodied agents, whether biological or robotic. I first present work on the biomechanics of squirrels landing on branches, examining their adaptive landing strategies. This includes their rapid forelimb dynamics to manage landing forces and torques. I also briefly introduce a squirrel-inspired gripper design. Next, I introduce the Smart Suction Cup and demonstrate how two tasks were accomplished with two different control algorithms. The first algorithm enhances grasping success on challenging surfaces by leveraging haptic signals, while the second enables contour-following.

To my family and friends

Acknowledgments

Contents

List of Figures

List of Tables

Chapter 1

Introduction

An embodied agent, whether biological or robotic, relies on its mechanical body and electrical signals to produce useful movements. For example, gecko feet naturally stick to smooth surfaces like glass due to their microfibrillar structure [2], but this utility can be compromised if the contact location is chosen poorly, i.e. contact on teflon, where gecko feet fail [3]. Fortunately, visual, proprioceptive, and tactile signals can be used to trigger reflexes that rectify contact placement and ensure robust behavior. This concept of using physical structure and sensory inputs to guide physical interactions can be described as embodied dexterity. It involves two key concepts: 1) morphological computation, where the body's design inherently assists in task execution, and 2) adaptive control, where sensory input informs real-time adjustments when morphological computation is insufficient.

When interacting with objects in the environment, embodied agents can leverage their body's design and sensory feedback to produce effective contact, which is a prerequisite for dexterous grasping and locomotion. The relative position between gripper and substrate is a particularly important factor that determines quality of contact. For instance, when a gripper is larger than the substrate, it can rely on form closure, i.e. geometrically constraining an object by wrapping around it, like a bird's feet around a branch or a hand around a hammer. This type of grasp - a prehensile grasp - can reduce or even negate the need for friction altogether [4]. However, wrapping may not be feasible when the substrate is substantially larger than the gripper. In these cases, grippers must rely on nonprehensile grasps, which instead require high squeeze and/or suction force for friction (force closure).

However, achieving force closure with a nonprehensile grasp is challenging. The inability to generate opposing forces leads to reduced contact stability and a higher risk of failure due to external wrenches from substrate weight, motion, or environmental disturbances. Nonprehensile contact presents unique constraints for grasping and locomotion, requiring innovative adaptive control strategies to dynamically compensate for positioning errors and external disturbances. Positioning errors are common in any grasping task. Due to unknown or noisy state information, an agent may not reach a target state or even reliably determine the correct target state, requiring real-time corrections upon contact. Dynamic behaviors in particular can be challenging due to the shorter time spans and higher forces.

1.1   Overview

A prime example of dynamic control can be found in tree-dwelling squirrels. Their acrobatic skills are evident in the way they navigate arboreal terrains with agility and ease [1]. A particularly impressive skill is their ability to jump and land upright on branches of varying sizes and orientations. Chapter 2 is dedicated to understanding the adaptive landing strategies of squirrels. Using a specialized field apparatus, I measured the dynamics of squirrel branch landing by recording landing forces, torques, and kinematics. By correlating landing kinematics with force-torque data, I show that squirrels adapt to different landing conditions, presumably through integration of sensory inputs. Additionally, I introduce a squirrel-inspired robotic gripper, demonstrating that for a set of landing conditions, morphological computation through foot design increases tolerance to positioning errors.

However, the capabilities of this design are clearly limited without sensing and adaptive control - a widespread limitation across robotic systems today. When it comes to embodied dexterity, biological systems simply outclass robotic ones. This concept is well captured in Moravec's paradox, which states that tasks that are easy for humans, such as walking or manipulating objects, are extremely difficult for robots to perform. One approach to address this challenge is through morphological computation. This is exemplified by the suction cup, whose inherent softness facilitates more effective contact. However, a significant limitation of these systems is their lack of sensing. To overcome this, researchers have attempted integrating various sensing elements, including capacitive, resistive, and camera-based sensors. This dissertation explores adaptive control with the Smart Suction Cup.

The Smart Suction cup is an airflow-based tactile sensor design that divides a single suction cup into multiple chambers. Chapter 3 presents possible adaptive control strategies with this cup design. Monitoring of the pressure differential across the chambers enables flow leakage localization, and thereby haptic search on various surfaces. Our controllers are tested on a set of adversarial objects to truly test the effectiveness of tactile sensing. Chapter 4 leverages the same haptic feedback signals to enable contour-following, enhancing the robot's ability to interact with objects of varying shapes and curvatures. By integrating these haptic signals, robots can make real-time adjustments to improve their grasping success rate, demonstrating the effectiveness of combining morphological computation with adaptive control. In Chapter 5, I summarize my dissertation contributions and potential future work.

The contributions of this thesis are as follows:

1. Summary statistics on gap distance effect on squirrel landing kinematics and forces.

2. Validation of control hypotheses on the biomechanics of squirrels landing on branches.

3. Dynamic effects of friction, damping, and stiffness on a squirrel-inspired gripper.

4. Characterization and design of model-based haptic search controllers.

5. Bin-picking experiments to benchmark performance of haptic search controllers.

6. Design of controller for contour following using a tactile sensing suction cup.

1.2 List of Publications

The results presented in this dissertation have been taken from a number of the author's publications, namely:

- Chapter 2 contains the full text of:

  S. D. Lee, S. Wang, D. Kuang, E. K. Wang, J. K. Yim, N. H. Hunt, H. S. Stuart, R. S. Fearing, R. J. Full, "Free-ranging squirrels perform stable, above-branch landings by balancing using leg force and nonprehensile foot torque," *Journal of Experimental Biology*, 2024. [in revision]

  It also contains portions of a co-authored publication:

  S. Wang, D. Kuang, S. D. Lee, R. J. Full, H. S. Stuart, "Squirrel-inspired tendon-driven passive gripper for agile landing," *International Conference on Robotics and Automation*, 2024. [published]

- Chapter 3 contains the full text of a co-first-authored publication:

  J. Lee, S. D. Lee, T. M. Huh, H. S. Stuart, "Haptic search with the Smart Suction Cup on Adversarial Objects," *IEEE Transactions on Robotics*, 2024, vol. 40, pp. 226-239 ©2024 IEEE.

- Chapter 4 contains the full text of:

  S. D. Lee, J. Lee, H. S. Stuart, "Haptic contour following with the Smart Suction Cup," *IEEE International Conference on Intelligent Robots and Systems*, 2024. [accepted]

Chapter 2

Adaptive Branch Landing in Squirrels

For gap crossing agility, arboreal animals require the ability to stabilize dynamic landings on branches. Despite lacking a prehensile grip, squirrels achieve stable landings using a palmar grasp that prepares them for parkour. We investigated the landing dynamics of free-ranging fox squirrels (*Sciurus niger*) to uncover strategies for stable, above-branch landings. Using high-speed video and force-torque measurements in the sagittal plane, we quantified landing kinetics across gap distances. Squirrels rapidly managed $> 80\%$ of the landing energy with their forelimbs. With larger gaps, peak leg force and foot torque increased. Alignment between forelimbs, velocity, and force increased, likely reducing joint moments. We tested control hypotheses based on a physical model, a spring-mass, extendable pendulum hopping robot named Salto. Squirrels stabilized off-target landings by modulating leg force and foot torque. To correct for undershooting, squirrels generated pull up torques and reduced leg force. For overshooting, squirrels generated braking torques and increased leg force. Embodying control principles in leg and foot design can enable stable landings in sparse environments for animals and robots alike, even those lacking prehensile grasps.

2.1   Introduction

Grasping capabilities can affect locomotion, feeding, social interactions and reproductive behaviors of all tetrapod clades [5, 6]. In particular, arboreal locomotion can place some of the most challenging demands on grasping as it requires a secure grip on branches while executing rapid movements and directional changes. Among locomotor behaviors in tree canopies, gap crossing onto narrow and sparse branches stands out as a common dynamic activity that often requires high-impact contact, and stabilization [7].

Primates can use highly effective prehensile grasps, employing opposable digits like the pollex and hallux to navigate arboreal environments [8, 9]. Research on tree squirrel biomechanics has primarily centered on quantifying locomotor dynamics along branches of various inclines and sizes [10, 11, 12, 13, 14, 15]. Young and Chadwell (2020) directly compared the locomotor mechanics along a branch in a sciurid rodent and two platyrrhine primates that
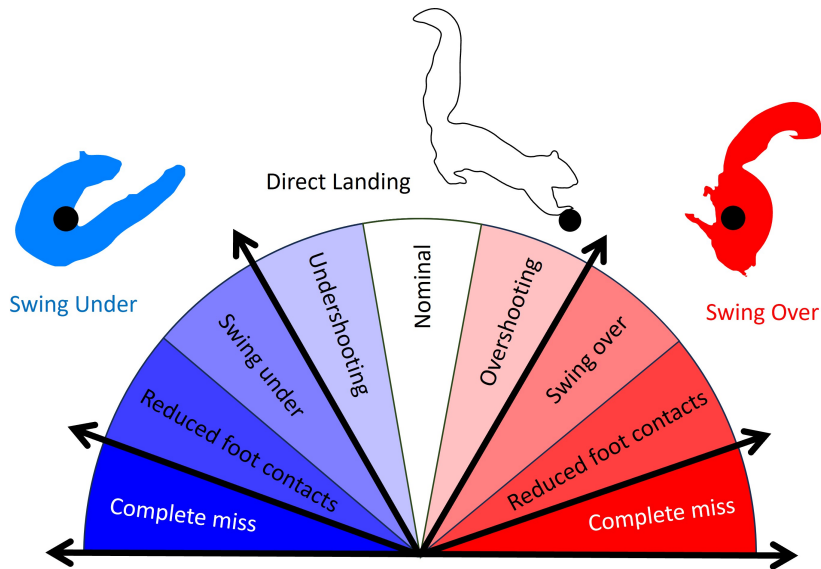
Figure 2.1: **Landing types.** As defined by Hunt et al. (2021) [1], squirrels can land with a variety of landing types. Squirrels may swing under a target branch (dark, left blue sectors), sometimes being able to make contact with only their front feet (reduced foot contact). Squirrels may also swing over a branch (dark, right red sectors), sometimes only being able to make contact with their hind feet. Squirrels may also land directly on a branch and avoid CG inversion (three middle sectors), which is critical for taking another leap if necessary. Within the envelope of direct landings, squirrels may land nominally (no landing error) or undershoot/overshoot their target.

modeled the different "stages in the evolution of primate grasping morphology" [16]. When presented with branches of different widths, squirrel monkeys, with their superior prehensile abilities, exhibited minimal kinematic adjustments in gait, speed, duty factor, and peak impact force. In contrast, marmosets demonstrated moderate adjustments, while squirrels, which lack a prehensile grasp, required the greatest adjustments. Interestingly, squirrels were also characterized by the lowest values of peak rolling angular momentum over a stride. Assuming limited grasping ability to apply torques to modulate roll, the results suggested that squirrels effectively used dynamic stability as a control strategy for arboreal balance. In the present study, we find foot friction plays a significant role in the landing and pitch balancing mechanism of squirrels, indicating a nuanced interplay between dynamic stability and the application of torque about a branch.

Grasp taxonomies from robotics offer precise analytical frameworks, making them suitable for extracting insights on the role of foot friction. Grasp types have been defined by an object's shape and size relative to the gripper and its configuration relative to the object, which may vary in the degree of digit contact and wrapping [4]. Feix et al. (2015) define

a power palmar grasp with an adducted thumb as a grasp type that relies on opposability afforded by palm and limited digit wrapping [17]. Employing only nonprehensile palmar grasps, squirrels still execute highly precise and stable, above branch landings, while also maintaining readiness for dynamic parkour off substrates. Studies on squirrel across-branch locomotion have examined jumping [1, 18] and gliding [19, 20, 21] dynamics. Hunt et al., (2021) studied free-ranging fox squirrels jumping from simulated branches to land on narrow perches [1]. Squirrels leaping across unfamiliar, simulated branches decided where to launch by balancing a trade-off between branch-bending compliance and gap distance. Squirrels learned to modify impulse generation upon repeated jumps from unexpectedly compliant beams. In over a hundred trials, squirrels never missed or fell. When squirrels were far off-target, they exhibited fail-safe and fault tolerant landings, skillfully swinging their center of gravity (CG) under (Fig. 2.1, darker, blue-shaded sectors) or over the target branch (Fig. 2.1, darker, red-shaded sectors). As spectacular as these landings are, unstable landings prevent squirrels from rapidly responding, making them more susceptible to predation. Despite squirrels using nonprehensile palmar grasps, most branch landings were direct and avoided inversions of the center of gravity above or below the branch (Fig. 2.1, three middle sectors). This allowed a squirrel to maintain its posture above the branch for its next maneuver. By quantifying the dynamics of direct landings, we test hypotheses of control stabilizing mechanisms that correct for undershooting (Fig. 2.1, lightest blue sector) and overshooting (lightest red sector) when deviating from nominal (white sector).

To quantify nonprehensile, high-impact, dynamic landing on artificial branches in free-ranging squirrels in our eucalyptus forest, we measured both touchdown state and forces in the sagittal plane at various gap distances. We used high-speed video to measure the landing kinematics. We designed a force-torque sensor apparatus that could be transported to the field to enable the first landing kinetic measurements on a horizontal branch (Fig. 2.2A-C). We tested control hypotheses for direct landings postulated by Yim et al. (in preparation) [?] for the physical model/robot Salto [22, 23, 24]. We modeled the CG to front foot contact as a compressible virtual leg comparable to a simple spring-mass, extendible pendulum system (Fig. 2.2E). We hypothesized that a nominal, direct landing (Fig. 2.1, white center sector) could be attained by squirrels using only their angular momentum to swing to a stable, balanced position. Far more likely, squirrels will undershoot or overshoot the target branch (Fig. 2.3A, Movie S1). Stabilizing off-target landings by controlling rotation about the branch could be accomplished by modulating leg force and foot torque (Fig. 2.3B). Control of front leg force could correct for overshooting by generating more leg braking force, whereas undershooting could be stabilized by generating less leg braking force. Squirrels could also correct for overshooting by generating counter-clockwise braking torques at larger landing errors and total angular momentum. Undershooting corrections could be produced by a clockwise pull up torque for a smaller landing error and total angular momentum.

Our study on squirrels aims to stimulate further research on the role of embodied control in foot and leg design for dynamic, high-impact interactions. Understanding the biomechanics of the elaborate morphology of squirrel foot and toe design can lead to novel use of metamaterials [25]. Interdisciplinary collaboration with engineers could provide biologi-
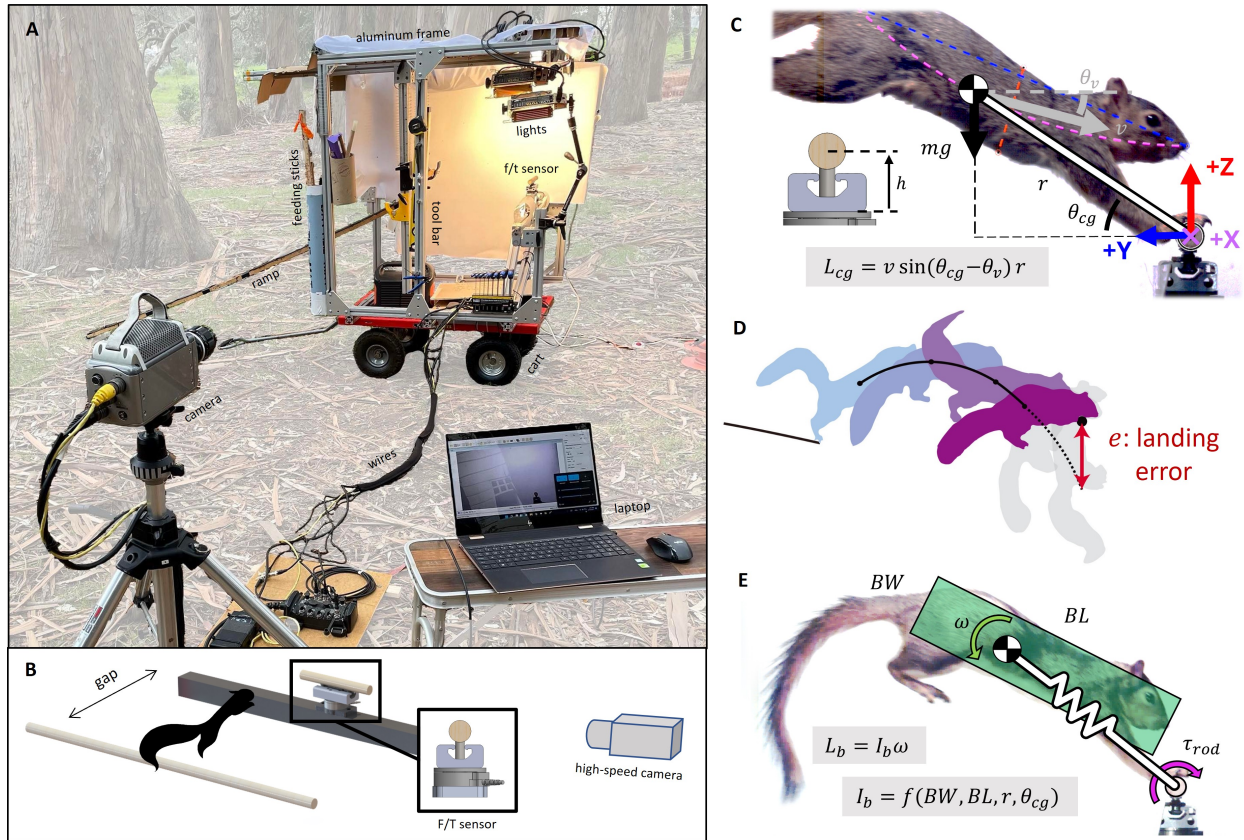
Figure 2.2: **Field apparatus and key kinematic quantities of S. niger landing.** (A) Mobile field apparatus in the eucalyptus forest. High-speed video recordings and force-torque measurements were made during voluntary landings using the cart supporting the aluminum frame and F/T sensor, a ramp, lights, high-speed camera, and a laptop for data acquisition. (B) Diagram showing the take-off branch, the gap distance jumped, the force/torque (f/t) sensor (with lateral view in box) and high-speed camera. The take-off rod was attached to a linear rail, which allowed for variable gap distances of 50, 75, and 100 cm. (C) CG is graphically calculated by fitting a parabola between three points as in Hunt et al. (2021): nose, tailbase, and the midpoint of the ventral-dorsal line (red dashed), which approximately bisects the tailbase-nose line (blue dashed). CG position and velocity were extracted to calculate CG angular momentum (L_{cg}) and landing error (e). The distance, h, between F/T sensor interface and the branch axis was h = 40mm. (D) Landing error (e) was calculated as the projected vertical offset of the extrapolated aerial trajectory (see Hunt et al., 2021). (E) Body angular momentum is a function of body moment of inertia (L_b) and body pitch rate (ω). The body is modeled as a cylinder body length (BL), diameter (body width, BW), and the CG position.

cal inspiration for the development of the next generation of legs and feet for agile legged robots, as well as nonprehensile robotic manipulators. These findings point to the promise that examining dynamic, high-impact landings and stabilization with only nonprehensile, palmar grasps can further advance the field of grasping and manipulation for both animals and engineered systems.

2.2 Materials and Methods

To measure squirrel landing dynamics, we designed experiments to capture the kinematics, forces, and torques using an instrumented branch or rod. The experiments involved three key components: (1) the acquisition and training of free-ranging research animals, (2) the utilization of a mobile instrumented apparatus, and (3) a systematic data collection and processing procedure for subsequent analysis. The ethical treatment of animals and adherence to protocols were ensured through the approval of the University of California, Berkeley's Animal Care and Use Committee (ACUC) Protocol # AUP-2018-06-11201-1 and the California Department of Fish and Wildlife Nongame Wildlife Program.

Animal preparation

Sciurus niger are free-ranging arboreal squirrels known for their adept navigation in tree canopies. These squirrels have adapted to urban environments and can be easily observed in our university groves. Their agility and accessibility make *S. niger* an ideal candidate for studying and characterizing arboreal locomotion [1]. Here we focus on the measurement of landing forces, rod torque, and high-speed video involving four female fox squirrels (*S. niger*; 729 ± 63 g). To uniquely identify each individual, a non-toxic fur dye (Nyanzol D) was prepared and dispersed on squirrels' fur.

Introducing free-ranging individuals to a novel apparatus required training squirrels with a shaping paradigm using peanuts as positive reinforcement for approximately 3-5 weeks. Individuals were introduced to the setup at different times over a span of 4 months based on their voluntary willingness to cooperate. After acclimation, individuals were trained to follow a feeding stick and execute jumps from a non-instrumented take-off perch (0.75" diameter birch dowel) to a target, instrumented perch (0.75"). To minimize learning effects, each individual underwent training until they successfully completed at least five landings on the instrumented perch. A successful landing was defined as a direct landing in which foot contact is restricted to the rod only, without swinging under or over the landing target (Fig. 2.1, center sector). Data collection only occurred immediately after this training was completed by each individual at each of the gap distances.
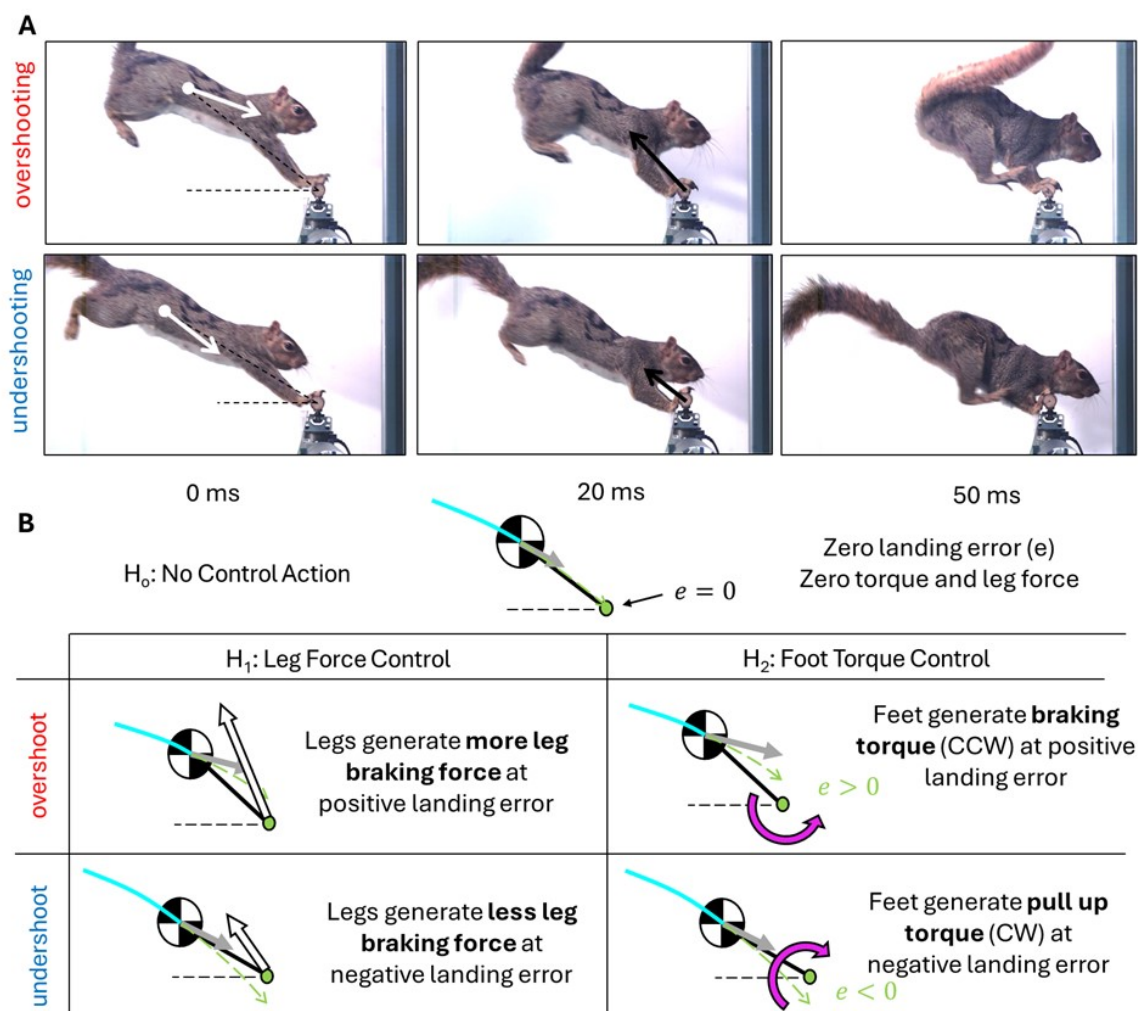
Figure 2.3: **Balanced landing control hypotheses for undershooting and overshooting trajectories.** A) Snapshots at three different time intervals - touchdown, 20 ms, and 50 ms (close to hindfoot touchdown, thf). At touchdown, the black arrow begins at the CG and represents the velocity vector. At 20 ms, squirrels start bringing their hind feet forward to prepare for a second touchdown. At 50 ms, the undershooting trial shows hindfoot touchdown while in the overshoot trial, the hindfeet have not touchdown yet due to the greater imparted braking force. B) Force-torque control hypotheses after Yim et al. (in prep) are summarized for undershooting and overshooting conditions.

Field force, torque, and kinematics apparatus

We designed and implemented an experimental setup to simultaneously capture three-dimensional force/torque data and 2D high-speed video of squirrels landing on artificial and instrumented branches. The force measurement device (Fig. 2.2A,B) utilized a 6-axis Force/Torque (F/T) transducer (ATI Mini45 with SI-145-5 calibration) and data acquisition system (NI USB-

6210 DAQ). The F/T sensor was connected to the DAQ and a power supply for 3D force data streaming. The DAQ was connected to a computer (Windows 11 Laptop) for data recording through NI LabVIEW. The hardware selection allowed for measurements with force resolution of 62.5 mN in all three axes, a torque resolution of 1.3 Nmm in the X-axis, and a sampling rate of 3000 Hz.

The mechanical structure of the apparatus was designed for high stiffness but also to be lightweight and compact for ease of transport into the field (Fig. 2.2A). To minimize vibrations in the F/T signal, an aluminum truss was attached to the base-side of the F/T sensor. An artificial branch was attached to the topside of the sensor, and its offset from the sensor interface was minimized to maximize the cantilever's natural frequency, which aided in minimizing signal loss when filtering the signal. Outdoors, the ground can be uneven, so two measurement levels were attached to the setup to ensure the sensor was as horizontal as possible. The take-off branch was attached to a rail, which enabled quick adjustment of gap distance and experimental conditions.

As shown in Fig. 2.2A, the instrumented setup was transported to a nearby eucalyptus grove. A ramp guided squirrels to the take-off branch substrate. A high-speed camera (Vision Research, Phantom v10.0) sat level and approximately 8 feet away from the subject. Incandescent light bulbs provided a non-flickering light source. The high-speed camera was set to record at 500fps, 1080p. Force and video data were electronically synchronized through the Vision Research GUI.

Instruments of the apparatus (i.e., camera, flood lights, laptop, DAQ) were first connected to an outdoor power outlet. The F/T sensor and camera were placed and then leveled such that the landing substrate and squirrel's body were visible in the camera frame. Given the brevity of the landing event, the instruments were armed to end-trigger recordings. When available, free-ranging individuals were guided towards the setup with feeding sticks. A researcher prompted an individual to climb up the ramp and to cross the gap by leaping between rods or perches. For a given trial, another researcher end-triggered force and video data as soon as the squirrel came into contact with the F/T sensor. Data was then written to the laptop. After five trials, data collection was terminated for the given experimental condition.

Feature extraction

We digitized the high-speed video sequences of each landing by manually marking key points and drawing lines between them as shown in Fig. 2.2C. Their motion is tracked for at least 5 frames pre- and post- front feet touchdown (± 10 ms from t_0) to ensure a reliable estimate for landing velocity. These key points were chosen from a previous study [1]. and were used to calculate CG in a similar manner. They included nose, tail base, dorsal midpoint, ventral midpoint, and branch center. The trajectories of these points were computed in the camera view. From r, v, θ_{cg}, and θ_v as defined in Table 2.1, we computed tangential and radial speed as well as body pitch rate with the following equations:

Table 2.1: **All measured and calculated force, torque, and kinematic variables used for featurizing each landing sequence.**

Variable	Name	Units	Description	Variable	Name	Units	Description
Timing				**Touchdown Kinematics**			
t_1	1st peak time	ms	First peak force	r	Rod to CoM Distance	mm	Distance r in Fig. 4A.
t_{hf}	Hind feet touch-down	ms	Second contact	v	CoM speed	m/s	Speed v in Fig. 4A.
T	Settling time	ms	End of landing	θ_{cg}	CoM touch-down angle w.r.t. horizontal	deg	Angle θ_{cg} in Fig. 4A.
Force, Torque, and Impulse							
F_h	Horizontal force magnitude	N	y-axis force	θ_v	Velocity angle w.r.t. horizontal	deg	Angle θ_v in Fig. 4A.
F_v	Vertical force magnitude	N	z-axis force	BL, BW	Body width and length	mm	Dimensions of squirrel body as a cylinder.
τ_x	x-axis torque magnitude	Nmm	Measured from F/T sensor.	I_b	Body moment of inertia	m^2	$I_b = f(BW, BL, r, \theta_{cg})$ See Supplement.
F_{net}	Net force magnitude	N	Camera-view force $\sqrt{F_v^2 + F_h^2}$	γ	Body pitch	deg	Angle w.r.t to horizontal of blue line in Fig. 4A
θ_F	Force angle w.r.t. horizontal	deg	$atan2(F_v, F_h)$	ω	Body pitch rate	deg/s	$\dot{\gamma} = \frac{\gamma(t+\Delta t)-\gamma(t)}{\Delta t}$
τ_{rod}	Rod-axis torque magnitude	Nmm	$\tau_{rod} = \tau_x - F_h h$ where h is defined in Fig. 4A.	L_{cg}	CoM angular momentum	m^2/s	$L_{cg} = v\sin(\theta_{cg} - \theta_v)r$ in Fig. 4A.
J_0	Impulse from front leg	Ns	$J_0 = \int_0^{t_{hf}} F_{net}(t)\,dt$	L_b	Body angular momentum	m^2/s	$L_b = I_b\omega$
J_T	Total landing impulse	Ns	$J_T = \int_0^T F_{net}(t)\,dt$	L_{total}	Total angular momentum	m^2/s	$L_{total} = L_{cg} + L_b$
				e	Landing error	mm	Distance e in Fig. 4B.

$$v_r = v\cos(\theta_{cg} - \theta_v) \tag{2.1}$$

$$v_\theta = v\sin(\theta_{cg} - \theta_v) \tag{2.2}$$

$$\omega = \dot{\gamma} = \frac{\gamma(t + \Delta t) - \gamma(t)}{\Delta t} \tag{2.3}$$

From r, v, θ_{cg}, and θ_v, we also calculated landing error and total angular momentum. Landing error was computed as:

$$e = r_y + v_y\Delta t - \frac{g}{2}\Delta t^2 \tag{2.4}$$

where $\Delta t = r_x/v_x$ and r_x, r_y, v_x, and v_y are the horizontal and vertical components of leg length and velocity, respectively, and g is gravitational acceleration. CG and body angular momentums were computed as:

$$L_{cg} = mv_\theta \times r \tag{2.5}$$

$$L_b = I_b\omega \tag{2.6}$$

where I_b is the instantaneous body moment of inertia. We approximated the squirrel as a cylinder with diameter BW and length BL. Then, the moment of inertia can be approximated as:

$$I_b = \frac{1}{4}m(\frac{BW}{2})^2 + \frac{1}{12}m(BL)^2 \tag{2.7}$$

where BW is the squirrel's body width and BL is the body length. The sum of angular momentums yields the total angular momentum:

$$L_{total} = L_{cg} + L_b \tag{2.8}$$

From the synchronized dataset, we filtered the raw force data from each trial to remove high-frequency noise and mechanical vibrations from the setup. We used an 8th order forward-backward low-pass Butterworth filter with a 40 Hz cutoff frequency. Filter design and minimal attenuation were facilitated by the fact that both the F/T sensor attachment and base have sufficiently high natural frequencies in the vertical and horizontal axes (above 300Hz). When a squirrel comes into contact with the setup however, the natural frequency of the squirrel-branch system decreases significantly. Through signal mode decomposition, we found a cutoff frequency of 40 Hz was a good balance between removing system vibrations and preserving the signal of interest. Features were extracted from net force and rod torque data as defined in Table 2.1. Rod torque was computed with the following equation:

$$\tau_{rod} = \tau_x - F_h h \tag{2.9}$$

where τ_x is the raw torque measurement about the x-axis, F_h is the raw horizontal force measurement, and h is the distance between the branch center and the F/T sensor's interface. Forelimb and total linear impulse were computed as follows:

$$J_0 = \int_0^{t_{hf}} F_{net}\, dt = m\Delta v = m(v_0 - v_{hf}) \tag{2.10}$$

$$J_T = \int_0^T F_{net}\, dt = mv_0, \tag{2.11}$$

where F_{net} is the net force, t_{hf} is the hindfoot touchdown time, v_{hf} is the unknown speed at t_{hf}, and T is the time to landing completion. Impulse can be approximated as the mass times change in speed for the given time intervals. Then with these two impulses, we define forelimb impulse contribution α, which yields a relationship between α, v_0 , and v_{hf}:

$$\alpha = \frac{J_0}{J_T} = \frac{v_0 - v_{hf}}{v_0} = 1 - \frac{v_{hf}}{v_0} \tag{2.12}$$

We also define energy states at t = 0 ms and t = t_{hf}.

$$KE_0 = \frac{1}{2}mv_0^2 \tag{2.13}$$

$$KE_{hf} = \frac{1}{2}mv_{hf}^2 \tag{2.14}$$

We define forelimb energy contribution β using these two energy states, which yields a relationship between β, v_0 , and v_{hf}:

$$\beta = \frac{\Delta KE}{KE_0} = \frac{KE_0 - KE_{hf}}{KE_0} = 1 - \frac{v_{hf}^2}{v_0^2} \tag{2.15}$$

Combining the equations above yields the relationship between α and β,

$$\beta = 1 - \frac{[v_0(1 - \alpha)]^2}{v_0^2} = 2\alpha - \alpha^2 \tag{2.16}$$

Statistical analyses

Over eight experimental sessions, squirrels performed over 60 successful landings. We focused our analysis on force and high-speed video data of n = 60 successful landings, five trials for four individuals at three gap conditions. Some trials were excluded for one of two reasons: a) The camera view did not capture the squirrel's tailbase at touchdown, so CG kinematics at touchdown could not be extracted (n=11), or b) the squirrel severely undershot or overshot the target branch, resulting in an unstable landing, appendages coming into contact with other parts of the setup, and therefore invalid force-torque measurements (n=2). Then, for extraction of the landing state from high-speed video data, we analyzed n = 49 landings. Means and standard deviations are reported for metrics across all trials for each gap condition. P-values and F-statistics are reported from one-way repeated-measures ANOVA comparisons across gap distances. P-values and t-statistics are also reported for the linear mixed-effects models controlling for gap and individual to show predictive power of landing error and angular momentum. Data were analyzed using MATLAB statistical software tools.
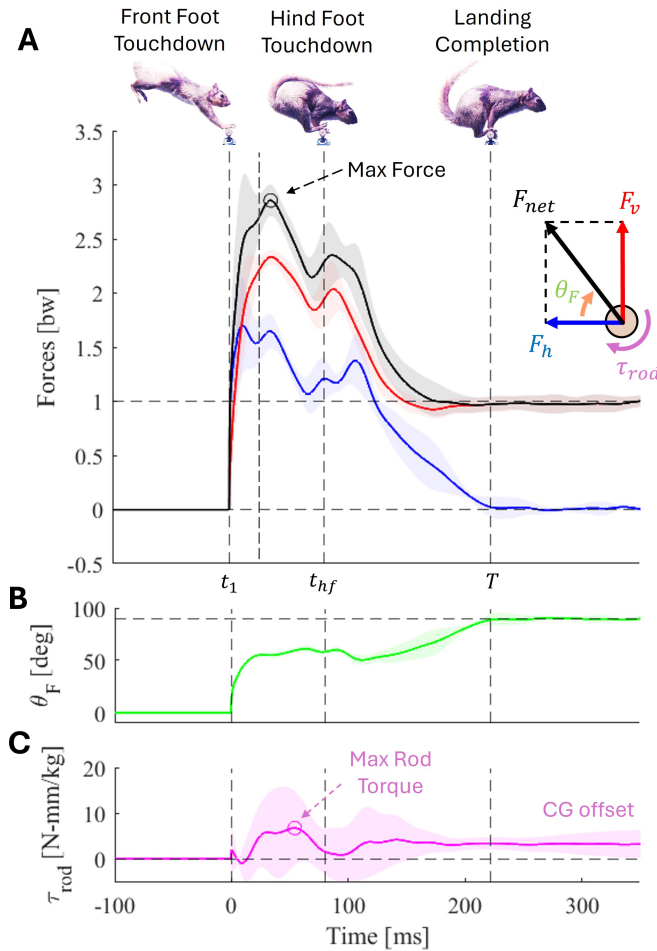
Figure 2.4: **Branch landing reaction force, maximum force angle, and rod torque as a function of time.** (A) Mean net force and force components are plotted over time. Light bands show one standard deviation. Squirrels showed maximum force peaks during front feet touchdown and a secondary smaller peak after hind feet touchdown. Vertical dashed lines indicate critical landing times (t_1: time to peak force, t_{hf}: hind feet touchdown, T: landing completion time). Front feet (t = 0) or hind feet (t_{hf}) touchdown time is defined as the frame in which the feet first come into contact with the branch. Settling time (T) is defined as the time at which F_h reaches 0 N. (B) Net force angle stabilizes around 50 degrees and steadily increases to a vertical 90 degrees after t_{hf} until t = T. (C) Maximum rod torque can be positive and negative throughout the time series, as seen in the magenta shaded area. When t > T, τ_{rod} settles to a non-zero value, which corresponds to static torque while perched.

2.3   Results

Landing dynamics as a function of time

Kinematics of landing

Throughout the experiments, squirrels crossed gaps following projectile motion trajectories. Forces normal to the camera view (X-axis of the load cell) were negligible compared to forces in the squirrel's sagittal plane (YZ-plane of load cell). Squirrels exhibited a diverse range of landing touchdown states i.e., CG position and velocity with respect to the branch. In all landings, squirrels always touched down with their front feet first, quickly followed by their hind feet (Fig. 2.4A). As squirrels landed, they actively rotated their joints – shoulders, spine, tail, head, hips, and limbs to control their body pose such that their hind legs could make contact with the branch. This is required to reach the stable, above-branch, end state, that is, upright with zero speed. In a typical sequence for a given gap and individual, squirrels prepared for touchdown by extending their forelegs and front feet. The extended feet first engaged with the branch to create a reliable anchor. Then, the front limbs compress as kinetic energy decreases. A force peak always followed front feet touchdown. The first peak force induced by the front limbs was always greater than the second one, which was induced after hind feet touchdown. At the end of the landing at t = T , the hind feet provided friction for static balance while the front feet either stayed in contact or detached.

Branch reaction force timing during landing

Landings for a given individual were consistent. A characteristic set of leg reaction force data (n=5 trials) for one individual at the 75 cm gap distance is shown in Figure 4A with its net force angle in Figure 4B. Figure 4C represents the maximum rod torque which in this trial is clockwise, positive. Here, the shaded regions illustrate variability, which is defined as the standard deviation across five trials. We define t = 0 ms as the time at which the front feet first come into contact with the branch. We visually examined high-speed video to extract the frame at which contact occurred. The first force peak occurred at t_1, the time at which F_{net} reached its global maximum. The hindfoot touchdown time, t_{hf} , is defined as the time at which the hind feet first make contact, which was visually noted on the high-speed video. Finally, we estimated the end of the landing, T, as the time at which the horizontal force, F_h, reached and settled to 0 N. Snapshots corresponding to t = 0 ms, t_{hf}, and T are displayed sequentially in Fig. 2.4A. Table 2.2 reports time variables mean and standard deviation for each event at each gap distance tested. Depending on gap distance, squirrels completed landings within T = 200-350 ms. Within 20-65 ms, squirrels reached peak forces. Hind feet touchdown occurred within 60-140 ms or within 29-43% of T.

Table 2.2: **Landing variable measurements as a function of gap distance.** Mean ± S.D. of variables.

Name	Symbol	50 cm	75 cm	100 cm	F	p Value
Timing						
Time to peak force (ms)	t_1	45 ± 20	28 ± 7.7	22 ± 9	30.8	8.04e-7 ***
Hindfeet touchdown time (ms)	t_{hf}	124 ± 15	95 ± 12	68 ± 10	353.9	2.30e-26 ***
Landing completion time (ms)	T	313 ± 61	262 ± 27	232 ± 59	30.6	7.97e-7 ***
Force and Torque						
Peak net force (BW)	F_{net}/mg	2.09 ± 0.19	3.25 ± 0.30	4.31 ± 0.49	488	2.51e-29 ***
Max force angle (deg)	θ_F	51.7 ± 3.4	47.5 ± 4.4	46.1 ± 5.2	38.3	7.47e-8 ***
Peak rod torque (N-mm/kg)	τ_{rod}/m	54 ± 58	95 ± 97	136 ± 169	5.0	0.029 *
Peak rod torque magnitude (N-mm/kg)	$|\tau_{rod}|/m$	72 ± 31	114 ± 73	191 ± 97	31.3	6.86e-7 ***
Impulse						
Forelimb force impulse (N-s)	J_0	1.09 ± 0.29	1.64 ± 0.34	1.77 ± 0.32	81.4	1.65e-12 ***
Total force impulse (N-s)	J_T	1.67 ± 0.30	2.33 ± 0.35	2.77 ± 0.26	324.7	5.66e-25 ***
Forelimb impulse contribution (%)	α	65.4 ± 9.7	70.3 ± 8.3	64.1 ± 11.3	0.3	0.58
Forelimb energy contribution (%)	β	87.1 ± 7.6	90.5 ± 5.5	85.9 ± 9.0	0.5	0.48
Touchdown Kinematics						
Touchdown virtual leg length (mm)	r	205 ± 9	208 ± 10	208 ± 7	5.7	0.021 *
Touchdown leg angle (deg)	θ_{cg}	34.9 ± 4.0	34.4 ± 4.8	37.7 ± 5.6	2.7	0.10
Touchdown velocity angle (deg)	θ_v	23.1 ± 4.8	28.4 ± 4.9	34.1 ± 4.7	145.4	5.46e-16 ***
Touchdown speed (m/s)	v	1.71 ± 0.18	2.29 ± 0.23	2.79 ± 0.18	251.7	1.68e-20 ***
Radial speed (m/s)	v_r	1.67 ± 0.17	2.28 ± 0.23	2.78 ± 0.18	277.2	2.44e-21 ***
Tangential speed (m/s)	v_θ	0.35 ± 0.09	0.24 ± 0.10	0.17 ± 0.15	32.6	7.45e-7 ***
Body length (mm)	BL	279.2 ± 16.3	270.7 ± 13.1	270.0 ± 7.8	4.7	0.035 *
Body pitch (deg)	γ	24.3 ± 3.3	26.7 ± 3.7	25.4 ± 3.7	0.4	0.51
Body pitch rate (deg/s)	ω	-122.4 ± 63.2	-59.6 ± 87.1	-25.0 ± 84.2	14.0	5.06e-4 ***
Landing Error and Angular Momentum						
Landing error (mm)	e	-11.7 ± 18.2	-11.9 ± 15.0	-9.7 ± 16.5	0.6	0.43
Angular momentum (m²/s)	L_{cg}	0.073 ± 0.020	0.051 ± 0.023	0.036 ± 0.031	30.6	1.38e-6 ***
Body angular momentum (m²/s)	L_b	-0.015 ± 0.009	-0.007 ± 0.010	-0.003 ± 0.009	15.0	3.37e-4 ***
Total angular momentum (m²/s)	L_{total}	0.058 ± 0.016	0.044 ± 0.023	0.033 ± 0.034	10.5	2.20e-3 **

F statistics and p values are reported from repeated-measures ANOVA comparisons between experimental conditions.
* significant at 0.05 level.
** significant at 0.01 level.
*** significant at 0.001 level.

Impulse reflecting energy management by forelimbs

Forelimb impulse is calculated as the area under the F_{net} curve from t_0 to t_{hf} (See Table 2.1). J_T is the total impulse induced by the landing event. Impulse can also be calculated as a change in momentum ($J = m\Delta v$). We define α as the ratio between forelimb impulse and total impulse, $\alpha = J_0/J_T$ (Eqn. 12). We found that $\alpha = 67 \pm 10\%$, which means on average, 67% of speed was decelerated by the forelimbs alone.

We can also compute β, the ratio between kinetic energy managed by the forelimbs over the total touchdown kinetic energy. Here, we express β in terms of α, as $\beta = 2\alpha - \alpha^2$ (Eqn.

2.16). Using this equation, we calculate that on average, squirrel forelimbs manage 88% of landing kinetic energy, regardless of gap distance. This occurred within 60-130 ms, which on average is 36% of T. Therefore, forelimbs were responsible for managing most of the landing kinetic energy in a fraction of the landing period.

Landing dynamics as a function of gap distance

Gap distance effect on touchdown kinematics

Squirrel touchdown kinematics are defined by the CG's position and velocity at t = 0 ms. As seen in Table 2.2, virtual leg length (r) and leg angle (θ_{cg}) did not vary significantly across gap distances ($p > 0.01$). However, speed (v) and velocity angle (θ_v) both increased with gap distance. As gap distance increased, squirrels took higher [one-way repeated measures ANOVA, $F(1,47)= 145.4$, $p < 0.001$] and faster ballistic trajectories [$F(1,47)= 251.7$, $p < 0.001$]. As gap distance increased, squirrel landing velocity angle, θ_v, also approached the 45° launch angle that tends to maximize horizontal travel for a particular speed. Touchdown velocity can be broken down into radial and tangential components. Like speed, radial speed (v_r) increased with gap distance [$F(1,47)= 277.2$, $p < 0.001$]. Tangential speed (v_θ) on the other hand, decreased with gap distance [$F(1,47)= 32.6$, $p < 0.001$]. Squirrel touchdown kinematics are also defined by the body's posture and rotational speed at t = 0 ms. Body length (BL) and body pitch (γ) were not significantly different across gap distances ($p > 0.01$). However, body pitch rate (ω) decreased in magnitude as gap distance increased [$F(1,47)= 14.0$, $p < 0.001$].

For all key time points, average time decreased as gap distance increased, pointing towards a consistent force behavior over time. Hindfoot touchdown time (t_{hf}) decreased from 124 ms at 50 cm to 68 ms at 100 cm, indicating hind feet touched down faster at longer gap distances [$F(1,58)= 353.9$, $p < 0.001$; see Table 2.2]. The landings were completed more rapidly the longer the gap distance [$F(1,58)= 30.6$, $p < 0.001$]. The landing sequences themselves were approximately 80 ms shorter at the 100 cm gap compared to the 50 cm gap. Time to peak reaction force also occurred sooner, decreasing from 45 ms to 22 ms [$F(1,58)=30.8$, $p < 0.001$].

Gap distance effects on force-torque, force angle, and impulse

Upon touchdown across all trials, squirrels exerted a peak wrench (peak force and torque) on the branch (Table 2.2). As expected, peak F_{net} increased with gap distance more than doubling from 2.09 bw at 50 cm to 4.31 bw at the 100 cm distance [Fig. 2.5, $F(1,58)= 488$, $p < 0.001$]. Maximum force angle (θ_F) decreased with increasing gap distance [$F(1,58)= 38.3$, $p < 0.001$] from 51.7° at 50 cm to 46.1° at 100 cm (see Table 2.2), becoming more horizontal at longer gap distances. A lower maximum force angle implies that at longer gap distances, squirrels are relying more on horizontal force rather than vertical force to decelerate their landings.
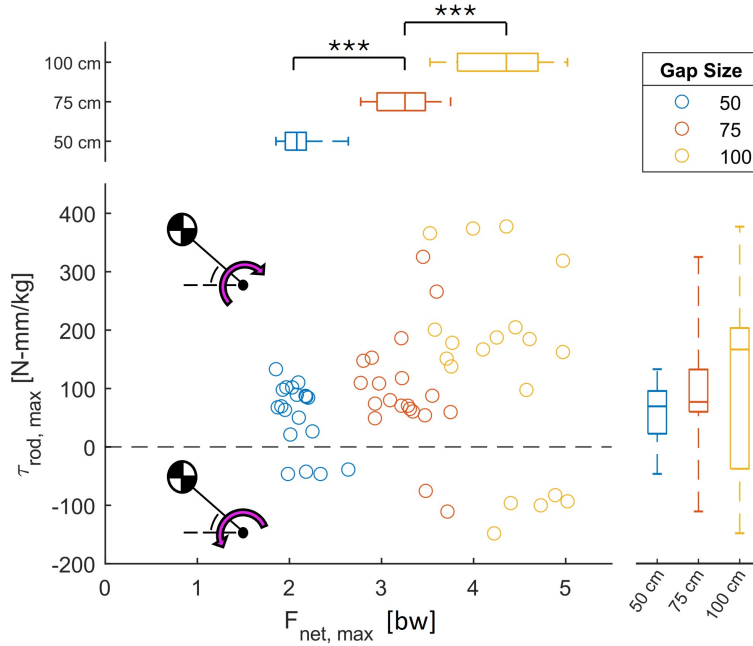
Figure 2.5:   **Grasping wrench space represented by peak foot torque (τ_{rod}) and peak leg force (F_{net}) at each gap distance.**   (Wrench space refers to force and torque pairs). Individual points and box plots illustrate data spread with median. Bars represent quartiles. Peak F_{net} magnitude and variation tend to increase with gap distance (*** p < 0.001). Comparisons are made across gaps (*** p < 0.001). Mean peak rod is statistically different across gaps (* p < 0.05). This difference is more significant when comparing magnitudes of rod torque (*** p < 0.001, See Table 2.2). Standard deviation also increased with gap distance. Purple arrows represent branch reaction torque direction.

Peak τ_{rod} magnitude increased with gap distance [F(1,58)= 31.3, p < 0.001] more than doubling from 72 N-mm/kg at 50 cm to 191 N-mm/kg at 100 cm (Fig. 2.5). The range of peak τ_{rod} magnitude values also increased with gap distance, tripling from 31 N-mm/kg at 50 cm to 97 N-mm/kg at 100 cm (see Table 2.2; Fig. 2.5). The larger variation in peak torque is likely because longer gap distances required higher take-off and landing speeds, which would yield greater variation in touchdown states. We postulate that the increasing variation in peak force and torque can be explained by this variation in touchdown state.

Forelimb impulse J_0 and total forelimb impulse J_T increased with gap distance [F(1,58) = 81.4, p < 0.001, and F(1,58) = 324.7, p < 0.001, respectively; see Table 2.2]. However, forelimb impulse and energy contribution, α and β, do not vary significantly across gap conditions [F(1,58) = 0.3, p=0.58, and F(1,58) = 0.5, p=0.48, respectively] indicating that the variation in forelimb contribution is not explained by gap distance. Forelimb impulse contribution (α) was 66.7 ± 10.0% and forelimb energy management (β) was 87.9 ± 7.6%.
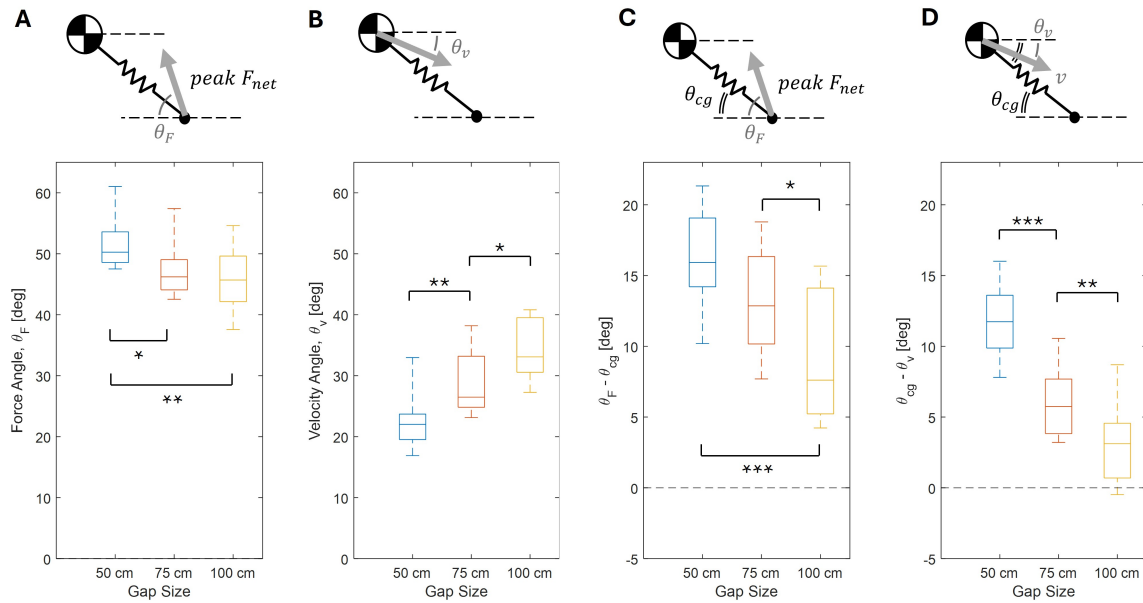
Figure 2.6: **Force and velocity angles and angles relative to the leg angle at each gap distance.** (A) Maximum force angle decreased as gap distance increased (* $p < 0.05$, ** $p < 0.01$). (B) Velocity angle increases as gap distance increases. (C) Difference between maximum force and leg angle decreased as the gap distance increased (*** $p < 0.001$). (D) Difference between velocity and leg angle also decreased. As gap distance increases, maximum force and velocity align more to the forelimb such that $\Delta\theta \to 0$.

Gap distance effect on landing error and angular momentum

The touchdown kinematics can be simplified to two variables: landing error and total angular momentum. Landing error is defined as the vertical distance between the projected ballistic trajectory of the squirrels' CG and the branch center. On average, landing error across all trials was -11.3 ± 16.4 mm, and it did not increase or decrease with gap distance ($p > 0.05$; Table 2.2). Normalizing with squirrel body length did not result in statistical differences in landing error.

Total angular momentum is defined as the sum of CG angular momentum, L_{cg}, and body angular momentum, L_b. Angular momentum of the CG about the branch was significantly different across gap distances [$F(1,49) = 30.6$, $p < 0.001$], decreasing from 0.073 m^2/s at 50 cm to 0.036 m^2/s at 100 cm. Similarly, body angular momentum decreased significantly in magnitude with increasing gap distance [$F(1,49) = 15.0$, $p < 0.001$] from -0.015 m^2/s at 50 cm to -0.003 m^2/s at 100 cm. Finally, total angular momentum also tended to decrease with increasing gap distance [$F(1,49) = 10.5$, $p < 0.01$] decreasing from 0.058 m^2/s at 50 cm to 0.033 m^2/s at 100 cm. Generally, angular momentums tend to zero the longer the gap distance.

2.4 Discussion

Reaction force patterns and magnitudes during landing

Boulinguez-Ambroise and colleagues (2023) highlight in their study on tree squirrel jumping that, although jumping performance is often discussed as a pivotal aspect of early primate evolution, its quantification in arboreal mammals is lacking compared to other locomotor behaviors, such as quadrupedal walking and running on branches [18]. The prevalent focus on locomotion along branches [26, 16, 12, 10, 27, 28, 13, 29]. largely stems from the research in the initial stages of primate evolution, particularly concerning the ability to grasp thin terminal branches. Our study extends beyond assessing movement along branches or saltatorial ability by examining the challenge of executing a stable landing on a narrow branch without the advantage of a prehensile grasp.

Since Bonser's (1999) review [30], surprisingly few studies involve landing kinetics that consider grasping or balancing. Among the studies that have explored landing dynamics, various animals such as birds, lemurs, cats, and toads have been investigated. In our fox squirrels (∼750 g), balanced branch landing most often produced a bimodal branch reaction force pattern (Fig. 2.2A). Within just 20-65 ms after touchdown, squirrels reached peak reaction forces resulting from front foot touchdown. Hind foot touchdown occurred within 60-140 ms corresponding to a second, smaller reaction force peak. Peak F_{net} increased with gap distance more than doubling from 2.1 bw (multiples of body weight) at 50 cm to 4.3 bw at the 100 cm distance (Fig. 2.5; Table 2.2). Peak branch torque τ_{rod} produced by the palmar grasp of the front feet occurred between their front foot touchdown and hind foot touchdown. Average peak τ_{rod} also increased with gap distance more than doubling (72 N-mm/kg at 50 cm to 191 N-mm/kg at 100 cm; Fig. 2.5).

Birds, such as parrotlets, demonstrate an intricate use of their feet during landing on branches, employing opposable digits for effective grasping. While birds primarily utilize their wings to generate supportive aerodynamic forces, Roderick et al. (2019) observed that parrotlets (∼30 g) exert perch reaction forces ranging from 4 to 5 bw [31]. Birds reach peak reaction forces within 5-10 ms, and unlike squirrels, parrotlets use only their hindlimbs to apply ground reaction forces, resulting in a unimodal force pattern. Their feet follow a consistent sequence of movements when landing, including spreading, opening, preshaping, wrapping around the branch, and curling their claws. Their study revealed that after touchdown, the dynamics of the foot, toes, and claws are crucial for a successful perch, and that these anchoring mechanisms are surface specific. These actions, particularly the toe squeeze, enhance stability upon landing, providing an advantage that squirrels lack.

Landing kinetics have been measured in leaping lemurs attempting to grasp a compliant vertical pole acting as a force sensor [32, 33] Peak landing reaction forces ranged from 5-11 bw, but no time course was reported. Demes, et al. studies show that some lemurs show a more diverse landing pattern and behavior when leaping down to a flat and horizontal force plate. They show a bimodal reaction force pattern representing the front and hind limbs [34] However, the first peak reaction force depended on whether the fore- or hindlimb struck

the platform first. This differed among the two species in question. Peak vertical reaction forces ranged from 1.7-1.9 bw for the forelimb lander (1.9 kg) and 2.0-3.1 bw for the hindlimb lander (3.1 kg), both increasing with jump distance. Hindlimb landing species reached their first force peak at 100 ms and completed landing in 400 ms.

Landing kinetics using extending forelimbs, as shown by our squirrels, have also been measured in both cats and toads landing on flat surfaces instrumented with a force plate. Cats (4-5 kg) jumping down from a platform extend their forelimbs for landing impact [35] Cats generate a bimodal reaction force pattern that results from the first peak force from front leg landing followed by the rotation of the body allowing hind limb landing to produce a second peak force [36] As jump height is increased further, peak reaction forces from the front limb increased from approximately 3 to 8 bw, whereas hind limb forces could increase far more, ranging from 2.5 bw to as great as 20 bw [37]. A faster increase in hindlimb peak force implies that as platform height increases, cats use their hindlimbs more for energy management. Time to peak force shifts from 10 ms to 40-50 ms. Similarly, as hopping toads (250 g) prepare for landing, they also fully extend their front legs or hands [38, 39, 40]. Landing consists of two phases defined by two peaks of vertical reaction force coinciding with the impact of two body parts. In the Hand Landing Phase, the extended arms hit, flex, and rotate as they absorb the landing energy. The vertical force peaks tend to be near 1.75 bw. The Body/Feet Landing Phase begins when the folded hindquarters (i.e., pelvis, abdomen, and feet) hit the ground simultaneously. The peak vertical force for this landing phase was approximately equal to body weight.

Force, velocity, and leg alignment

Alexander (1991) emphasized the importance of aligning ground reaction force (GRF) vectors with the center of mass and joint centers for energy conservation in legged locomotion [41]. Chen et al. (2006) and Full et al. (1991) demonstrated that animals maintaining a consistent average speed, regardless of their number of legs or posture, tend to align these force vectors along their legs [42, 43]. This alignment minimizes joint moments and reduces the work required by the limbs. The significance of this alignment can become even more critical during higher speed landings, where the primary concern shifts from energy conservation to injury prevention - from efficiency to safety.

For landing squirrels, we used impulse estimates to conclude that the forelimbs and torso manage 80-95% of kinetic energy within 60-140 ms (Table 2.2). We also measured the angle differences between maximum reaction force angle, velocity angle, and leg angle (Fig. 2.6). We found that the difference between the maximum reaction force angle and leg angle decreased with gap distance (Fig. 2.6C). The difference between leg angle and velocity angle also decreased with gap distance (Fig. 2.6D). Both of these differences approach zero as the gap distance increases. This suggests that alignment between ground reaction force, touchdown velocity, and virtual leg angle increases as gap distance increases. In other words, the longer the gap distance, the more vector alignment is present, which could result in a reduction of joint moments.

Like squirrels, cats also align ground reaction forces on jump down landings with their forelimbs [35]. Specifically, cats land with shallower leg angles to offload GRF to their hindlimbs, thereby reducing the peak force on the forelimbs. The reduction protects the forelimbs from damage in higher speed landings. Wu et al. (2019) have shown that at higher jump heights, cat hindlimbs play a greater role than the forelimbs in absorbing landing energy as the body rotates down and the back bends to allow hindlimb touchdown [44]. In fact, forelimb fractures (38.5 %) are less common than hindlimb fractures (61.5 %) in falling cats [35], highlighting the tendency to use the hindlimbs at higher drop heights. Therefore, in cats, posture dependent actuation prior to touchdown allows the animal to tune the distribution of energy absorption between forelimbs and hindlimbs after touchdown. EMG data show that cats have a generalized motor program that is agnostic to drop height and is used to activate extensor muscles at the elbow joint during the pre-landing phase of self-initiated jumps [45, 46]. In addition to pre-touchdown muscle activity and limb coordination, cats also possess passive, post-touchdown landing mechanisms. In particular, they show a remarkable multilevel energy buffering system for shock absorption that includes paw pads, limb bones, and coordinated joints complementing each other [47]. These results have inspired the design of energy dissipation pads [48] and suggestions for legged landing robot design [49] Further definition of the complete energy buffering system used in squirrel landing will likely lead to additional inspiration.

In cane toads, Azizi et al. (2014) showed that rapid modulation of hindlimb flexion during the aerial phase of a hop could shift the COM anteriorly and reduce torque by aligning the COM with the GRF vector [40]. A similar study using the same species of Cane toads (Bufo marinus) performing controlled landings found that toads use their forelimbs exclusively to decelerate and stabilize the body after impact [38]. By having animals jump from platforms of different heights, they showed that toads achieve dynamic stability across a wide range of landing conditions. Specifically, Cox and Gillis (2017) found that torques during landing could be reduced by a landing preparation motor control strategy for aligning the forelimbs with the body's instantaneous velocity vector at impact (impact angle). As in our squirrels, these two toad studies together show the importance of CG alignment with both velocity and GRF vectors.

Energy absorption can also occur during flight prior to touchdown. In flying squirrels for example, landing force is negatively correlated with glide length [19]. Longer glides allow more time for animals to reach body orientations where they can use aerodynamics to decrease landing velocity, and thus landing forces. In fact, Paskins et al. (2007) suggested flight in flying squirrels may have been selected to control landing forces [20]. A study on birds by Provini et al. (2014) determined that the hindlimbs of zebra finches and diamond doves produce 1.4-2.6 bw forces during landing [50]. It was estimated that for both species, the hindlimbs reduced landing velocity by 60%, thereby contributing substantially to the absorption of kinetic energy after touchdown. The flying robot SNAG (stereotyped nature-inspired aerial grasper) incorporated an independent passive energy absorption for each leg [51]. We surmise that the rich morphology of squirrel paws almost certainly contributes to passive energy management upon landing and deserves further attention.
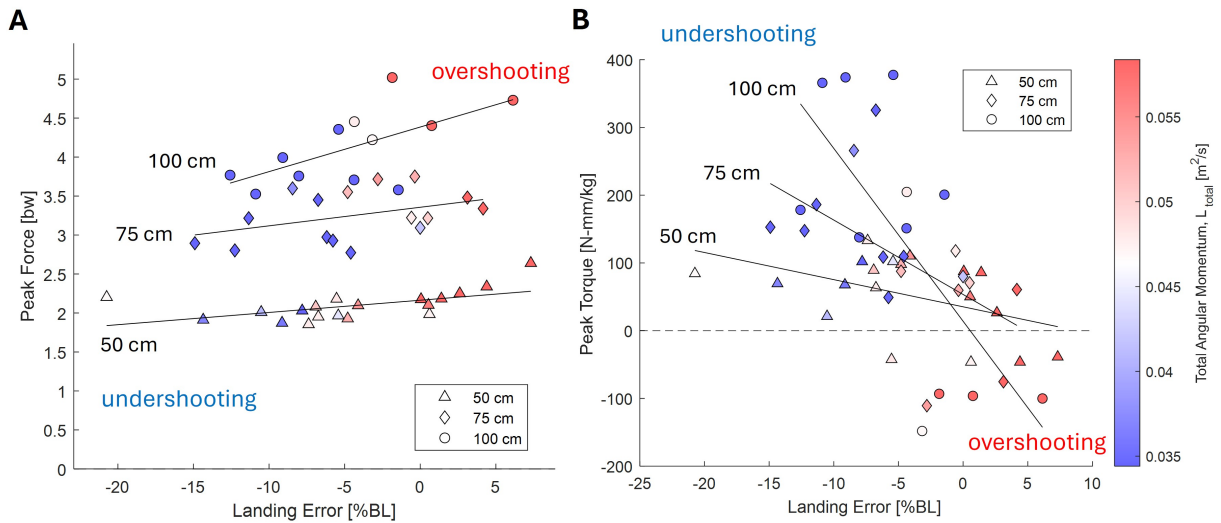
Figure 2.7: **Squirrel peak force data vs. landing error and angular momentum as a function of gap distance.** (A) Squirrels tend to apply higher peak forces the more they overshoot [linear mixed-effects model controlling for gap and individual, $t(1,45) = -3.4$, ** $p = 0.0015$]. (B) Squirrel peak torque data vs. landing error and angular momentum are plotted for each gap distance. Squirrels tend to apply higher torque the more they undershoot [$t(1,45) = -3.7$, *** $p < 0.001$].

Landing stabilization by control of leg force and foot torque

Spring-loaded inverted pendulum (SLIP) models have long been used to test hypotheses for stable walking and running in animals [52, 53, 54]. and a whole host of robots [55, 56]. Squirrels, cats, anurans, and birds alike rely on their limbs to manage landing energy post-touchdown, regardless of their ability to control touchdown speed prior to touchdown, and therefore variations of spring-loaded inverted pendulum models could be useful to understand landing. Zhang et al. (2014a) examined energy absorption and control by spring-mass modeling the front limb behavior of cats jumping down from 1.8 m high platforms onto a force plate [37]. Toad [38] and frog [57] (Nauwelaerts & Aerts, 2006) landings after a hop used versions of spring-damper models to determine the alignment of forelimbs at impact and their angle for effective energy absorption. Birds have been studied using spring-mass models to design a flying robot that could perch on branches using an under-actuated, dynamic grasper [51]. Using a spring-mass model, they defined a "perching sufficiency region". They found that the primary perching failure mode of slipping too far forward or back could be quantified by angular momentum about the branch, which is a function of mass distribution, velocity, and body angles relative to the perch.

Taking a similar approach, we used an extensible pendulum model developed by Yim et al. (in prep) for above-branch landing of the monopedal robot Salto, after a jump from another branch. Yim et al. (in prep) proposed two adaptive control strategies that squirrels

may be utilizing upon touchdown: leg force control and body torque control. Their control hypotheses are summarized in Fig. 2.3B, and they are as follows. All else being equal, they postulate that when an overshoot landing error is present (Fig. 2.1, lightest red sector), an extensible pendulum can achieve balance by generating a greater leg force to prevent shortening as well as applying a CCW (counterclockwise) torque to brake (Fig. 2.3B, overshoot). Preventing shortening or even lengthening the legs during an overshoot can increase inertia, thereby decreasing angular velocity to slow down the swing up. When an undershoot landing error occurs (Fig. 2.1, lightest blue sector), an extensible pendulum could achieve balance by producing less leg force and shortening toward the branch as well as applying a CW (clockwise) torque to pull up (Fig. 2.3B, undershoot). Shortening legs can decrease inertia, thereby increasing angular velocity to speed swing-up. Adding leg or radial force control to torque-based balance has been shown to expand disturbance rejection [58] and improve balance capture regions available to pendulum models using vertical motion [59]. Using balancing strategies with support forces and torques can assist by adjusting linear or angular momentum [60, 61].

Attempting to apply the landing control hypothesis revealed that all else is not equal for the jumps at our three gap distances. Specifically, landing speed and velocity angle were significantly different at each gap distance, resulting in variation in both landing error and angular momentums (See Table 2.2). The larger variation in peak force and torque in Fig. 2.5 is likely because longer gap distances are required for higher take-off and landing speeds. We postulate that this variation in touchdown states across gaps also explains the increasing variation in peak force and torque. The space of stable above-branch landings is set by landing error and total angular momentum. A sequence of snapshots for a characteristic undershoot and overshoot trial are illustrated in Fig. 2.3A. The relationship between wrench and landing type indicates that fewer adjustments are necessary for a nominal landing (Fig. 2.1, white center sector) where the landing error is small and negative while the angular momentum is moderate. In this instance, a squirrel can passively use moderate post-impact angular momentum to compensate for the small, negative landing error, resulting in swinging up towards a balanced posture without the need for significant adjustments. However, when the magnitude of landing error increases, greater adjustments are necessary. For example, when the landing error is large and positive such that the ballistic trajectory of the CG is above the branch, total angular momentum is also high (Fig. 2.7AB in red). Under these overshoot conditions, we predict that the landing will be stabilized by the squirrel if it generates a large leg force (Fig. 2.7A) and a CCW braking body/foot torque (Fig. 2.7B). Likewise, the landing trajectory of the CG could be significantly below the branch (large, negative landing error) and the total angular momentum could be small (Fig. 2.7AB in blue). Given these undershoot conditions, we predict that a squirrel will achieve landing stabilization through generation of a lower leg force (Fig. 2.7A) and a CW pull up body/foot torque (Fig. 2.7B). Furthermore, at the gap distance of 100 cm, both peak force and torque seem to be most sensitive to landing error. In other words, for the same landing error but faster landing speed, even more adjustments in force and torque may be necessary for stable above-branch landing.

2.5   Squirrel-inspired Gripper

Different from many arboreal primates with opposable thumbs and prehensile tails, tree squirrel foot morphology includes elongated digits with ridgeless foot pads and unfused volar pads [62]. These adaptive features, coupled with the squirrels' high arboreal agility, make referencing their foot engagement during landing and walking particularly compelling. Notably, non-prehensile gripping is commonly observed when fox squirrels land on rods, as seen in Figure 2.8. In pilot field trials, we found initial grasp time of the squirrel to be around 10 ms [63]; this is faster than typical muscle activated reflexes [64], indicating that morphological computation plays a role in foot behavior. Therefore, we study fully-passive tendon-driven mechanical foot actuation as a means to support stable landing.

The SQRT grasper is designed to study mechanical features relevant to agile non-prehensile landing and grasping on curved surfaces. This testbed enables us to alter the springs at each joint and attach and detach finger pads in a modular way to explore and fine-tune individual parameters such as joint stiffness, friction, and damping.

An underactuated digit of the SQRT grasper, as shown in Fig. 2.9A, consists of four rigid acrylic segments connected by pin joints. The lengths of each individual segment decreases from proximal to distal (4.6, 4.0, 3.4, and 2.8 cm, respectively). We select a specific stiffness at each pin joint by attaching an extension spring, such that a resistive torque is exerted linearly with respect to joint angle. The distal joint is stiffer than the proximal and medial joints ($k_3 > k_1$, k_2) so that flexion of the digit occurs at the proximal joint before distal curling. Furthermore, each joint has a hard stop or "joint lock" to prevent finger hyperextension. Finger pads are optionally included by attaching 2 cm thick high-density foam to each segment with sewing string, functioning as a proxy for the damping and elasticity properties of squirrel volar pads.[1] ArUco tags are affixed to each of the four

---

[1]We do not match any specific physical characteristics of real volar pads. We only look at the introduction or absence of compliant pads.
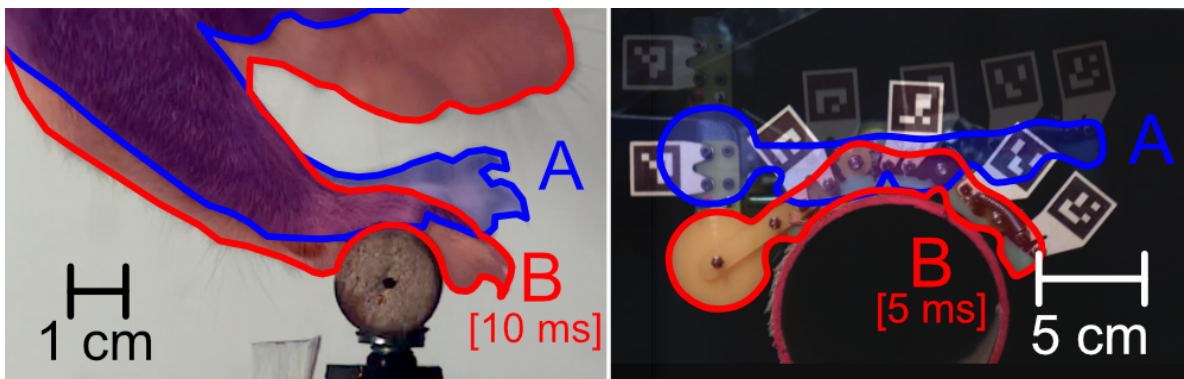
Figure 2.8:   **Non-prehensile grasp for stable landing on a thin curved substrate exhibited by a squirrel and our robot.** Blue outlines labeled A denote the pose of the paw at initial contact, and red outlines labeled B denote the pose of the paw in a stabilized grasp, 5-10 ms after touchdown.
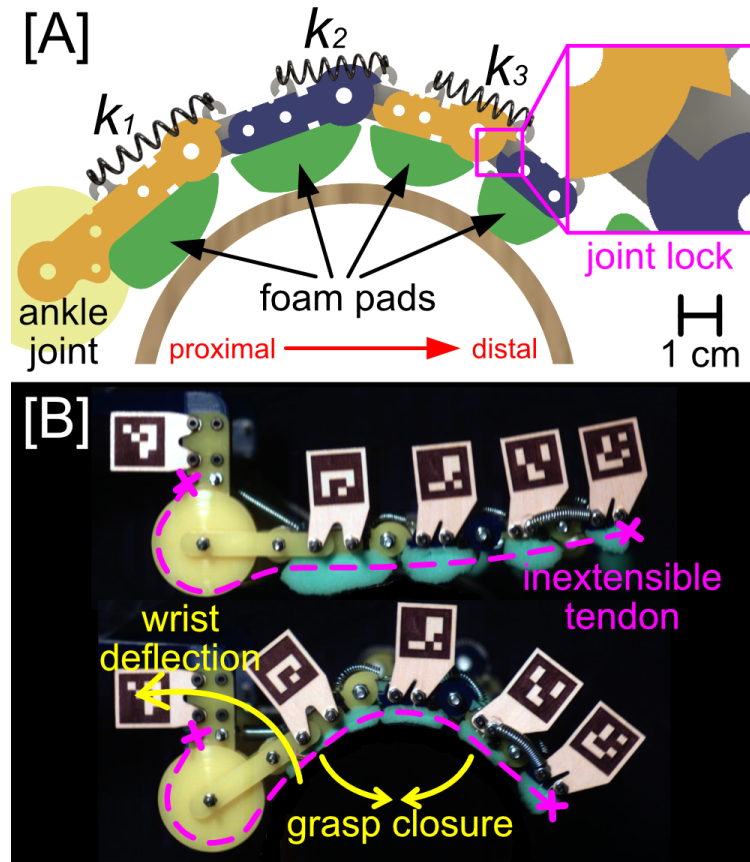
Figure 2.9: **Implementation of SQRT (SQuirrel-inspired Rapid Tenodesis foot).** (a) Schematic of the four-segment digit with three spring-loaded joints $\{k_1, \ k_2, \ k_3\}$. Foam pads are attached for grip and damping during landing impact (b) Passive grasp actuation driven by a tenodesis action. An inextensible tendon routed through the digit allows for grasp closure to be coupled to wrist deflection.

segments to measure their motions.

The overall digit is driven by a tendon, as shown in Fig. 2.9B, which is an established mechanism for underactuated robot fingers [65]. The tendon is an inextensible string fixed at the tip of the distal digit, routed beneath each segment,[2] and subsequently affixed around a circular wheel of 2 cm radius which acts as an ankle joint. This tendon imposes a kinematic constraint (tenodesis action) on the structure where a deflection of the ankle causes a closure of the digit. This actuation mechanism allows the digit to close passively as the ankle joint rotates due to the weight of the robot and impact force of landing.

---

[2]The effective moment arm at each interphalangeal joint is 0.75 cm

Robot Methods

We construct a lander apparatus with SQRT digits to test its capability to passively land stably on rods whose circumference is at least double of the finger length. SQRT consists of two identical tendon-actuated digits arranged in parallel 8 cm apart to prevent out-of-plane tipping and approximate a 2D landing case. A mass is attached above the foot such that the center of gravity G is positioned approximately over the center of the digits. The overall weight of this assembly is $M = 1.5$ kg.

We examine three parameters of interest: (1) contact friction, (2) damping of pads, and (3) stiffness of digit joints. (1) is motivated by the static sufficiency region model. (2) is motivated by the hypothesis that soft volar pads, like those on squirrel feet, play a role in stable non-prehensile landing. (3) is tested because overall digit stiffness trades off the ease of passive curling with natural frequency, which influences final foot pose and bouncing of the toes during dynamic impact. We examine six testing conditions as given in Table 2.3 to explore various permutations of these design parameters.

Table 2.3: **SQRT Digit Test Conditions**

Test	Joint Stiffness $[N/m]$			Configuration		μ
	k_1	k_2	k_3	Grasper	Substrate	
A	20	22	70	No Pad	Cardboard	0.2
B	20	22	70	No Pad	Rubber Tape	2.2
C	20	22	70	Foam Pads	Grip Tape	3.0
D	37	40	140	No Pad	Cardboard	0.2
E	37	40	140	No Pad	Rubber Tape	2.2
F	37	40	140	Foam Pads	Grip Tape	3.0

Joint stiffness is varied by swapping the springs at each joint, with tests (D, E, F) having approximately double the stiffness of tests (A, B, C). Damping is varied through inclusion (C, F) or exclusion (A, B, D, E) of foam pads on the SQRT digit. Friction is varied through the application of different materials to the surface of the landing rod, and is also influenced by the foam pads. While varying friction on the grasper directly may be more practical in field settings, it is quicker to vary the substrate properties directly in these experiments. Trials where low friction was desired (A, D) were performed with the smooth cardboard surface of the rod. For trials without pads (B, E), a soft rubbery tape is applied to the rod to ensure sufficient friction with the acrylic mechanism. For trials with foam pads (C, F), a 60 grit grip tape is applied to the rod to ensure adequate friction. The friction coefficient for each configuration is experimentally determined. The rod size is always kept constant at a diameter of 11 cm, approximating the same length scale between squirrel toes and branches found in natural arboreal habitats.[3]

---

[3]We leave flat, small, and irregular landing surfaces for future work.
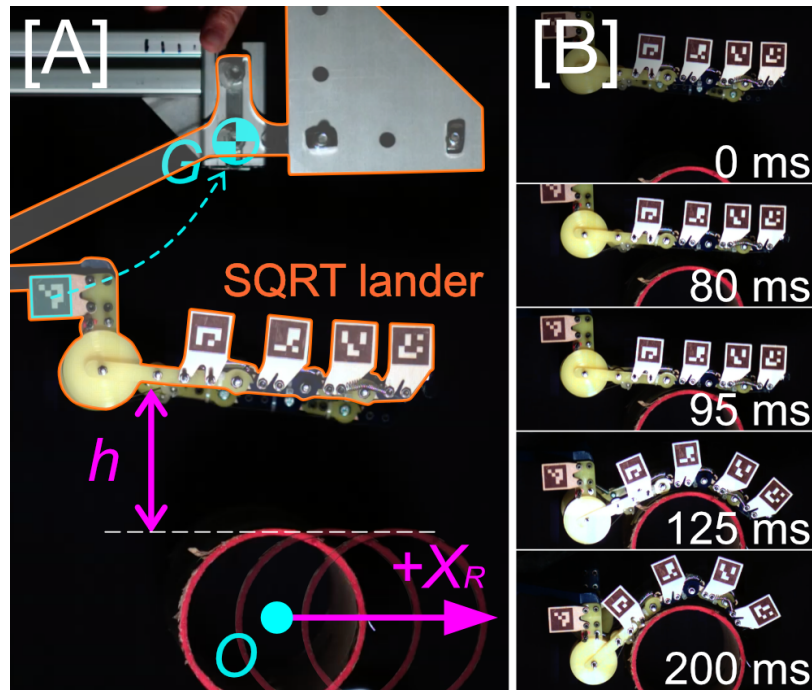
Figure 2.10: (a) Experimental apparatus for vertical impact of the lander with a curved rod. Horizontal position of the rod (X_R) and drop height (h) are varied. (b) Sequence of a characteristic drop and stable landing.
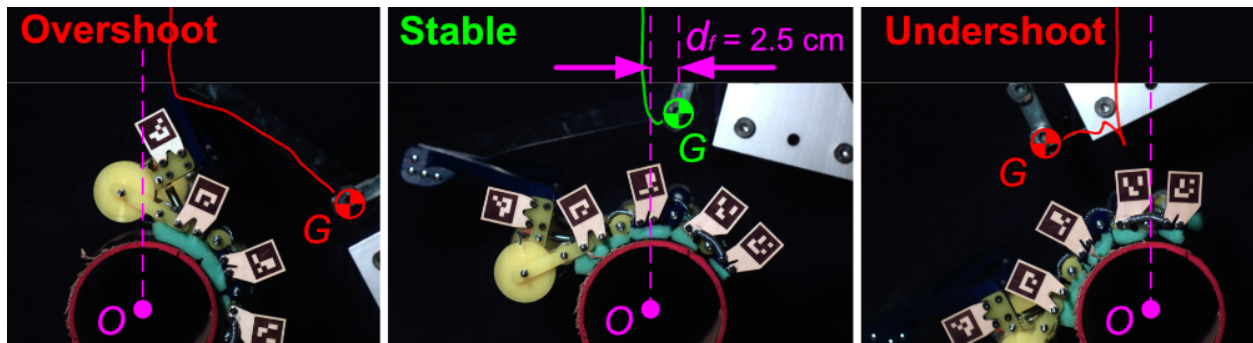
Figure 2.11: Characteristic center of gravity (CG) trajectories during landing showing overshoot, stable landing, and undershoot behavior.

Dynamic landing experiments are conducted by dropping the SQRT grasper onto the rod from a given drop height (h) and rod location (X_R). These initial conditions are varied using an adjustable 80/20 aluminum frame, as shown in Fig. 2.10A. SQRT begins held in a 5 cm vertical linear rail by hand. Once released, it accelerates vertically downward in the rail, exits the rail and enters freefall, before impacting the rod. Drop height h is measured as the distance between the top of the landing rod and position of the SQRT digit at release. The contact location $X_R = 0$ is defined where the points G and O are vertically aligned along the $\hat{y}$ direction before SQRT is released.

A high-speed camera (Phantom V10, Vision Research) records each landing sequence at 978 frames per second. Fig. 2.10B shows the sequence for a characteristic stable landing consisting of release (0 ms), freefall, initial contact (95 ms), initial grasping (125 ms), and complete static stabilization (200 ms). OpenCV is used to track the poses of each ArUco tag attached to the digit. The base tag at the wrist of the digit is used to estimate the location of the center of gravity G.

Landing stability is defined by the overall trajectory of the center of gravity G, as shown in Fig. 2.11. A characteristic stable landing consists of the settling of G to a static pose above the rod, while unstable landings result in the deviation off the rod (overshoot/undershoot). For stable landings, we measure d_f, the offset of G from the center of the rod O once a static pose has been achieved. For unstable landings, d_f is recorded as the last recorded position of G, about 200-300 ms after touchdown; in these cases, the term d_f does not represent a static pose since G remains in motion until SQRT slides off.

We borrow the term "sufficiency region" as introduced in [51] to denote a range encompassing a particular parameter space where stable landings occur. We vary (h) from 10 to 40 cm and (X_R) from -2 to 3 cm. For each condition of drop height and contact location tested, we perform 5+ trials to observe stability. We utilize motion tracking to then determine the static stability range by measuring the post-landing d_f across all trials.
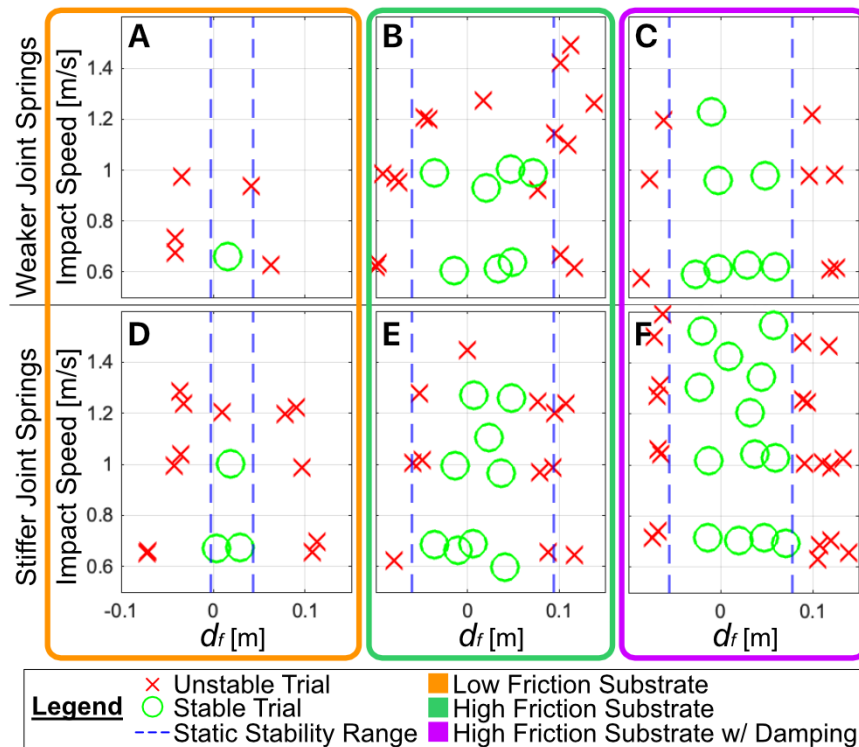
Figure 2.12: **Landing kinematics.** All dynamic landing trials showing impact velocity and final recorded pose (d_f, distance between lander CG and the center of the branch). The static stability range is offset from zero due to the lander's asymmetry.

We translate data from the input test parameters into impact speed and final post-landing static posture in Fig. 2.12. Both damping and joint stiffness play a role in increasing stability for higher impact speed landings. The range of d_f for stable dynamic landing trials appears largely independent of impact speed until a maximum tolerable speed in A, B, D, and E. At these lower speeds, there is agreement between the empirical static stability range, denoted in dashed vertical lines, and dynamic landing successes. At higher impact velocities, the recorded position after 200-300 ms may remain within the static balance range, but SQRT still eventually slides off of the rod. This indicates that there is ongoing movement, likely in vertical bouncing, since horizontal movement is small.

2.6 Conclusion

In summary, our measurements on free-ranging squirrels shed light on their remarkable landing dynamics, uncovering findings that govern their agility and stability in arboreal environments. Along with general gap effects on landing kinetics, our investigation revealed three discoveries. First, squirrels exhibit rapid and precise landings, primarily utilizing their forelimbs to manage landing energy. Second, their ability to align velocity and force vectors along the limb becomes more pronounced as landing speed increases, reflecting an adaptive strategy for managing landing energy. Third, the variability in peak force and torque is consistent with the control of overshooting and undershooting the landing target, suggesting squirrels use radial leg force and body-foot/torque to adjust their landings actively. Specifically, squirrels employ substantial braking forces and torques when overshooting, while utilizing lesser leg force and pull-up torques to correct for undershooting.

Further exploration is warranted to deepen the understanding of squirrel landing dynamics. The SLIP model and the cylindrical approximation of the squirrels' bodies at touchdown pose modeling limitations, primarily the omission of joints throughout the body like the variable curvature of the spine, head, limbs, and tail. XROMM data could reveal the utility of modeling several degrees of freedom. One example could be in revealing the stabilizing function of the shoulder and back as suggested in cats [37]. Kinematic analyses encompassing the entire time series could elucidate the changes in leg length over time, offering valuable insights into how leg force adjustments contribute to leg length changes and the correction of landing error. Additionally, investigating the effects of foothold parameters such as size, curvature, and friction on landing control could provide a comprehensive perspective on the adaptability of these findings in different environments.

The implications of the present findings extend beyond the realm of squirrel biomechanics. Advancements in the field of aerial robotics have demonstrated robot abilities such as landing dynamically and perching on cylindrical substrates using specialized grippers [51, 66, 67, 68]. These specialized mechanisms ensure anchoring to the substrate and enhance stability during critical landing phases. Specialized gripper designs could be integrated into quadruped robots, which have demonstrated dynamic capabilities like walking across bricks [69], walking along a thin walkway [70], and even jumping/landing optimally on flat surfaces [71, 72].

However, implementation of foot designs more complex than wheels or spheres remains an open challenge due to the complexity of modeling multiple contacts for legged robot control.

One way we can complement and simplify control is by designing passive feet using compliant structures that react to substrate forces such as bistable mechanisms [25], finray designs [73, 74], and multi-segment tendon-driven feet [75]. Our latest work examines the effect that stiffness and damping have on tendon-driven feet for dynamic branch landing [76]. These passive foot designs simplify legged robot control, and they have the potential for becoming useful for dynamic grasping and detachment for agile robot locomotion on sparse terrains. Exploring the scalability of these control strategies from diverse biological systems holds promise, particularly in the domain of quadruped robot locomotion. The landing mechanisms inherent to squirrels, manifested in their body, limbs, and feet, could provide inspiration for the design and control of innovative, agile, legged robots equipped with the ability to rapidly traverse sparse terrains for societal benefit.

Our squirrel-inspired passive lander, SQRT, quickly adapts to a rod, applying a non-prehensile grasp to support stable, passive landing. We focus here on non-prehensile gripping to emulate a common grasp type that enables squirrels to achieve agility, especially when navigating irregular surfaces and enduring high-impact locomotion. While there is a clear distinction between a squirrel's complex multi-limb landing and our robotic grasper's vertical landing and simplified implementation, our experiments provide a foundation for refining foot design aimed at sparse terrain navigation. In particular, we found that joint stiffness, friction, and inclusion of damping finger pads can all play a role in landing stability on rods. This emphasizes the diverse end-effector design possibilities in the realm of agile legged robots.

Chapter 3

Adaptive Haptic Search with a Suction Cup

We now shift our focus to a different adaptive control system for grasping objects with a different type of nonprehensile gripper - suction cups. Suction cups are an important gripper type in industrial robot applications, and prior literature focuses on using vision-based planners to improve grasping success in these tasks. Vision-based planners can fail due to adversarial objects or lose generalizability for unseen scenarios, without retraining learned algorithms. We propose haptic exploration to improve suction cup grasping when visual grasp planners fail. We present the Smart Suction Cup, an end-effector that utilizes internal flow measurements for tactile sensing. We show that model-based haptic search methods, guided by these flow measurements, improve grasping success by up to 2.5x as compared with using only a vision planner during a bin-picking task. In characterizing the Smart Suction Cup on both geometric edges and curves, we find that flow rate can accurately predict the ideal motion direction even with large postural errors. The Smart Suction Cup includes no electronics on the cup itself, such that the design is easy to fabricate and haptic exploration does not damage the sensor. This work motivates the use of suction cups with autonomous haptic search capabilities in especially adversarial scenarios.

3.1 Introduction

Vacuum grippers, or suction grippers, are widely used in industry for simple pick and place operations. Relying on negative internal pressure that forms when sealed against a surface, the suction gripper can gently handle an object without applying squeezing force, which allows an astrictive handling of various types of objects. If the item to be grasped is smooth and well modelled, as in manufacturing lines, the gripper can repeatably and predictably handle it with high reliability. However, for grasping in unstructured environments, e.g., in e-commerce warehouses, objects vary dramatically and present many different surface conditions that may or may not be easy to visually perceive or grip with a suction cup. Careful
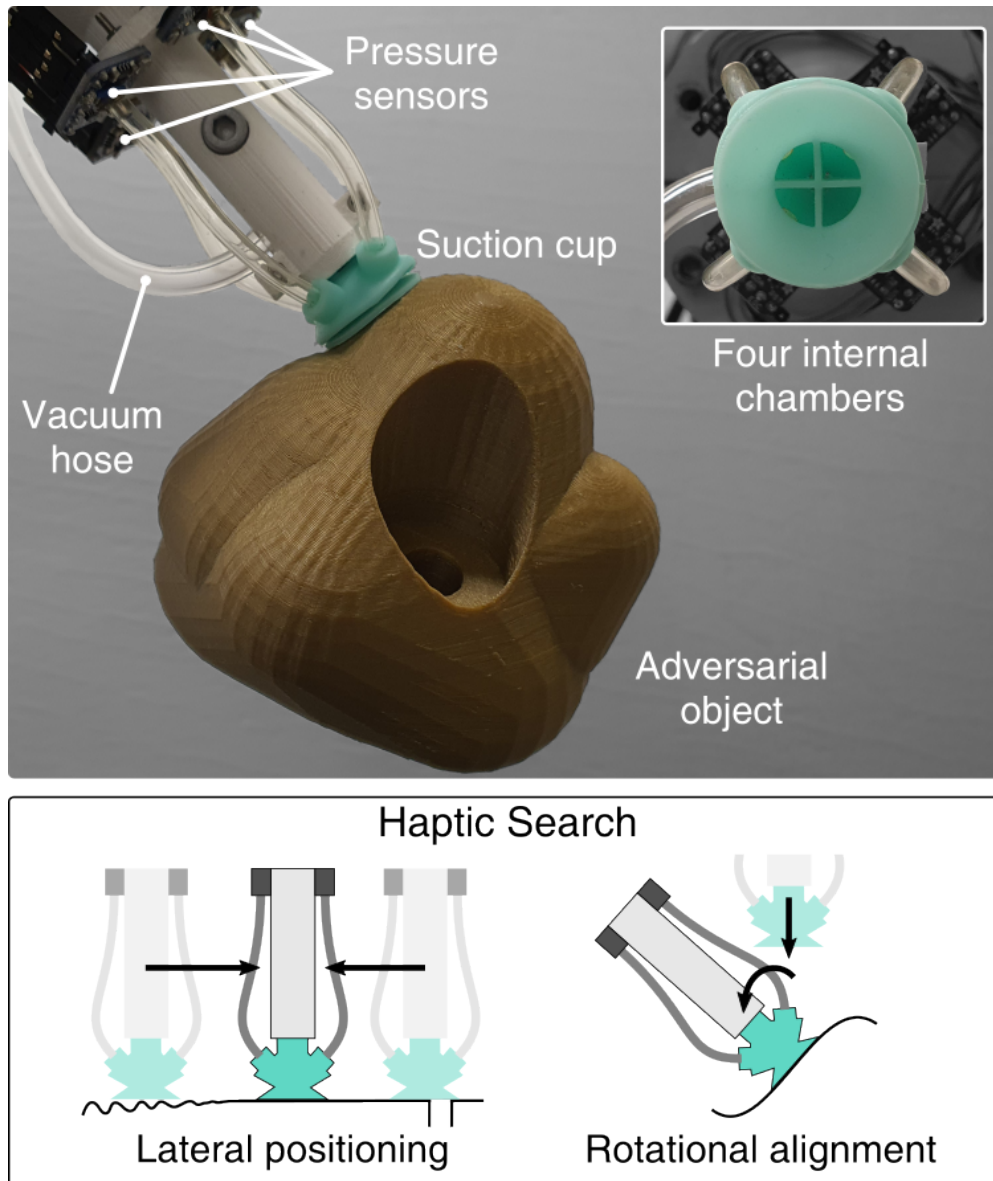
Figure 3.1: **The multi-chamber Smart Suction Cup grips an adversarial object.** The cup has four internal chambers, each connected to a pressure transducer that provides a measure of internal flow rate. It is able to localize small breaks in the seal due to, for example, the rugosity (e.g., wrinkles, bumps, etc.) of the object surface. Haptic search can allow for successful gripping even when the initial grasping point fails, important for visually-adversarial objects.

planning of grasp contact location is therefore important, and methods for doing so have been widely studied for the past few years. While there have been successful demonstrations of versatile suction grasp planners, these methods often rely on vision, which may not capture fine object details of the geometry and lead to suction failure. Moreover, pre-trained models are typically specific to certain suction cup and camera configurations, making it challenging to transfer these methods to different hardware setups without retraining. Time-consuming retraining currently presents a barrier to adoption.

To address these challenges, we propose the use of autonomous haptic search – or the repositioning of the cup using contact measurements – to supplement vision in suction grasping. This new approach leverages pre-trained vision-based grasp planners to obtain an approximate solution before then fine-tuning the pose after contact occurs until the grasp succeeds. For this method to be effective, we assume that a successful grasp point is close to the pre-trained planner's solution even when errors emerge, as the planner already considers key factors of graspability such as the object's weight distribution and the suction seal formation of a similar suction cup. To adjust the contact location, we use haptic exploration driven by flow-based tactile sensors on our Smart Suction Cup, first presented in [77]. This design has the advantage of no electronics embedded in the cup itself, but remote sensors can still provide valuable information about local suction leakages to overcome grasp failures.

Overview

Section 3.2 provides a review of related works. In Section 3.3, the Smart Suction Cup is described along with computational fluid dynamics models to demonstrate the expected signals; this design and flow analysis was previously presented in our prior work [77]. In the current work, we evolve this concept substantially beyond the prior work by now introducing and implementing autonomous haptic search. Section 3.4 presents our new proposed haptic search algorithm that utilizes the flow readings to improve grasping on adversarial objects. Experimental setup and procedures are described in Section 3.5, including both sensor characterization on primitive fixed objects and a bin-picking task with loose adversarial objects. Section 3.6 presents the results of these experiments; overall, we find that the use of the Smart Suction Cup haptic algorithm provides useful controller estimates and more successful grasping. Discussed in Section 3.7, the model-based haptic exploration encounters failure modes that can be further improved in future work.

The contributions of this paper are as follows:

1. Presentation and characterization of the first Smart Suction Cup that can sense local suction seal leakage on flat and curved surfaces by using remote pressure sensors.

2. Design of a suitable model-based haptic search controller using tactile sensing feedback to improve suction seal in real time.

3. Bin-picking experiments to evaluate performance across adaptive control algorithms with comparison to an existing vision-based grasp planner.

3.2 Related works

Suction grasp planning using vision

One major challenge in suction grasping is how to plan a contact location. Examples of planning methods include the heuristic search for a surface normal[78] and neural network training of grasp affordance using binary success labels[79]. Wan et al. (2020) use CAD model meshes to plan a grasp resisting gravitational wrench[80], and Dex-Net 3.0 learns the best suction contact pose from a point cloud considering both suction seal formation and gravitational wrench resistance[81]. Using a similar approach to Dex-Net, Cao et al. (2021) built a larger suction grasp dataset including RGB images and annotations of a billion suction points[82]. Using physics simulation, Shao et al. (2019) demonstrated a self-supervised learning method that finds suction grasp policies from RGB-D images for cluttered objects[83], and Cao et al. (2022) improved it by implementing dense object descriptors[84]. These aforementioned methods rely on RGB or depth sensors, which may not perceive fine details critical to suction success, e.g., texture, rugosity, porosity, etc. Vision can also become occluded in cluttered environments and heavily distorted with reflective or transparent objects.

Suction cup tactile sensors

Prior tactile sensors designed for use in suction cups provide partial information about object properties and vacuum sealing state. Researchers employ strain sensors on a suction cup by coating PEDOT [85] or carbon nanotube [86], or by installing microfluidic channels filled with carbon grease [87]. These strain sensors measure suction deformation during surface contact, estimating the compression forces and load distributions of suction cups [85], surface angles and stiffness [87], and object weight and center of gravity [86]. Alternatively, the contact of the suction cup can be measured indirectly by proximity sensors, including a capacitive base plate [88], inserted fiber optic cable [89], and micro-LIDAR [90]. However, these methods provide information about the cup deformation and surface proximity, which may not always correspond to a suction seal formation that is subject to fine local geometry and porosity. For direct contact sensing, Muller et al. (2017) report a thin pressure sensor array attached to the suction cup lips, measuring the distributed contact pressures [91]. However, the sensor film on the contact layer may weaken the suction seals.

Another straightforward approach is to monitor the internal vacuum pressure of the suction cup as a discrete measure of suction sealing, as in [92]. However, this prior implementation method does not localize the source of a leak around the lip's edge or measure local surface geometry, which is critical for adaptive haptic exploration for a better grasp.

Adaptive Regrasping using Tactile Sensing

Robust grasping in real-world scenarios has driven research in adaptive regrasping using tactile sensing. Due to uncertainties in vision systems and difficulties capturing detailed object features, tactile sensors are employed to detect contact information and guide improvements in response to unsuccessful grasps. Adaptive regrasp research has predominantly focused on friction-based grippers rather than suction grippers. Simple regrasping approaches include increasing grasp forces or grasp impedance upon detection of perturbations, such as external forces causing slips[93, 94]. For multi-finger grippers, researchers have demonstrated finding better grasping points through finger gaiting [94]. These methods primarily aim to improve handling or increase the stability of objects already held by the gripper. In object-picking processes, deep learning or reinforcement learning techniques have been employed to process complex tactile sensor data. Chebotar et al. (2016) used a multi-finger gripper with a Bio-Tac sensor to demonstrate regrasping of a simple cylindrical object; they analyzed complex spatiotemporal tactile sensor information with PCA and learned a regrasp policy to update the pose[95]. Reinforcement learning was also used to learn hand grasping and regrasping policies in simulation, which are then effectively transferred to real robots [44]. For parallel jaw grippers, vision-based tactile sensors, such as Gelsight, have been used[96, 97]. In [96], the researchers trained a grasp quality metric from a given tactile image and simulated possible image shifts to guide the best regrasping policy. In [97], they directly trained for the best action to achieve the highest grasp success, which could be either a regrasp or pick.

The majority of the approaches mentioned above rely on tactile sensing information processed by deep learning or reinforcement learning algorithms. These methods can be unintuitive and may require significant training data for generalization. These approaches may involve fully reopening the gripper during regrasp actions, which can be time-consuming. Moreover, theses approaches may not be applicable to suction grasping due to differences in grasping mechanisms. In the following sections, we will present a physics- or intuition-based regrasping controller for suction cup grippers, enabling generalization without requiring extensive training data. Our controller operates without losing contact, potentially reducing operation times. To our knowledge, no existing literature addresses adaptive regrasping for suction cup grippers.

3.3 The Smart Suction Cup

The Smart Suction Cup utilizes internal airflow estimates to monitor local contact conditions. Internal wall structures separate the internal cavity of the suction cup into four chambers (Fig. 4.1) – one for each cardinal direction. Overall suction airflow is therefore separated between each chamber and the pressure sensor connected to each chamber provides an estimate of the local flow rate. We implement the wall structure inside a single-bellows suction cup for its versatility on different curvatures and orientations of objects. The internal wall structure only spans the proximal portion of the suction cup, in order to maintain typical

flexibility, deformation and seal formation at the distal lip. As shown in Fig. 3.2a-b, the suction cup is mounted to an end effector fixture piece and connected with pressure transducers and a single vacuum hose with pressure regulation. For experimental trials, this end effector is integrated with a universal robot arm. Dimensions and internal geometry of the compliant cup are shown in Fig. 3.2c. A single prototype is used throughout experimental testing, without incurring damage or needing replacement.

Fabrication

We fabricate this 3D rubber structure including the chamber walls as in Fig. 3.3, with a single-step casting of silicone rubber. The casting mold comprises three parts, two outer shells and one core, that are 3D printed using an SLA 3D printer (Formlabs, Form2). These are assembled together using stainless steel dowel pins and bolts. To ensure the clean casting of the thin internal wall structures (0.8 mm thick), we used a syringe with a blunt needle (gauge 14) to inject uncured RTV silicone rubber (Smooth-On, MoldMax 40) and then vacuum-degassed it. After curing, the outer shells are removed and the silicone suction cup is stretched and peeled off of the inner core mold. Tearing of the silicone can occur during this step, especially with harder rubbers. Cast flashing around the lip of the cup can occur at the interface between the core and outer shells; deflashing is performed manually after demolding using a razor blade.
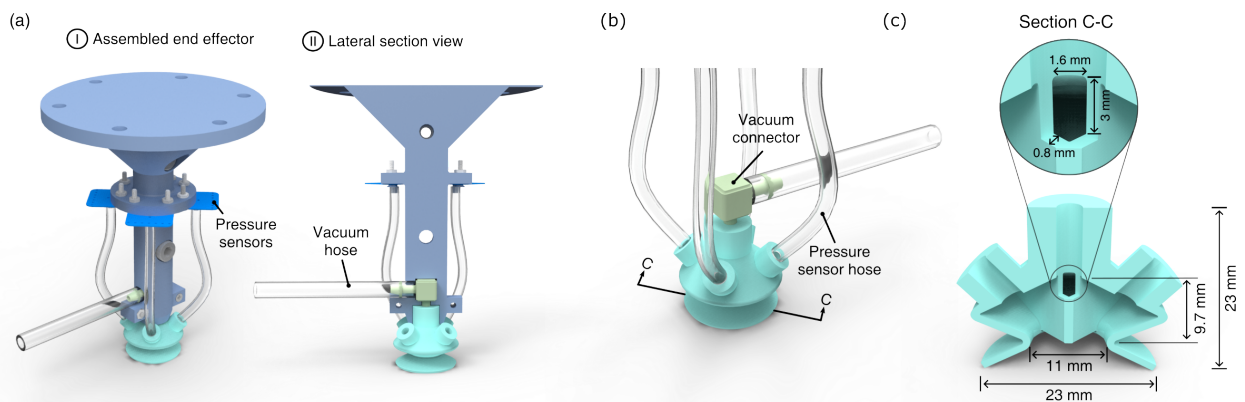
Figure 3.2: **Design of the end effector and the suction cup.** (a) The end effector integration with the suction cup. (b) A close up of the suction cup shows how it is connected with a vacuum connector and hoses to the pressure sensors. (c) Cross-sectional view of the suction cup shows internal and outer dimensions.

CFD Simulation

Using Computational Fluid Dynamics (CFD) simulation (COMSOL Multiphysics, $k - \epsilon$ turbulence model), we evaluate the gripper in two example suction flow cases: *vertical* and *horizontal* flow (Fig. 3.4a and b, respectively). The vertical flow case emulates when the suction cup only partially contacts a surface, or when the surface's shape inhibits sealing. However, when the suction cup engages with a smooth flat surface, flow can only move inward from the outer edges of the cup, as in the horizontal flow case. This horizontal leak is common as the suction cup is wrenched from the surface after a suction seal is formed. Although the suction cup will deform under vacuum pressure, we use modeled rigid geometry in the CFD simulation. For each case, we approximate the leak flow direction with a small pipe (D = 1 mm, L = 7 mm) intersecting with one of the internal chamber volumes as shown in Fig. 3.4a-b. The boundary conditions of the vacuum pump pressures and flow rates match the experimental setup.

The simulation results suggest that the gripper can detect leakage flows using differences between the four pressure transducers. We defined vacuum pressure (P_{vac}) as

$$P_{vac} = P_{atm} - P_{chamber} \tag{3.1}$$

where P_{atm} is atmospheric pressure. In the vertical leakage flow case, P_{vac} close to the leaking orifice shows the least vacuum pressure than the others (Fig. 3.4c). On the other hand, the horizontal leakage causes the diagonally opposite channel to have the lowest P_{vac} (Fig. 3.4d). These trends are supported by the flow results in Fig. 3.4e-f, where the vertical
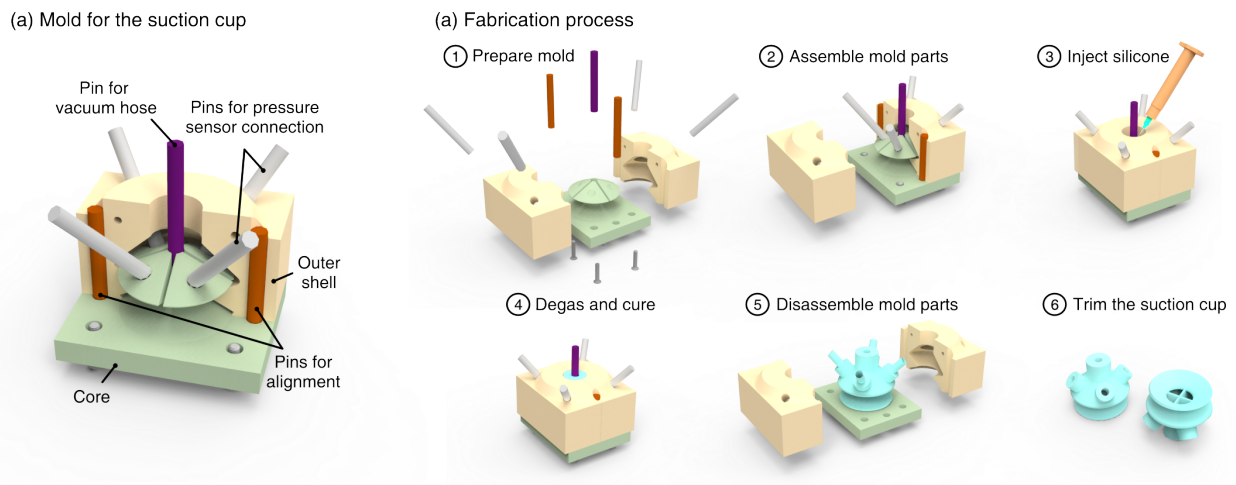
Figure 3.3: **Casting mold and fabrication of the suction cup.** (a) The casting mold has three parts (2 Outer shells and 1 core). Molds are aligned and fixed by pins and bottom bolts. (b) The fabrication process of the suction cup.

and horizontal orifices produce the highest flow rate in opposite chambers. The simulation result also shows an estimate of the pressure difference between chambers (∼0.4kPa) which must be resolved by the selected pressure sensors.

System integration

Four ported pressure sensors (Adafruit, MPRLS Breakout, 24 bit ADC, 0.01 Pa/count with an RMS noise of 5.0 Pa) connect with the four chambers of the smart suction cup via polyurethane tubes. The suction cup and the pressure sensors attach to a 3D printed fixture (Fig. 4.1a) and this fixture is attached to the wrist F/T sensor (ATI, Axia80, sampling rate 150 Hz) on the robot arm (Universal Robots, UR-10) as in Fig. 3.5. A microcontroller (Cypress, PSoC 4000s) is fixed to the arm proximal to the load cell and communicates with the four pressure sensors via I2C at a 166.7 Hz sampling rate.

A vacuum generator (VacMotion, VM5-NA) converts compressed building air to a vacuum source with a maximum vacuum of 85 kPa. A solenoid valve (SMC pneumatics, VQ110, On/off time = 3.5 / 2 ms), commanded by a microcontroller, regulates the compressed air as a means of moderating vacuum intensity. The vacuum hose that applies suction to the cup is attached at both the suction cup vacuum connector and proximal to the load cell to reduce tube movement and subsequent F/T coupling.
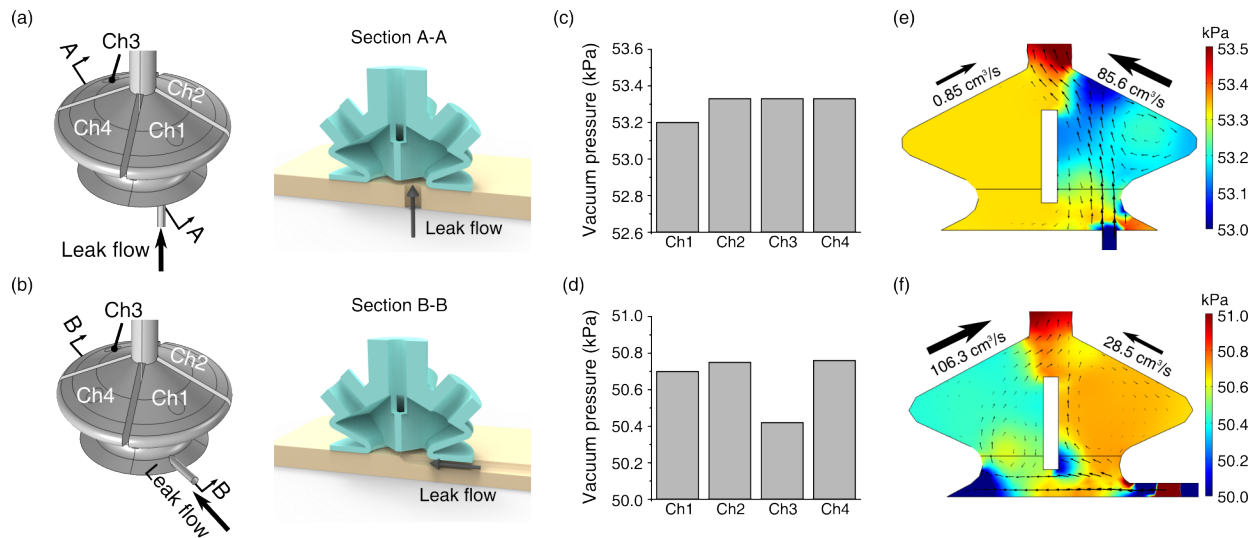
Figure 3.4: **Two cases of CFD simulation.** (a-b) Light yellow blocks are engaged objects and the cross-sectional view shows leak flow into channel number 1. (c-d) CFD result of the vacuum pressure measured at the sensor locations of each chamber. The bar graphs are from the maximum of the four vacuum pressures. (e-f) Cross-sectional view of the pressure distribution. The arrows inside represent the relative logarithmic scale of airflow velocity.

The experiments are conducted on a desktop computer running Ubuntu 20.04 with a 3.00-GHz Intel Core i5-7400 quad-core CPU and an Intel HD Graphics 630 GPU. The UR-10 controller is responsible for moving the robot to the target pose, while communication between the desktop computer and the UR-10 robot uses Real-Time Data Exchange (RTDE) over a standard TCP/IP connection. We used ROS (Noetic) to collect both pressure sensor and wrist force/torque (F/T) sensor data during experiments. An RBG-D camera (Intel, RealSense D435) is additionally mounted to the robot arm wrist such that it does not apply any wrenches on the F/T sensor. It takes photos (640x480 RGB resolution, 0.1 mm depth resolution), which are used in the bin-picking experiments.

3.4 Autonomous Haptic Search

The control goal is to enable the robot arm to make small end-effector pose adjustments in the direction that will eventually seal the suction cup, in other words bring the vacuum pressure of all channels closer to the maximum vacuum–85kPa for the fully sealed condition. We decompose autonomous haptic search motions into three direction unit vectors defined in the tool basis, shown in Figure 3.6: (1) *lateral positioning* or translation along $\hat{v}$ in the $\hat{x}$-$\hat{y}$ plane, (2) *rotational alignment* or rotation about $\hat{\omega}$ in the $\hat{x}$-$\hat{y}$ plane, and (3) *axial movement* or movement along $\hat{z}$. The lateral positioning assumes partial contact of the suction cup
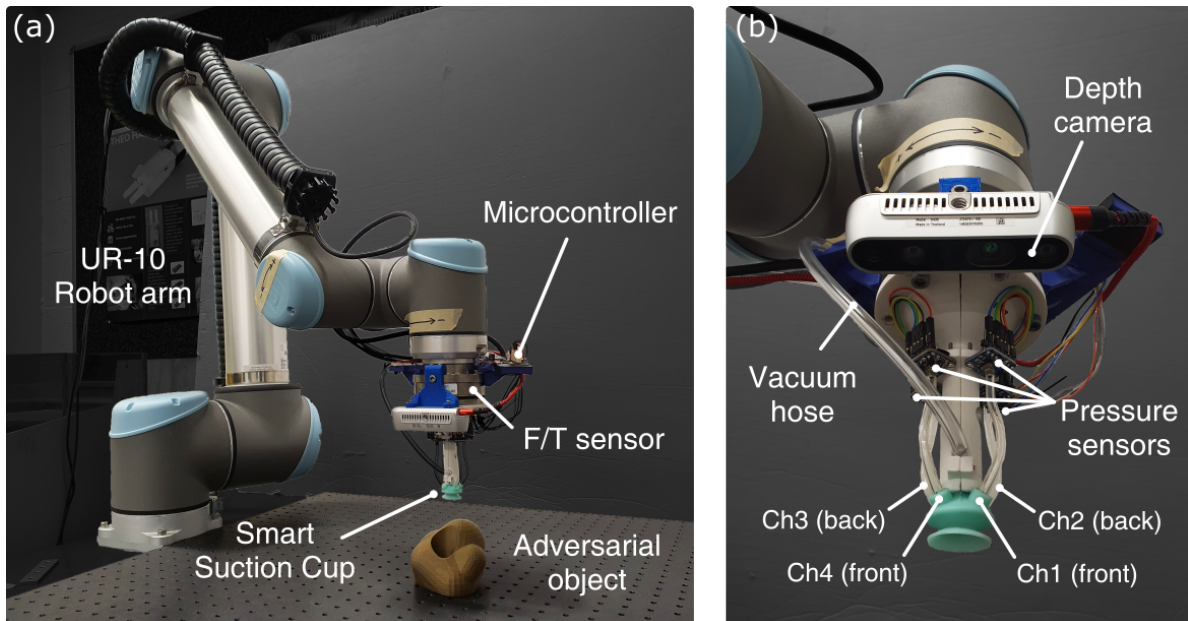
Figure 3.5: **System integration of the Smart Suction Cup.** (a) the smart suction cup system integrated on UR-10 robotic arm with a 6 DOF F/T sensor and a microcontroller. (b) Close up of end-effector, including the depth camera.

with an object or the presence of small holes underneath the cup. The rotational alignment assumes a misalignment between the suction cup and the surface normal of the object contact point. In both situations, we assume there is significant misalignment or the existence of bottom holes, resulting in vertical leak flows as depicted in Fig. 3.4(a). The axial movement ensures a consistent normal force, or $\hat{z}$-force, that is necessary to engage the suction with an object and maintain contact.

Both lateral positioning and rotational alignment search for a better grasping pose using smart suction cup pressure signals. To do so, pressures are first calculated for each cardinal direction by taking the average of the two chambers that correspond to that direction:[1]

$$P_E = (P_1 + P_2)/2 \tag{3.2a}$$
$$P_N = (P_2 + P_3)/2 \tag{3.2b}$$
$$P_W = (P_3 + P_4)/2 \tag{3.2c}$$
$$P_S = (P_4 + P_1)/2. \tag{3.2d}$$

Pressure differentials across cardinal directions are then calculated as:

$$\Delta P_{WE} = P_W - P_E \tag{3.3a}$$
$$\Delta P_{NS} = P_N - P_S. \tag{3.3b}$$

Using these values, the vectors $\hat{v}$ and $\hat{\omega}$ are calculated at each time step, in real time at a control rate of 125Hz.

Pressure Signal to Lateral Positioning

The lateral direction vector, $\hat{v}$, is defined to move the suction cup towards the channels with less leakage flow, i.e., higher vacuum pressure, as follows:

$$\vec{v} = -\Delta P_{NS}\hat{x}_{tool} + \Delta P_{WE}\hat{y}_{tool} \tag{3.4a}$$
$$\hat{v} = \vec{v}/||\vec{v}||. \tag{3.4b}$$

Then the lateral repositioning increments, ΔL_x and ΔL_y, are defined as follows:

$$\Delta L_x(\hat{v}, \Delta L) = \Delta L \hat{v} \cdot \hat{x}_{tool} \tag{3.5a}$$
$$\Delta L_y(\hat{v}, \Delta L) = \Delta L \hat{v} \cdot \hat{y}_{tool} \tag{3.5b}$$

where $\Delta L = 0.5$ mm, is the overall lateral positioning step size per control loop.

---

[1]This first step aligns the cardinal points with the wall interfaces of the cup. Alternatively, one can directly assign chambers to cardinal directions, e.g., $P_E = P_1$; this would result in a tool basis rotation of $45°$ about the $\hat{z}$ direction compared to our implementation.
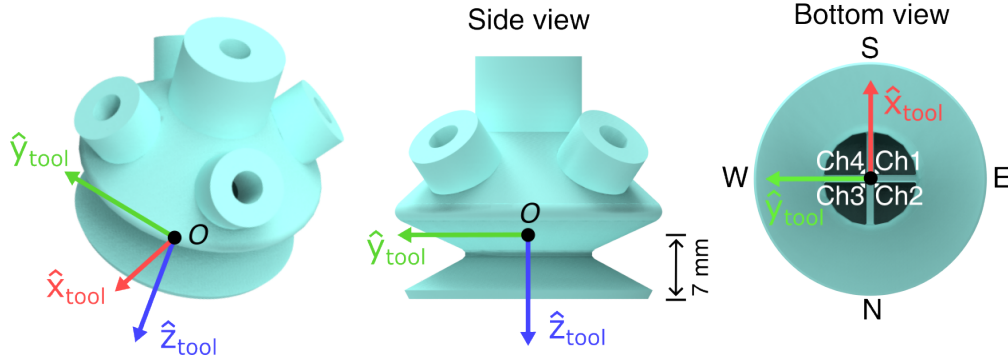
Figure 3.6: **Tool reference frame.** The reference frame associated with the tool end is shown, including the origin point (O) located relative to the unloaded cup lip. The cardinal directions of the cup are oriented along the walls of the inner chamber, shown in the bottom view.

Pressure Signal to Rotational Alignment

The rotational direction vector (axis of rotation), $\hat{\omega}$, is defined to close the gap between the object and channels with high leakage flow, i.e., low vacuum pressure, as follows:

$$\vec{\omega} = -\Delta P_{WE}\hat{x}_{tool} - \Delta P_{NS}\hat{y}_{tool} \tag{3.6a}$$

$$\hat{\omega} = \vec{\omega}/||\vec{\omega}|| = [\omega_1, \omega_2, 0]^T. \tag{3.6b}$$

Given an overall rotational alignment step size of $\Delta\theta = 0.5°$, the rotation matrix R is calculated as follows:

$$R(\hat{\omega}, \Delta\theta) = e^{\Delta\theta S(\hat{\omega})} \in SO(3), \tag{3.7}$$

where S is the skew-symmetric operator,

$$S(\hat{\omega}) = \begin{bmatrix} 0 & 0 & \omega_2 \\ 0 & 0 & -\omega_1 \\ -\omega_2 & \omega_1 & 0 \end{bmatrix} \tag{3.8}$$

Rotations are applied about the axis of rotation, along $\hat{\omega}$, which is always in the $\hat{x}$-$\hat{y}$ plane and always intersects point O.

Force Signal to Axial Motion

The axial step size ΔL_z, is calculated as follows,

$$\Delta L_z = \left\{ \begin{array}{ll} -\Delta z, & \text{if } F_z \leq F_{z,min} = 1.5N \\ 0, & \text{if } F_{z,min} < F_z < F_{z,max} \\ \Delta z, & \text{if } F_z \geq F_{z,max} = 2.0N \end{array} \right\} \tag{3.9}$$

where $\Delta z = 0.1$ mm is the axial step size per control loop.

Composition of Motion Primitives

To test different combinations of lateral and rotational motion in experiments, step sizes in the lateral and rotational directions are scaled as:

$$\Delta\theta_\alpha = \Delta\theta\alpha \tag{3.10a}$$
$$\Delta L_\alpha = \Delta L(1 - \alpha) \tag{3.10b}$$

where $\Delta\theta_\alpha$ and ΔL_α are new step sizes weighed by α, which in turn change ΔL_x, ΔL_y, and R, producing an overall transformation matrix, T:

$$T = \left[\begin{array}{ccc|c} & & & \Delta L_x(\hat{v}, \Delta L_\alpha) \\ & R(\hat{\omega}, \Delta\theta_\alpha) & & \Delta L_y(\hat{v}, \Delta L_\alpha) \\ & & & \Delta L_z \\ \hline 0 & 0 & 0 & 1 \end{array} \right] \in SE(3) \tag{3.11}$$

If $\alpha = 0$, then $\Delta\theta_\alpha = 0$ and $\Delta L_\alpha = 1$, which results in pure lateral positioning. If $\alpha = 1$, then $\Delta\theta_\alpha = 1$ and $\Delta L_\alpha = 0$, which results in pure rotational alignment. For any α, axial force control remains unchanged to ensure contact with a surface.

3.5   Experimental Methods

Sensing Characterization for Haptic Search

To characterize the Smart Suction Cup sensing performance relevant for (1) lateral positioning and (2) rotational alignment, we perform two characterization experiments, one for each. We swept lateral and rotational offsets from known reference points and analyzed the resulting pressure signals. From these pressure signals in each experiment, we compute measured $\hat{v} = \hat{v}_{meas}$ and $\hat{\omega} = \hat{\omega}_{meas}$, respectively. Based on the physical experimental setups, we know the ground truth $\hat{v}_{true}$ and $\hat{\omega}_{true}$ that would move the suction cup towards a successful suction grasp with the shortest displacement. As shown in Fig. 3.7a-b, we report direction error as the unsigned angle between the measured and true direction vectors:

$$e_v = \cos^{-1}(\hat{v}_{true} \cdot \hat{v}_{meas}) \tag{3.12a}$$
$$e_\omega = \cos^{-1}(\hat{\omega}_{true} \cdot \hat{\omega}_{meas}) \tag{3.12b}$$

for lateral positioning and rotational alignment, respectively, where e_v, $e_\omega \in [0°, 180°]$.

Lateral Positioning characterization procedure

In the lateral haptic characterization experiments, we positioned and oriented the suction cup relative to the edge of a flat plate, as shown in Fig. 3.7c-d. We define the lateral offset δ
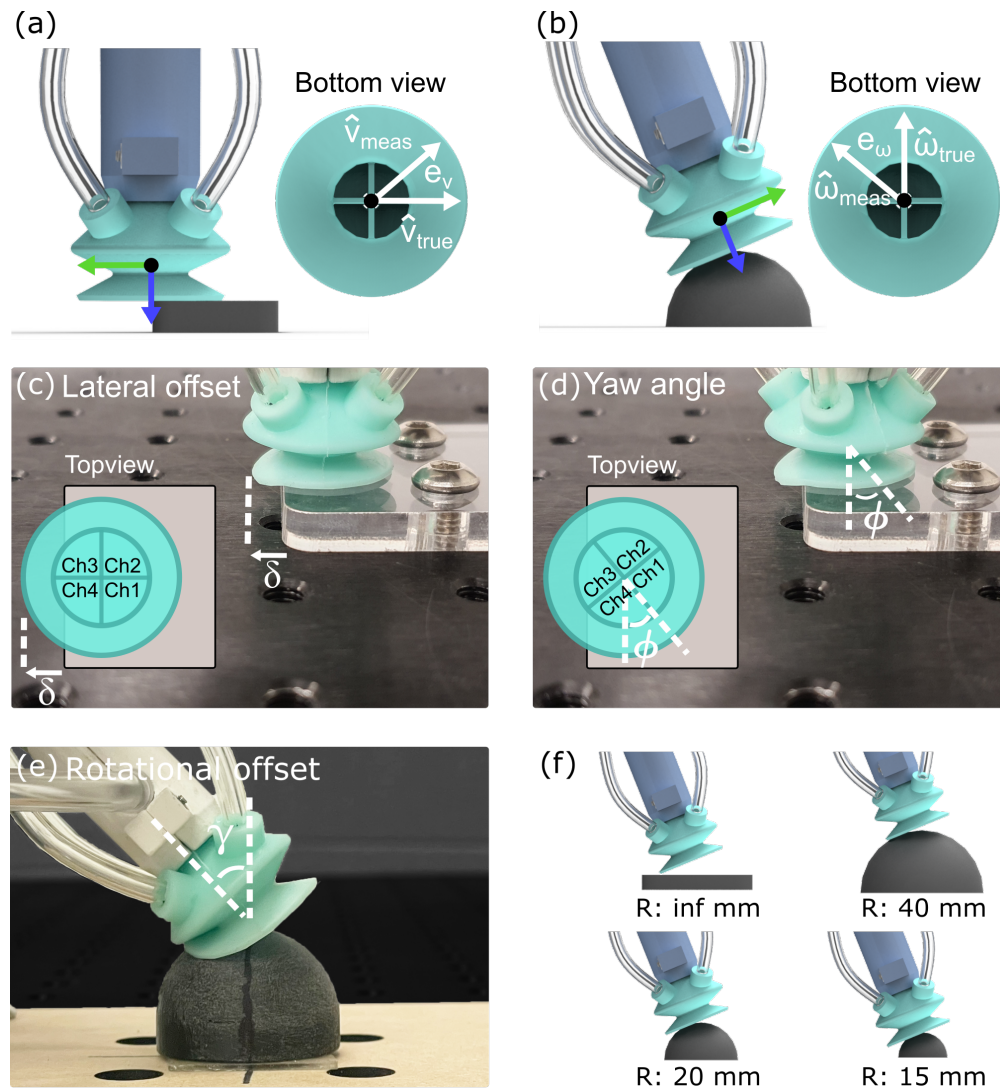
Figure 3.7: **Experimental setup.** Schematic image of direction error for (a) lateral positioning and (b) rotational alignment. (c) Experimental image of the suction cup with lateral offset, defined as the exposed lip length δ, and (d) yaw angle ϕ about the symmetric axis of the cup. (e) Experimental image of the suction cup with a rotational offset angle γ on a dome. (f) Four different radius domes for characterization of rotational alignment.

as the exposed lip length, and the orientation is parameterized by the yaw angle $\phi \in [0°, 360°]$ to test for asymmetry in the pressure sensor response. A yaw angle of $\phi = 0°$ corresponds to $\hat{v}_{true} = -\hat{y}_{tool}$. To maintain a constant vertical distance between the flat plate and suction cup across all trials, we apply a normal force of 1.5 N at a lateral offset of 0 mm and fix this height of the suction cup. We sweep the lateral offset from 0 to 23 mm with a 1 mm increment, noting that an offset of 11.5 mm is when the point O is vertically aligned with the edge of the plate, and sweep the yaw angle from 0° to 360° with a 5° increment. In each test pose, we average the sensor data over a measurement period of 2 seconds.

Rotational Alignment characterization procedure

In rotational haptic characterization, the suction cup was placed on and oriented relative to a sphere, as in Fig. 3.7e, such that the point O is vertically aligned with the highest point of the dome. We define the rotational offset γ as the angle between the true surface normal at this highest point (vertically upward) and $-\hat{z}_{tool}$. Domes with different diameters (15 mm, 20 mm, 40 mm, and flat plate) are selected, as in Fig. 3.7f, with the 15mm radius dome representing the smallest sphere that the suction cup can grasp in this study. In this experimental setup, $\hat{\omega}_{true} = \hat{x}_{tool}$. To initialize an experiment, we use force control to reach a target 1.5±0.1 N normal load[2], with $\gamma = 0$. We record the position of O in space at this moment, and then pivot about it while regulating the force along $\hat{z}_{tool}$. We sweep γ from 45° to 0° with 1° steps. At each offset, we average pressure measurements for 2 seconds of steady state readings.

Bin-picking

We set up a bin-picking task similar to that of [98] to evaluate the functional performance of the proposed haptic search algorithms. The robot system was programmed to pick objects up from a bin and transport them to a designated container, as shown in Fig. 3.8. For a given trial, the robot was first set with a particular controller. The system was then presented with 19 adversarial objects in a bin. Five of the objects were 3D-printed objects taken directly from the list of Adversarial objects from [81]. Eight of them were taken directly from the Level 3 object set in [98], which includes both 3D-printed and commercial objects. The rest of the objects were picked based on difficulty for a vision-based planner, specifically adversarial objects with imperceptible features like transparency, reflectivity, and small surface features.

Before the start of each trial, the operator placed the complete set of objects into the bin by first shaking them loosely in the container, inverting that container to drop them into the bin, and manually adjusting objects only to ensure that they were below the rim of the bin. The robot then continuously attempted to perform the pick-and-place task until an end-trial condition was met, and the number of successfully grasped objects was recorded.

---

[2]This type of force control to an exact value often leads to system vibrations. For the parameters used in our controller, with the tolerance of ±0.1 N and control rate of 125 Hz, we did not observe substantial vibrations.
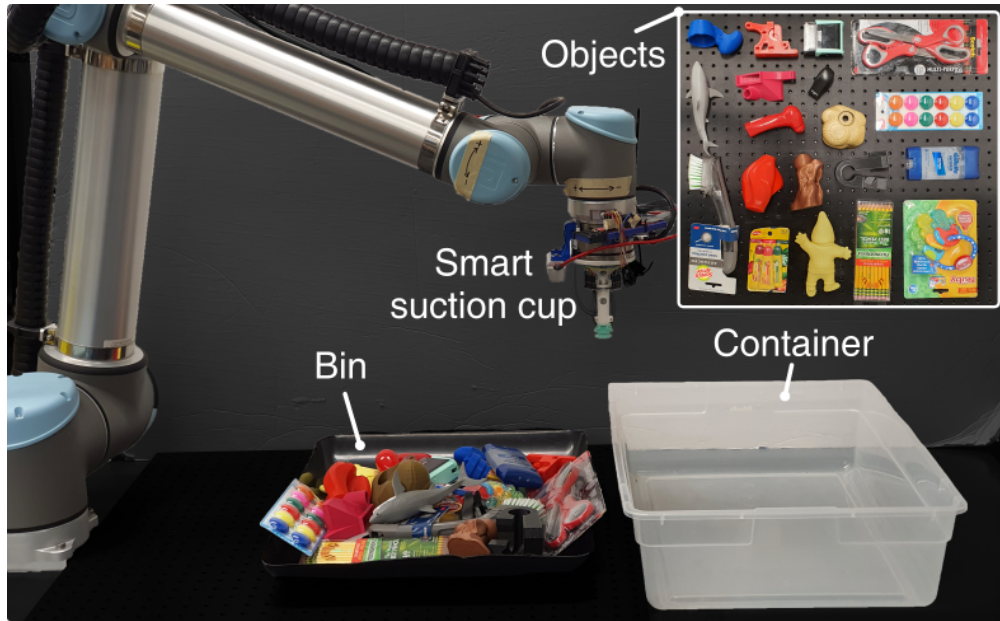
Figure 3.8: **Tabletop setup for bin picking experiments.** Inset: a dataset of 19 adversarial objects, showing eight 3D printed objects, six real objects with packaging, and five real objects without a package.
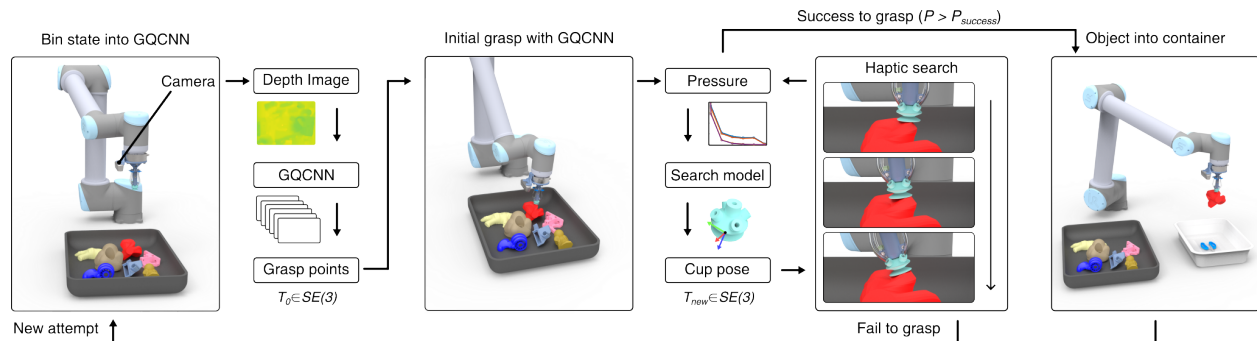
Figure 3.9: **Flow chart of robotic behavior during bin picking experiments.**[3]

In each trial, 57 attempts (three times the number of objects) were performed, and the trial stopped when 10 consecutive grasp attempts failed or no feasible grasping points remained available. We conducted five bin-picking trials for each tested control method.

   The process for each trial is shown in Fig. 3.9. On each grasp attempt within a given trial, a point cloud of the bin state with objects is inputted into the Grasp Quality Convolutional Neural Networks (GQCNN) [99] to generate 30 grasp point candidates with a grasp quality

---

[3]Visual renderings are used for illustrative purposes only. All characterization and bin-picking experiments were done with physical hardware, and not in simulation.

value ranging from 0 to 1 and corresponding suction cup pose. Among the candidates, the pose with the highest quality value and no previous failures is attempted. We implement a simple memory system to avoid repeated failures at the same grasp point. When a grasp is unsuccessful, the grasp point is stored and any points within 3 cm of previous failure points are considered non-feasible. The system stores up to three previous failures and is reset when the suction cup successfully grasps an object. Note that we have not re-trained this algorithm for our particular robot system or object set. The robot approaches the selected grasp point with a 15 mm offset in the estimated surface normal direction. Then, it approaches the surface along the estimated normal until normal force reaches 1.5 N. The suction cup then initiates vacuum suction and checks the vacuum pressure of all channels to determine whether it has successfully grasped an object. We define a grasp success if the mean vacuum pressure is greater than $P_{success} =15$ kPa, equivalent to holding $\sim$350 g with our suction cup. This estimate assumes the seal ring diameter is at the midpoint of the suction cup lip, or 17 mm across. The heaviest object lifted in experiments weighs less than 200 g, providing a safety margin of at least 150 g.

If a successful grasp is not detected after the initial grasp attempt with GQCNN, then the robot starts its specified search strategy to adjust the cup pose. During this search phase, a grasp is considered a failure if the suction cup moves away from the initial grasp point by more than 3 cm, rotates by more than 45° from the initial pose, or if the search time exceeds 15 seconds.[4] If the robot fails to grasp an object, it returns to the initial position and starts a new attempt. However, if at any point during the search procedure a successful grasp is detected, the robot then attempts to lift and move the object. Grasp failure is recorded if the object is dropped prior to the intentional release of the object into the container.

We evaluate eight total experiments: six with different haptic searching methods and two experimental controls. We implement five haptic search strategies by modifying the value of α from 0 to 1 in increments of 0.25. Specifically, we denote the values of α_1, α_2, α_3, α_4, and α_5 as an α of 0, 0.25, 0.5, 0.75, and 1, respectively. Also, we include a haptic search strategy which alternates a weight value between α_1 and α_5 every 0.5 s, denoted as $\alpha_{1\&5}$ in order to test the decoupling of motion between lateral positioning and rotational alignment. The first control condition is the application of GQCNN without any additional search method applied. As another experimental control case, we conduct a random search with Brownian motion (BM), or Weiner process, in the lateral direction; the lateral scalar step sizes in Eq. (3.11) , ΔL_x and ΔL_y, are chosen to make the standard deviation of the distance to be 3 cm from the initial grasp point after 15s of searching time.

---

[4]This maximum search time of 15 seconds was selected after preliminary experiments yielded diminishing grasp success after this time frame. In applications where speed is important, it would be impractical to search for an un-ending amount of time without a successful grasp.
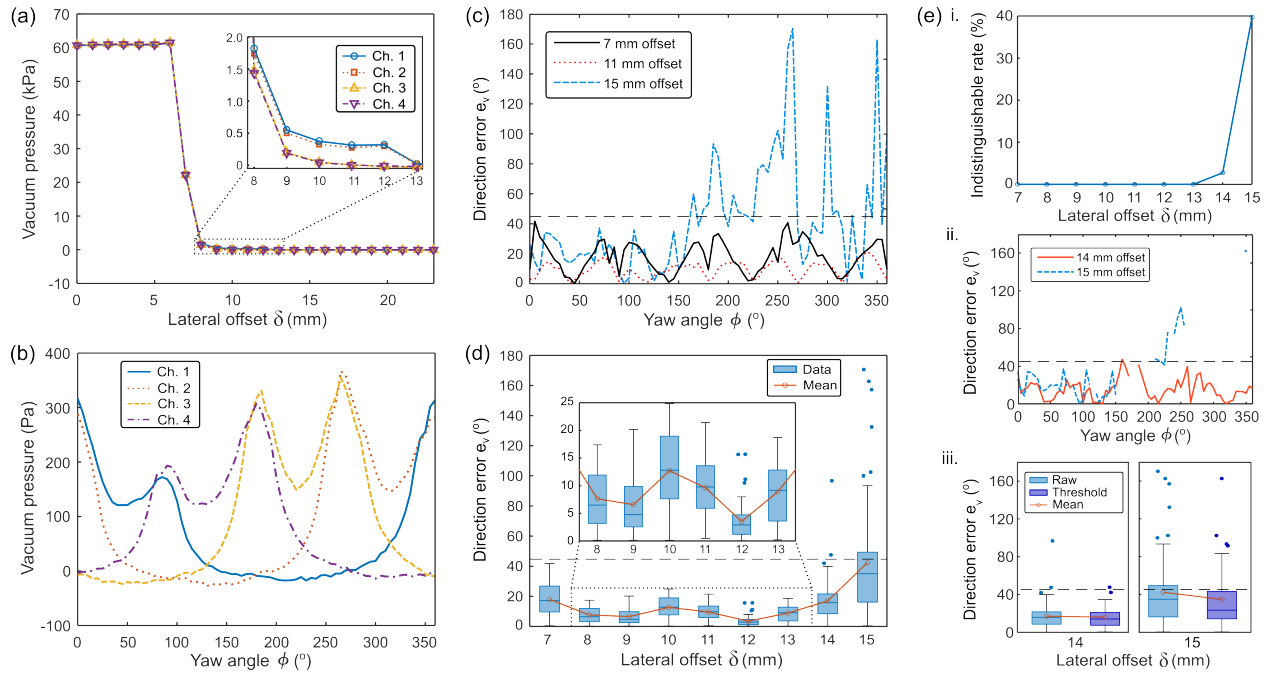
Figure 3.10: **Lateral characterization.** The pressure sensor readings for a sweep of lateral offset, δ, and yaw angle, ϕ, for the lateral positioning. (a) Vacuum pressure for a sweep of lateral offset from 0 to 23 mm at 0° yaw angle. (b) Vacuum pressure reading for a sweep of yaw angle from 0° to 360° at the center of the suction cup by averaging pressure reading at 11 and 12 mm lateral offset. (c) The direction error of various lateral offset. (d) Direction error data and mean. (e) Results from thresholding pressure readings by 10 Pa. i. The indistinguishable rate for a sweep of lateral offset. ii. The direction error at 14 mm and 15 mm lateral offset without indistinguishable data by thresholding pressure readings. iii. Direction error data and mean before and after thresholding pressure readings at 14 mm and 15 mm lateral offset. Dashed lines in the figure represent 45°.

3.6 Results

Lateral Positioning sensor characterization

The characterization results of lateral positioning are presented in Fig. 3.10. In Fig. 3.10a, the vacuum pressures from all channels are shown as lateral offset changes while yaw angle is held constant at $\phi = 0°$. All four channels remain over 60 kPa until the lateral offset reaches 6 mm; at these offsets, less than 7 mm, the suction cup seals completely with the plate and no haptic search is needed to grasp successfully. Note that the entire lip of this cup design does not necessarily need to be in full contact to generate a seal. Vacuum pressures decrease starting from a 7 mm lateral offset. The figure inset shows the region of offsets in which notable pressure differences exist between different chambers. Between 16 mm and 23 mm

lateral offset, pressure readings remain at 0 kPa across all chambers. It is therefore expected that directional signals will be most informative between 7 and 15 mm of offset.

To demonstrate how the pressure readings vary with the yaw angle, we vary ϕ from 0° to 360° with the edge of the plate located at the center of the suction cup (11.5 mm offset); we average the pressure readings at 11 mm and 12 mm lateral offset to estimate this cup alignment. As shown in Fig. 3.10b, the vacuum pressures in each chamber vary periodically with the change in yaw angle. At 0° yaw angle, chambers 1 and 2 overlap with the plate, showing higher vacuum pressure than the pressures from chambers 3 and 4. At every 90° of yaw angle, two chambers seal on the plate's surface, causing vacuum pressures to show peaks of two chambers. Given the chamber geometry of the cup, there will be higher overall vacuum pressure applied to the cup when more of the 4 chambers become sealed. This explains why we see two peaks per chamber, rather than just one, as the two adjacent chambers simultaneously break seal between local maxima. Variability between chambers is also seen, for example the maxima at $\phi = 90°$ is smaller than the others. Small variation could be caused by fabrication and assembly, as well as compliance in the suction cup, leading to asymmetric buckling deflections of the internal chamber dividers upon contact, as observed in prior work [77]. Regardless of chamber-to-chamber interaction and nonidealities, at each tested yaw orientation the 4 chambers provide a unique combination of readings to support the estimation of the ϕ state.

In order to understand the interpretation of these signals in our control algorithm, across both δ and ϕ, we visualize direction errors e_v with pressure sensor readings using Eq. (3.12a) in Fig. 3.10c-d. Direction errors from lateral offsets between 7 mm and 15 mm with 4 mm increments are shown in Fig. 3.10c. The 45° boundary indicates the directions that would enable faster haptic search for a better grasping point, by moving the cup towards the plate at a rate faster than along the edge of the plate. At 7 mm and 11 mm lateral offset, the direction errors show that all data is below the 45° boundary line. At a 15 mm lateral offset, some errors go above the boundary. The result shows that direction errors have a cyclic pattern every 45°, reflecting the internal wall structure of the suction cup with four chambers.

In Fig. 3.7d, we report the direction error for all trials between 7 and 15 mm offset. Each lateral offset has 73 data points, where we sweep yaw angles from 0° to 360° with a 5° increment. The result shows box plots with the means of the data. No data exceeds the 45° boundary from 7 mm to 13 mm lateral offset. However, within this range, error is greatest at 7 mm. It makes sense that direction error increases as the offset approaches 6 mm, as the suction cup becomes fully sealed and flow stops altogether. For the 7 mm case, as demonstrated in Fig. 3.4d-f, flow can become predominantly horizontal at the transition to the fully-sealed state, thereby decreasing the pressure difference between the exposed and covered chambers. At both 14 and 15 mm lateral offset, where pressure differences become small, several data points show error over 45°, yet the mean of the direction error remains below this threshold.

At large offsets, greater than 15 mm, the pressure approaches 0 Pa and e_v increases further, meaning that all four channels are open and not forming effective differential pressures.

We therefore apply a threshold condition of 10 Pa during controller implementation such that, when all chambers are below this level, the direction estimate is set to $\hat{0}$ (no motion). The rate at which this condition is met, which we call the indistinguishable rate, at different lateral offsets is shown in Fig. 3.10e i. The indistinguishable rates from thresholding are found to be 2.7% and 39.73% at 14 mm and 15 mm lateral offset, respectively, while no data are indistinguishable between 7 mm and 13 mm lateral offset. Fig. 3.10e ii shows the corresponding result of direction errors e_v at 14 mm and 15 mm lateral offset, where the indistinguishable data points are eliminated. Fig. 3.10e iii shows the change in e_v resulting from the threshold condition. Before thresholding, the mean of direction error at 14 mm lateral offset is 16.99°, which decreases to 15.70° after thresholding. At a 15 mm lateral offset, the mean direction error changes from 42.42° to 34.71°. In practice, motion will only occur when at least one channel measures a degree of flow restriction – if there is no measurable suction contact the cup will remain stationary.

Rotational Alignment sensor characterization

The characterization results of rotational alignment are presented in Fig. 3.11. Since the suction starts without a seal, we read the plot with decreasing rotational offset from left to right. The cup initially starts at $\gamma = 45°$ and all channels read close to 0 kPa. The critical rotational offset, where the vacuum seal is formed, is seen by a rapid increase in the vacuum pressure (Fig. 3.11a). This critical offset angle becomes smaller as the radius of the dome decreases, indicating that smaller radius domes require more precise alignment with the surface normal to successfully grasp. At rotational offsets smaller than the critical offset angle, the vacuum pressures are consistently near 60 kPa across all channels. The control condition for successful grasping, $P > P_{success}$, is shown as the horizontal dashed line. The region of interest for haptic search occurs when there is the presence of pressure differentials within the cup, detailed in the figure, comparing P_W and P_E. The difference is directly plotted as ΔP_{WE} in Fig. 3.11b after removing data points where $P > P_{success}$. For the 15 and 20 mm radius domes, signals rise as high as 1.5 and 1.2 kPa, respectively, over larger rotational offset ranges than the 40 mm dome or flat plate. The pressure differential for the flat plate in particular never even reaches a ΔP_{WE} of 20 Pa, because the compliant lip rapidly deforms and pulls itself into the surface before substantial differential flows can occur inside the cup due to chamber occlusion. We therefore expect tactile sensing to provide more useful prediction of $\hat{\omega}$ on higher curvature objects, where smaller domes can better occlude chambers before the critical angle is reached and more careful alignment with surface normal is required.

As shown in Fig. 3.11c, the test results indicate that the direction error (e_ω, Eqn. 3.12b) is lower for objects with smaller radii. Each subplot i-iv represents a trial on a different object and data for which $P > P_{success}$ is omitted. When we add a dashed boundary line of 45°, similar to in lateral search characterization, we see that errors consistently drop below 45° at rotational offsets of 30°, 31°, 23° for domes with radii of 15 mm, 20 mm, and 40 mm, respectively. On the other hand, the flat plate error does not fall below this threshold
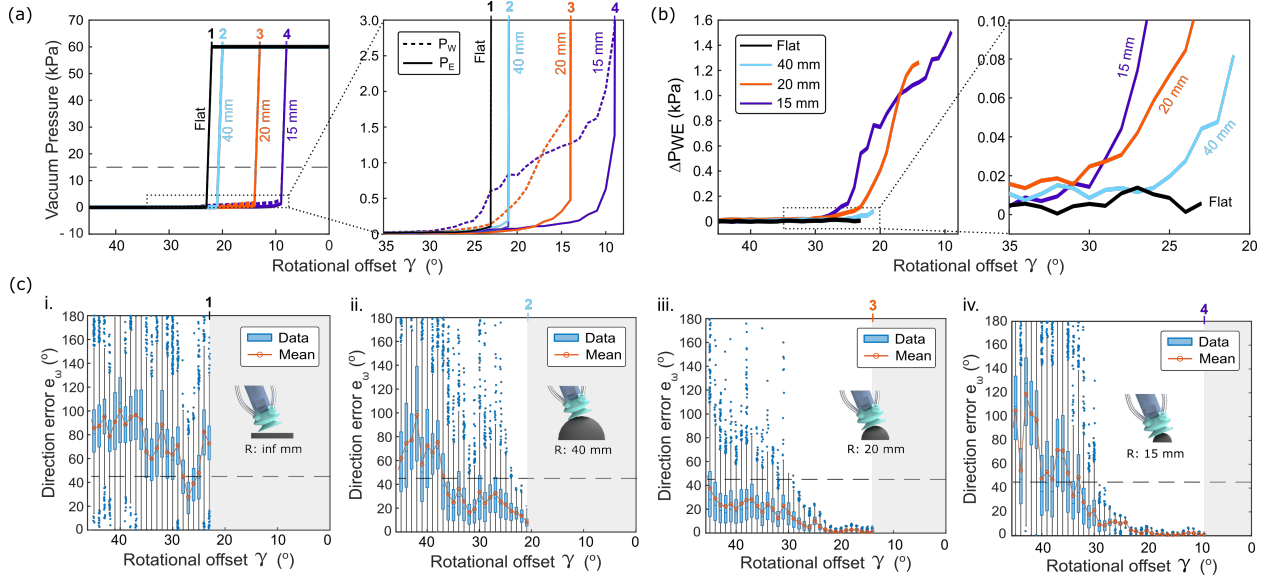
Figure 3.11: **Rotational characterization.** Vacuum pressure and pressure differential measurements for a sweep of rotational offsets γ, and direction error, e_ω, for four different objects - a flat plate and spheres with 40 mm, 20 mm, and 15 mm radii. (a) Vacuum pressures for $\gamma \in [45°, 0°]$. Pressure increases sharply at different critical offset angles as the vacuum seals on the surface, points numbered 1-4. Before sealing occurs, differences between P_W and P_E are visible, especially for the 20 mm and 15 mm objects. (b) Pressure differential between west and east chambers for each curved surface. Differential signals rise faster for high curvature objects. (c) i-iv. Direction error data and mean for the four objects. Included is the 45° direction error boundary line. The shaded regions indicate the rotational offsets at which the suction cup passively grasps the object, smaller than the critical offset angle. Direction error past 90° corresponds to motion perpendicular to the true desired direction.

consistently on the flat plate because ΔP_{WE} remains small up to the critical angle. The smaller radii objects (R=15 mm and 20 mm) show the most accurate predictions ($e_\omega < 10°$) close to the critical rotational offset. This result suggests that the proposed haptic search method can successfully grasp objects with small critical offset angles (e.g., 8° in R=15 mm object), even with high visual perception error of surface normal up to 30°.

Bin-picking

We evaluate the bin-picking test conditions defined in Section 3.5, with results shown in Fig. 3.12. The picks-per-attempts mean average from across five independent trials for each condition is reported in Fig. 3.12a; the six haptic search conditions are in shades of red while the the two experimental control cases are in shades of blue. All trials are reported for each
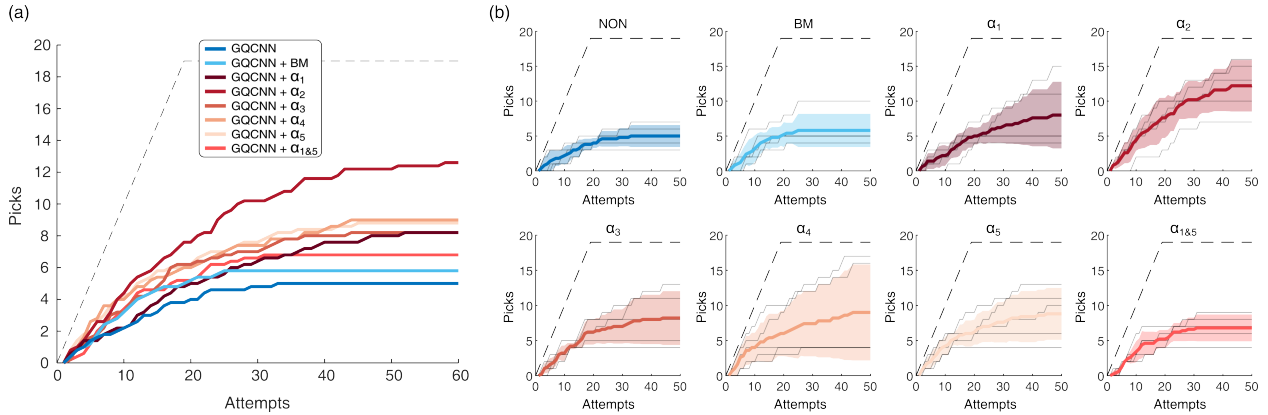
Figure 3.12: **Results of bin picking experiments.** (a) The average number of successful picks across all grasping methods. (b) The individual results for each grasping strategy, with solid colored lines indicating the average and colored areas representing the standard deviation. The grey lines within each grasping method indicate the results of individual trials. As a reference, a dashed black line is used to represent the optimal performance, which is defined as successfully picking every attempt in the bin until it is completely empty.

test condition experiment in Fig. 3.12b. The dashed lines on all plots indicate the ideal case where every grasp attempt is successful without any failures.

The control case "GQCNN" or "NON," which has no search phase, shows an average of 5 ± 1.58 successful picks. This means the robot system was able to successfully pick-and-place these objects from the bins without any haptic search assistance. The control case "GQCNN + BM," which includes random Brownian motions in lateral direction during the search phase, results in an average of 5.8 ± 2.39 successful picks. This shows that the introduction of non-haptically-driven motion after the initial grasp attempt can provide minor improvements. Comparing the two control cases with this ideal performance, we see the difficultly of the selected adversarial pick-and-place task. Of the two control cases, we propose that it is more appropriate to compare haptically-driven results with the "GQCNN + BM" control case because it represents baseline benefits from the presence of a search phase.

The proposed haptic search methods are labeled α_1 to α_5 and $\alpha_{1\&5}$. Results show that α_2 provides the highest number of successful picks per trial, with an average of 12.6 ± 4.16. Lateral positioning (α_1) and rotational alignment (α_5) show reduced results similar to one another, with 8.2 ± 5.17 and 8.8 ± 3.70 successful picks, respectively. α_3 results in an average of 8.2 ± 3.83 successful picks and α_4 provides successful picks (9 ± 6.86), but with the largest standard deviation. For the performance of the alternating haptic search method $\alpha_{1\&5}$, it shows the lowest successful picks of 6.8 ± 1.92 among all the haptic search methods evaluated. Overall, these results demonstrate the effectiveness but also the between-trial variability of the proposed haptic search methods. Out of these methods, α_2, which

predominantly performs lateral search but with some rotational alignment, best improves the success rate of bin picking by the robot system. However, between trial variability indicates that the potential benefits of haptic search is sensitive to initial bin state.

We can then compare the autonomous haptic search methods with the experimental control cases. In the region between 0 and 5 pick attempts, there is little difference between all eight methods. This indicates that success is driven by the GQCNN method, mostly because we attempt the grasping pose with the highest quality value first. The methods diverge in performance after 5 attempts, where the GQCNN and α_1 methods show lower performance than the other six methods. At 25 or more bin pick attempts, all six haptically-driven methods outperform the two experimental control methods. This indicates that autonomous haptic search methods are helpful to expand achievable grasp points, to now include those that GQCNN alone is unable to accurately predict.

Here, we quantify how much fine-tuning is executed through haptic search on average. Among the successful haptic search trials, across all six haptically-driven methods, the mean cartesian displacement from the initial pose was 4.8 mm with a maximum of 13.9 mm. Mean path length was 8.7 mm with a maximum of 32.7 mm. Mean angular displacement was 5.9° with a maximum of 25.2°. Mean angular distance traveled was 6.8° with a maximum of 39.1°.

3.7   Discussion

Sensor characteristics

Through varying the lateral displacement and yaw of the cup against a flat plate edge and varying orientation with domes of different sizes, we characterized the scale and types of pressure signals that the Smart Suction Cup produces. We also demonstrated how these raw signals are interpreted using our proposed haptic search procedure. However, plates and domes represent primitive shapes. The complexity of object geometries in real-world scenarios, with a combination of vertical and horizontal flows, will likely impact the haptic search effectiveness of the suction cup, making it challenging to identify suitable direction vectors. This may help us to understand why, at times, we observed certain unproductive haptic behaviors emerge during the bin-picking task.

We found in sensor characterization tests that thresholding reduced direction error, by eliminating cases where pressure differential measurements are too low to produce reliable estimates when sensor noise starts to dominate. At the same time, it is unlikely that perfect prediction accuracy is essential in effectively deploying Smart Suction Cup haptic search. Specifically, the prediction accuracy appears to improve as the cup gets closer to a successful grasp. During haptic search, if, as a result of noisy signals due to low pressures, the cup randomly reaches any state where a more accurate prediction can be better made, then the behavior will converge on a successful grasp over time. We posit that this will be especially true if, on average, predictions start from a place that are within 90° of the true direction
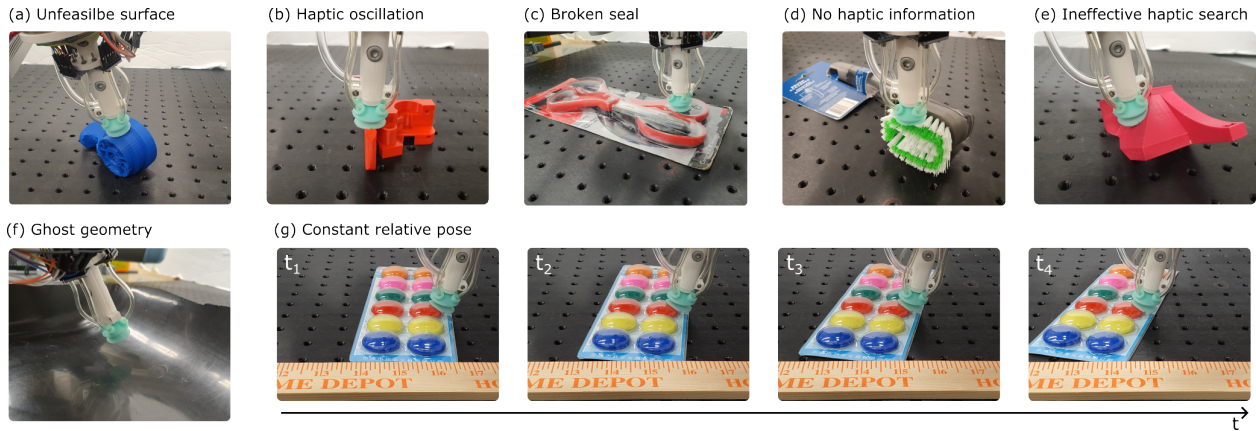
Figure 3.13: **Failure modes.** Representations of the failure modes for the Smart Suction Cup observed during the bin-picking experiments.

vector. In future work, conducting closed-loop control experiments, rather than stationary sensor characterization, would identify the highest possible offsets for which haptic search still yields a successful grasp, including on a wider variety of object shapes.

In the lateral search case and especially the rotational alignment case, we find that the compliant material and the bellows of the suction cup allows it to engage with objects even with postural errors to some extent. However, for objects with high curvature and critical features such as holes, the inherent tolerance of the suction cup may not be sufficient. In such cases, our proposed haptic search method is expected to enhance the operational tolerance even when the vision system fails to capture those features accurately.

Bin-picking observations

Bin-picking experiments suggest that a physical search phase after contact is made can improve grasp success, especially when employing autonomous haptic search methods that respond to measured contact conditions. The fact that all haptic search methods tested provided some increase in picking success rate as compared with experimental controls, including with random searching, shows how responding to contact pressures, even with a simple model-based controller, holds potential thus motivating ongoing investment in the Smart Suction Cup capability. We used a single suction cup prototype throughout all of these bin-picking-experiments, representing at least 1316 autonomous grasp attempts, without incurring damage to the cup or needing replacement. The Smart Suction Cup design, where the cup is fabricated in a single-step casting process and electronics are remote from the cup, thus appears to provides reliable and physically robust performance.

We saw the biggest performance increase with the α_2 haptic search method, whose motion is a mix of lateral positioning with a bit of rotational alignment. Though it matches our expectations that a coupled motion would yield better results than purely sliding (α_1) or

rotating (α_5), because most objects have both edges and curves, it is less obvious why α_2 outperforms α_3 and α_4. A possible theory is that the rotational alignment search counteracts the lateral search, so finding the optimal tuning between them is required. When the suction cup has partial contact, the lateral search attempts to reinforce contact on the contacted side by moving towards it, while the rotational alignment loosens the contact side and attempts to make balanced contact over all channels. Therefore, an appropriate balance between the two modes should be adjusted. We believe that α_2 provides the best balance among the five presets in general, but each geometry may require a different optimal balance between the two modes. We leave this local, object-specific controller optimization as a future work.

During the bin-picking trials with autonomous haptic search, we observed different common grasp failure modes. We classify them into seven categories, as shown in Fig. 3.13:

1. *Unfeasible surface:* Haptic search starts at an infeasible surface, where possible grasp poses are beyond the searching boundary.

2. *Haptic oscillation:* Haptic search oscillates in a region where haptic information makes the cup move back and forth without converging to a graspable point.

3. *Broken seal:* The contact wrench applied to the cup is too large to lift an object. This typically occurs when the suction cup tries to grasp a heavy object from the edges, also reported in [100].

4. *No haptic information:* The suction cup cannot get any distinguishable haptic data from a surface, such as the bristles of the brush (P<10 Pa).

5. *Ineffective haptic search:* A surface is feasible and haptically searchable, but the system uses an ineffective behavior. The example shows a case where the suction cup is using lateral positioning but would benefit more from rotational alignment.

6. *Ghost geometry:* Reflective and/or transparent materials yield artifacts, resulting in ghost geometries in a depth image. The example in the figure shows the suction cup is trying to grasp in the air because the light from the ceiling is reflected on the bin surface.

7. *Constant relative pose:* During haptic search, a loose object can be pushed such that the relative position between the cup and object remains unchanged despite robot motion. Given the new position of the object, the next attempt may consider the same grasp point as a valid candidate as its pose in the world frame changed.

Several of these error types occur because the vision-based grasp planner initializes the grasp at a point in which a suction grasp is locally impossible. The cases in Fig. 3.13 (a), (c), and (f) are not recoverable using contact condition condition sensing. To combat these, the camera and/or visual planner performance would need to be improved. However, for cases in Fig. 3.13 (b), (d), (e), and (g), new adaptive haptic search controllers designed to identify
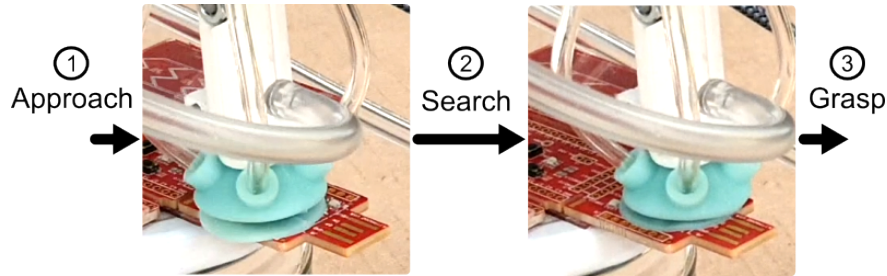
Figure 3.14: **Lateral haptic search on PCB.** An example of lateral haptic search, α_1, on a stationary PCB adhered to a surface. ① "GQCNN" guides to the pose where there are several via holes. ② The suction cup adjusts its lateral pose given its pressure readings. ③ The haptic search succeeds in grasping the PCB within 2 seconds.

and overcome such failure cases could further improve grasping in future work. For instance, the failure mode (g) may be effectively addressed through a jumping haptic search approach. In this approach, the suction cup retracts from an object and then re-approaches with an adjusted pose. This prevents the suction cup from exerting continuous pressure on an object while making pose adjustments. We recommend also coupling vision with the haptic search process. For example, camera information could be used to select appropriate haptic search methods in response to case (e). Or vision could identify object movement in (g) to adapt behavior on the fly; for example, in [77], we propose that one could dynamically reduce the suction pressure of the vacuum in order to achieve more gentle sliding over objects.

In the present work, we made the deliberate choice not to re-train the GQCNN algorithm for our particular robot system, resulting in overall low planner performance. In our case, we use a different camera, robot arm, object set, room/lighting, gripper, and bin from the ones used in training. The purpose of this choice is to generate a scenario that emulates a quick-adopt case for such technology, since generalizability is an ongoing challenge for such planning algorithms [101]. The present work therefore shows that the use of a Smart Suction Cup can be one tool in ameliorating errors that arise specifically in previously unseen systems. Future work will investigate how planner optimization and hardware selection (e.g., higher spatial resolution camera) affects the role of autonomous haptic search.

Printed Circuit Board demonstration

In the bin-picking experiment, the tested objects all had at least one smooth graspable surface for the suction cup to grip. However, some real-world objects have bumpy surfaces without any obvious continuously-smooth regions. For example, a Printed Circuit Board (PCB) with Integrated Circuits (IC) soldered on it and via holes might prevent the use of a suction cup, if the cup would fail to grasp at most surface locations. However, haptic search behaviors can still enable the grasping of such surfaces, adapting around local features to

achieve a seal. To demonstrate this behavior, we fix a printed PCB to the table and allow the cup to search for a grasp point using only lateral positioning, or α_1. Fig. 3.14 shows how the cup is able to find a successful grasp point over one of the IC's. Future work will measure to what extent the cup can respond productively on surfaces with different types of porosity and rugosity profiles for real-world applications.

In Fig. 3.10, the directional errors in lateral search on a flat, smooth plate commonly reach almost $20°$ for the best case lateral offsets between 8 and 13 mm. These errors may appear unsatisfying and at times result in longer searching paths than desired. This directional error provides one reasonable explanation for the edge-following behavior that emerges at Grasp point 3 in Supplementary Video. However, the PCB demonstrations show how this error does not necessarily result in overall failure during smart suction haptic search; the controller continues to adjust its directional estimate every 0.5 mm as it moves, ultimately leading to a successful grasp. Regardless, future work should investigate how performance – such as time and distance to successful grasp – may be optimized through cup and algorithm design.

3.8   Conclusion

The four-chamber cup design of the Smart Suction Cup, with remote pressure transducers, provides a reliable solution for generating differential airflows and protecting sensitive electronics from physical damage. In this work, our proposed autonomous haptic search method – a model-based approach for estimating lateral positioning and rotational alignment – enables the suction cup to adjust to a successful pose for suction grasping, effectively increasing tolerance to positioning or misalignment error induced by limitations of a vision-based grasp planner. Object properties such as surface roughness, holes, and ridges present adversarial conditions for vision-based grasp planners, and the Smart Suction Cup holds the potential to improve gripping of adversarial objects in various scenarios that already deploy vacuum grippers, such as in recycling facilities, warehouses, manufacturing, and logistics robots.

Future work

This study presented a single implementation of the Smart Suction Cup and one particular model-based approach to generating haptic searching behaviors in response to pressure readings. In future work, we seek to explore new soft cup designs to both improve gripping performance while studying how parameters, like the number of chambers, affect sensing. Next steps include optimization and learning-based approaches for sensor characterization and mixing lateral positioning and rotational alignment. These adaptive methods may be informed by visual and haptic information, for example. Finally, the ultimate goals of this line of work is to explore the adoptability and lifetime of such technology in real-world application.

Chapter 4

Adaptive Contour Following with a Suction Cup

The Smart Suction Cup is a tactile sensing and gripping system designed to enhance pick-and-place operations in industrial settings. While previous research has primarily focused on utilizing this technology for haptic search in cases of initial grasp failure, this study introduces a novel application: following contours. This function is already established as an important function for object recognition and grasp planning – substantiated by numerous works using other tactile sensors. Here, we explore contour following for a flow-based tactile sensor because it is not susceptible to visual occlusions nor tactile sensor wear. Experimental validation demonstrates the Smart Suction Cup's ability to track edges at different speeds and navigate various planar contours, showcasing rapid and robust tracking of edges. Notably, the Smart Suction Cup can reliably operate at a speed of 3 cm/s. This is one step towards the adoption of the Smart Suction Cup for real-world applications.

4.1 Introduction

Suction cups play a crucial role in industry for pick-and-place tasks. Their ability to astrictively grip and manipulate objects of various shapes and sizes makes them valuable tools for manufacturing and logistics operations today. However, traditional suction cups typically lack tactile sensing, limiting their adaptability and effectiveness in semi-structured and cluttered environments, such as e-commerce warehouses. Thus, prior efforts equip suction cups with sensing abilities.

Doi et al. (2020) proposed a 3-electrode capacitive sensor, which could localize contact [88]. Shahabi et al. (2023) embedded four microfluidic, carbon grease channels into a single suction cup, and demonstrated surface slope estimation [87]. Aoyagi et al. (2020) dip-coated a 2x2 array of suction cups with a thin-film polymer [85] and demonstrated real-time edge detection to trigger a regrasp. However, contour following with a sensorized suction cup has not yet been demonstrated. We seek to address this gap with the Smart Suction Cup.
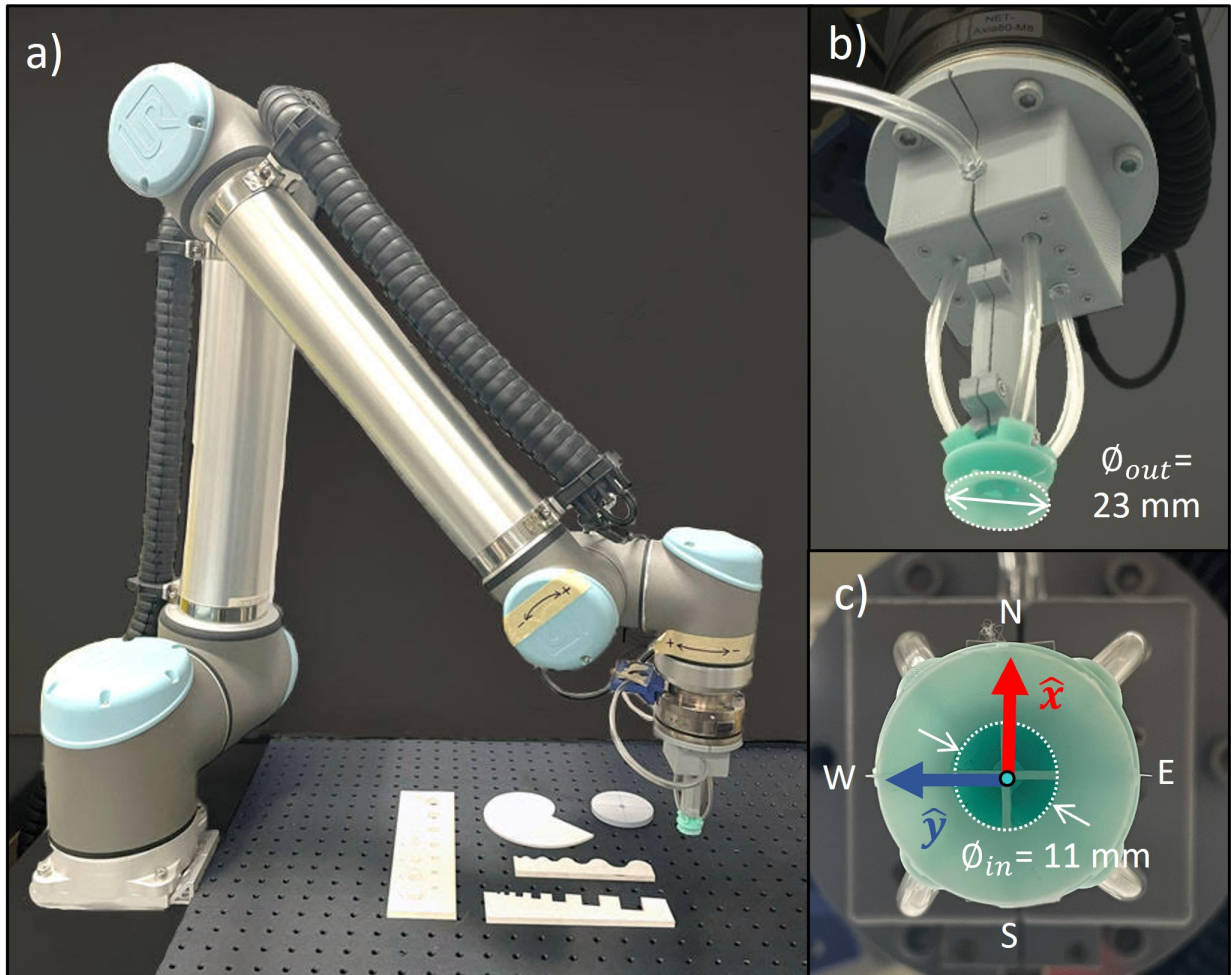
Figure 4.1: **The Smart Suction Cup robotic system.** a) suction cup mounted on a robot arm, b) close-up of suction cup hardware, and c) bottom view of the suction cup showing the tool frame.

The Smart Suction Cup was first introduced by Huh et al. (2021) [102]. We then introduced a haptic search method for sliding and rotating control strategies for grasping adversarial objects [103]. Implementing this method, which identifies viable grasping points when the initial grasp point fails, resulted in a 2.5x improvement in grasping during cluttered bin-picking trials. Our latest hardware is summarized in [103] and tested on PCB's for industrial recycling applications. Tactile sensors often employ localized force or geometry transducers near the contact point. One relative advantage of the Smart Suction Cup hardware is that its sensitive electronics are remote from the point of contact, which reduces physical damage to the transducers and degradation of the tactile signals. Though we previously demonstrate adaptive grasping capabilities with this technology, purposeful contour following has yet to be realized.

Contour following is employed by people when interacting with the physical world as

an integral part of haptic exploration. Edges are particularly salient features for humans [104], and guide the recognition of object shapes [105]. Lepora et al. (2017) demonstrate contour following with the TacTip using model-based [106] and model-free [107] approaches, the latter being more robust to complex, soft, and irregular objects. They also demonstrate this ability with DIGIT [108] and DigiTac [109]. With their 12-taxel, capacitive sensor, Martinez et al. (2013) demonstrate object shape classification with contour following [110]. These works show that robots can leverage contour following using tactile information alone in ways that are useful for automated dexterous manipulation.

Overview

To the best of the author's knowledge, we are presenting the first case of contour following using a suction cup gripper. Section 4.2 provides a description of the contour-following controller design. In Section 4.3, we summarize the hardware (Fig. 4.1) and describe controller bench-marking methods. In practice, speed and versatility of a tactile sensing system are both desirable, though these performance metrics can be at odds. The current study evaluates the Smart Suction Cup's ability to track an edge at different speeds as well as the ability to navigate different planar contours. Section 4.4 presents the experimental results. We find that at low speeds many controller designs achieve contour following on a disk, but at higher speeds success rate is more sensitive to controller parameters. We also observe successful contour following on compound geometries and filleted edges. In Section 4.5, we discuss the effects of parameters on success envelopes, reliability and speed, and observed failure modes. We conclude in Section 4.6 that rapid and robust contour following with the Smart Suction Cup is possible.

4.2 Controller Design

To achieve contour following, the controller first determines the direction in which to move. For each loop iteration, the pressure differential across the chambers, ΔP, is computed for two orthogonal directions of the cup's gripping surface, $\hat{\boldsymbol{x}}$ and $\hat{\boldsymbol{y}}$, as:

$$\Delta P_y = P_W - P_E \tag{4.1a}$$
$$\Delta P_x = P_N - P_S \tag{4.1b}$$

where P is the vacuum pressure relative to ambient pressure, and the subscripts represent cardinal direction or chamber number, e.g., P_1 is the vacuum pressure from chamber 1, and $P_S = \frac{P_1 + P_4}{2}$, while $P_N = \frac{P_2 + P_3}{2}$. With these pressure differentials, we can compute the direction vector as:

$$\mathbf{v} = \text{-}(\Delta P_x \hat{\boldsymbol{x}} + \Delta P_y \hat{\boldsymbol{y}}) \tag{4.2}$$
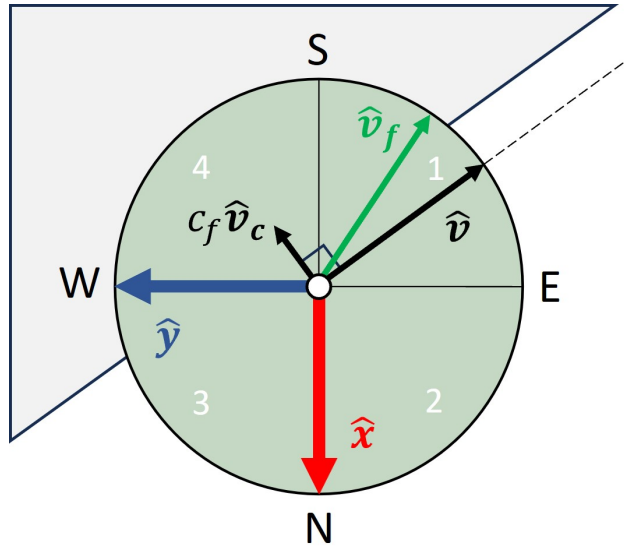
Figure 4.2: **Top view diagram of the Smart Suction Cup on a straight edge.**

where $\hat{x}$ and $\hat{y}$ are fixed in the tool frame. In this work, we use only the direction or unit vector $\hat{v}$. We also define a correction unit vector, $\hat{v}_c$, which is orthogonal to $\hat{v}$. The final vector, $\mathbf{v}_f$, is a linear combination of $\hat{v}$ and $\hat{v}_c$:

$$\mathbf{v}_f = \hat{v} + c_f \hat{v}_c \tag{4.3}$$

where c_f is the correction factor. Similarly, we normalize to compute unit vector, $\hat{v}_f$. Fig. 4.2 graphically shows the relationship between these vectors for a particular instance, assuming that $\hat{v}$ has no error. The mean pressure across the four chambers is computed as,

$$\bar{P} = (P_N + P_S + P_W + P_E)/4. \tag{4.4}$$

We allow the correction factor magnitude, $|c_f|$, to vary linearly with the log of the mean pressure, $\log_{10}(\bar{P})$. The idea is that $\bar{P}$ is related to how far away or into an edge the cup: $\bar{P}$ varies more gradually when the cup is fully open ($\bar{P}$ is low) and more dramatically when the cup is mostly covered ($\bar{P}$ is high) [103].

Fig. 4.3 illustrates the piece-wise function that determines c_f. To reduce the number of experimental parameters, values for P_n and P_g were set to 10 Pa and 15 kPa, which are approximately the noise level of $\bar{P}$ and the pressure required to grasp an object, respectively. In Fig. 4.3, $P_{ref} = 100$ Pa and $\beta = 1$, though these factors will be varied in experiments.
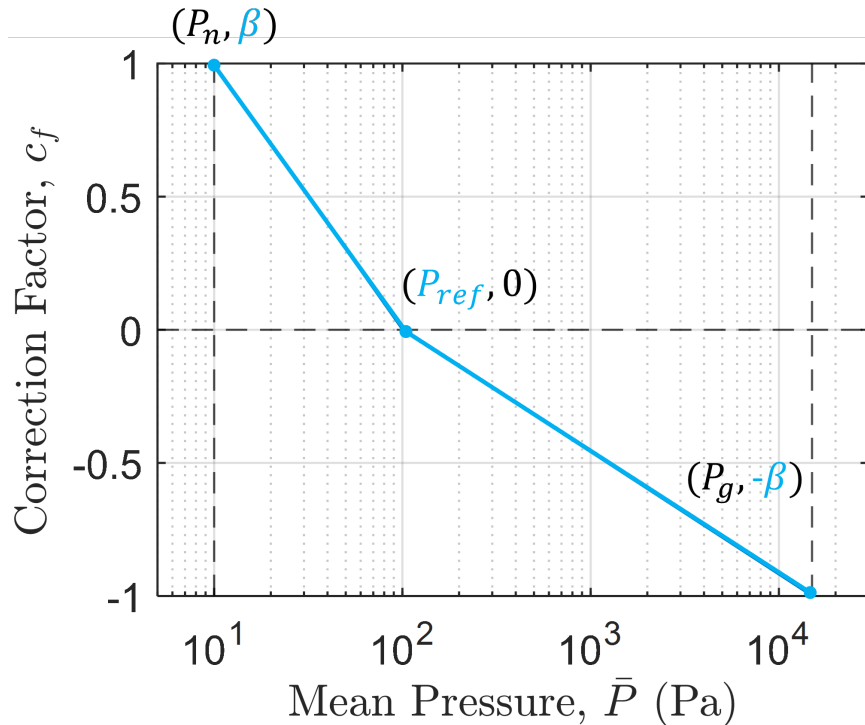
Figure 4.3: **Correction factor as a function of pressure.** When $P < P_{ref}$, the correction factor is positive. When $P > P_{ref}$, the correction factor is negative. Variables in blue are varied in our experiments, while variables in black are fixed.

4.3 Experimental Methods

Robotic System

1) Tactile Sensor: We use a pressure-based tactile sensing suction cup [102]. Fabrication details can be found in our prior work [103]. The latest version of the hardware uses a 3D-printed enclosure (Fig. 4.1b), which houses four pressure sensors (MPRLS, Adafruit), an I2C multiplexer (PCA9546, Adafruit), and a microcontroller (ESP32-S3 feather, Adafruit). The Smart Suction Cup is split into four chambers (Fig. 4.1c). In total, four pressure signals characterize flow differentials across the chambers in the cup and are enough to localize leakage and desired motion direction.

2) Robot Arm: The Smart Suction Cup serves as the end-effector. Its base is bolted to a 6-DoF F/T transducer (Axia80, ATI), which is mounted on a 6-DoF robot arm (UR-10, Universal Robots) as shown in Fig. 4.1a. Transducer normal force is measured and utilized to initialize experiments when the cup first approaches the object to achieve 1.5 N of compression. The arm then controls horizontal motion while maintaining a constant vertical height assuming a flat planar object; the load cell is not used during real-time contour-
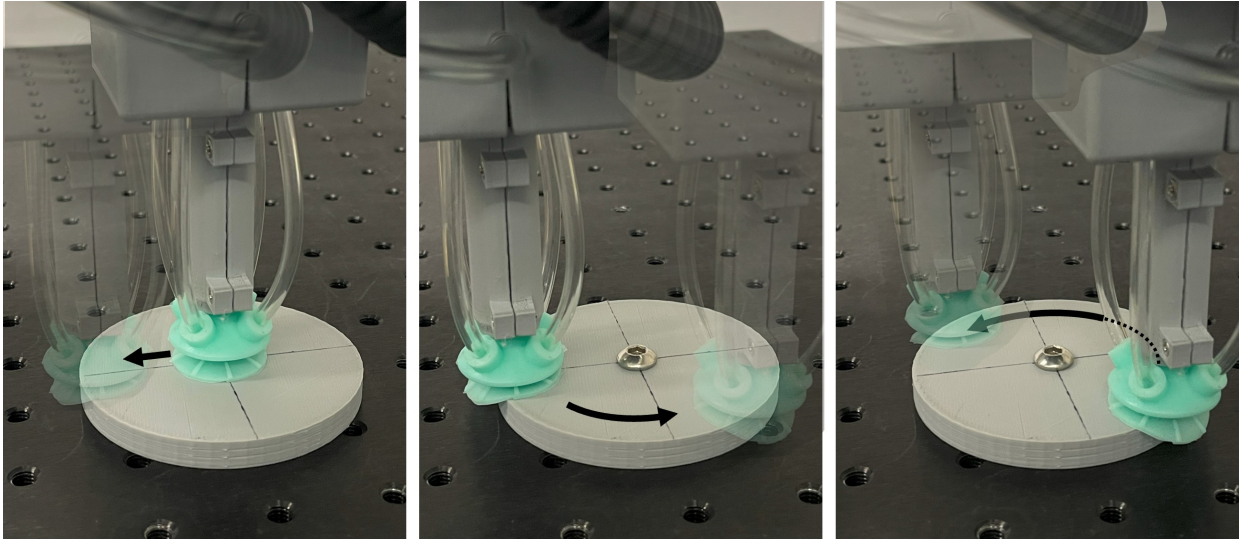
Figure 4.4: **Experimental setup for contour following on a disk.** The cup's position is initialized to the center of the disk to ensure consistency across trials. The trials starts after the cup moves to the edge.

following control. In this study, the experiments are conducted using a desktop computer running on Ubuntu 20.04 and ROS (Noetic).

Controller Benchmarking on a Disk

In order to benchmark the performance of our controllers, contour-following capability is tested on a 35 mm disk (Fig. 4.4). A trial is initialized by bringing the cup to the center of the disk, which ensures consistency across trials. The cup is then moved to the edge of the disk, 32 mm away from the disk's center to ensure an initial condition with sufficient coverage of the cup's chambers. Contour following is arbitrarily chosen to be in the counter-clockwise direction.

We test the effect of three parameters: P_{ref}, β, and step size ΔL. Cup speed is controlled by the step size, ΔL. We expect P_{ref} should correspond to the offset of the edge relative to the suction cup, while β should correspond to how aggressively the cup corrects for offset error. By definition, $|c_f| \leq \beta$, which implies that, when $\beta = 1$, the maximum magnitude of $c_f \hat{\mathbf{v}}_c$ is equal to that of $\hat{\mathbf{v}}$. This also means that the angle between them could be a maximum of 45°. For each triplet of $(P_{ref}, \beta, \Delta L)$ three trials were run and success rate recorded. A successful trial is defined as one complete circumference. We analyze this data set both in terms of this reliability performance metric with speed, but also look at the resulting trajectories of the end-effector.
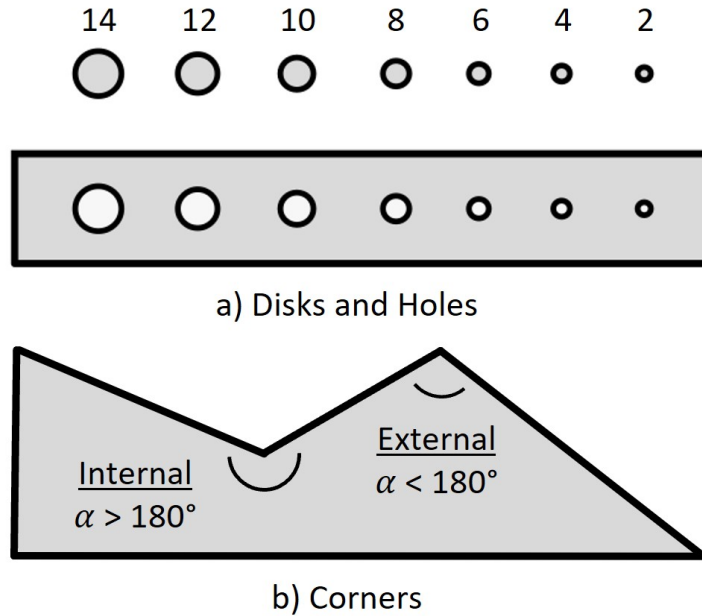
Figure 4.5: **Disks, holes, and corners.** Primitive planar geometries can be characterized by diameter or angle.

Testing on Other Objects

After selecting one promising controller found in our disk benchmarking experiments, we run contour-following trials on different types of geometries to assess the robustness of our system. First, we select primitive planar geometries designed to test the limits of the suction cup's contour-following capability. We initially test disks and holes of differing diameters, from 2 to 14 mm in steps of 2 mm (Fig. 4.5a). Since the cup is able to follow the edge of a 35 mm disk, we are most interested in characterizing the minimum diameter disk and hole.

We then test discontinuous corners between straight edges of varying internal (concave) and external (convex) angles, α, from 0 to 360° (Fig. 4.5b). Angles close to 180° resemble flat edges. Such discontinuities with no connecting curvature can generate signals that yield failures. We then test three compound shapes with varying continuous and/or discontinuous features to test how the prior results translate to more complex shapes. Finally, we perform initial trials on a simple three dimensional filleted edge, where the fillet gradually increases from a zero radius of curvature to 16 mm radius of curvature; we can observe how sharp the edge must be for our method to work.
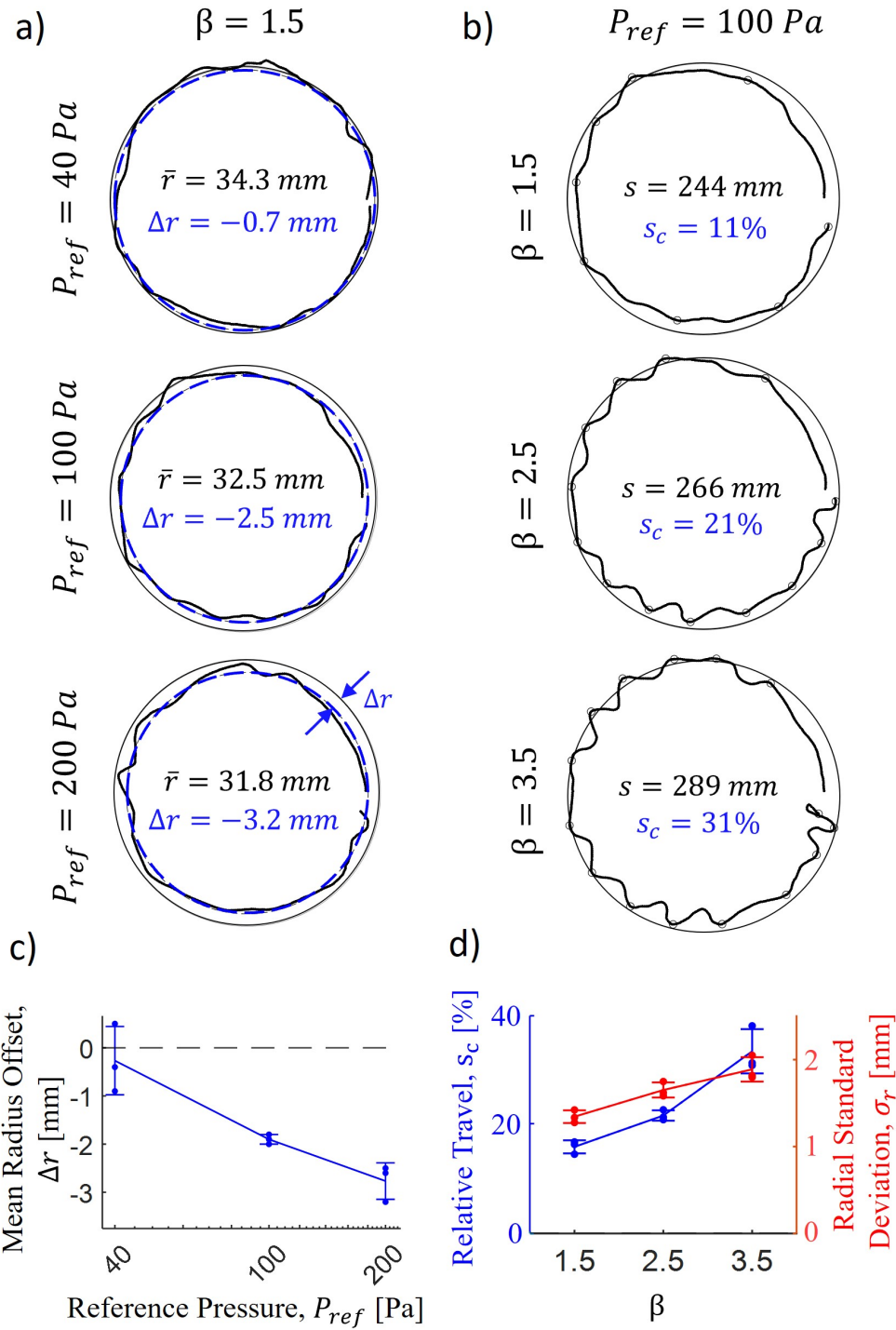
Figure 4.6: **Effect of controller parameters on closed-loop control trajectories.** Three trajectories are plotted for two different conditions. a) P_{ref} is varied while keeping β fixed at 1.5. b) Similarly, β is varied while keeping P_{ref} fixed at 100 Pa. c) As P_{ref} increases, the mean radius offset Δr (difference between disk radius and $\bar{r}$) decreases, resulting in trajectories where the cup is closer to the center of the disk. d) As β increases, both relative travel s_c and radial standard deviation σ_r increase.

4.4   Results

Effect of Controller Parameters on Trajectory

Here, we show and analyze closed-loop trajectories to illustrate the effects of P_{ref} and β. Varying P_{ref} while keeping $\beta = 1.5$ constant (Fig. 4.6a) shows that a higher $P_{ref} = 200$ Pa value biases the trajectory inside the edge of the object. On the other hand, $P_{ref} = 40$ Pa roughly centers the cup on the edge. In order to better understand this effect of P_{ref} on postural bias, we compute each trajectory's mean radius $\bar{r}$ and compare it to the object's radius for all trajectories in Fig. 4.6a Trajectory radii are graphically represented by the dashed circles. Mean radius offset, Δr, plotted across three trials under each condition in Fig. 4.6c, is the difference between $\bar{r}$ and 35 mm, the radius of the disk. At $P_{ref} = 40$ Pa, $\bar{r}$ is 34.3 mm, and $\Delta r = $ -0.7 mm. When $P_{ref} = 200$ Pa, Δr grows to -3.2 mm. As P_{ref} increases, $\bar{r}$ decreases, and the cup covers more of the disk.

Varying β while keeping $P_{ref} = 100$ Pa constant (Fig. 4.6b), shows that this parameter more so affects the trajectory shape than the edge bias; more obvious oscillation appears as β increases from 1.5 to 3.5. Here, we characterise these oscillations using radial standard deviation σ_r, which is the standard deviation of the trajectory's radial distance from the disk's center, and travel distance s, which is the trajectory's path length. At $\beta = 1.5$, $\sigma_r = $ 1.36 mm and $s = 244$ mm, which is 111% of the disk's circumference, C, i.e. relative travel s_c = 11%. At $\beta = 3.5$, s_c increases to 31% and σ_r increases to 1.89 mm. s_c and σ_r are plotted against β in Fig. 4.6d, which shows the average across three trials at each β. Relative travel appears to increase non-linearly with more variability at higher values of β.
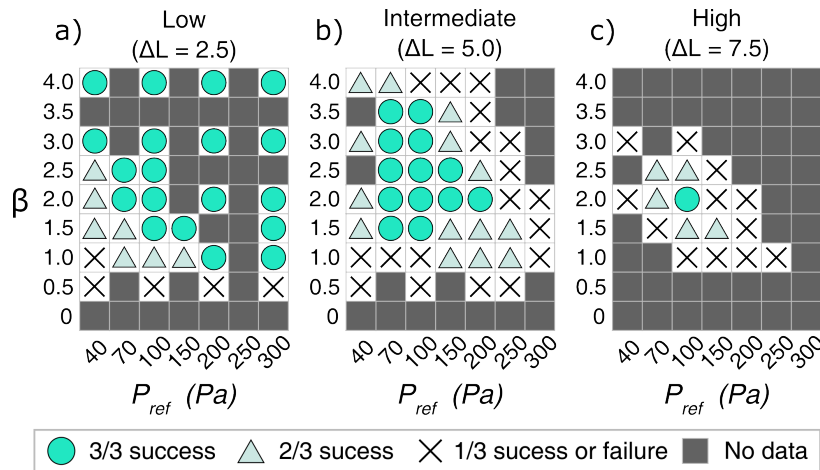
Figure 4.7: **Success rate maps at three different step sizes.** a) 2.5, b) 5.0, and c) 7.5. At each $(P_{ref}, \beta, \Delta L)$ triplet, three attempts were made to follow the edge of a 35 mm disk. Circles represent 100% success rate, triangles represent 66% success, and X's represent low or no success rate. Gray boxes represent points in the parameter space that were not tested.

Disk Contour Following Speed and Reliability

Through pilot studies we find that, when $P_{ref} = 70$ Pa and $\beta = 1.0$, the controller yields successful contour following at the step size of $\Delta L = 2.5$ mm. We consider $\Delta L = 2.5$ mm to be our initial "low" speed and seek to improve speed by tuning the other parameters. Figure 4.7 summarizes how the P_{ref} and β parameters are swept across step sizes ΔL of 2.5 mm ("low"), 5.0 mm ("intermediate"), and 7.5 mm ("high") speeds. P_{ref} is varied to six unique values between the range of $[40, 300]$ Pa, while β could be any multiple of 0.5 within the range $[0, 5.0]$. Success rate is reported for each triplet tested $(P_{ref}, \beta, \Delta L)$. To reduce the number of experiments, a sparse search is conducted; pairs of (P_{ref}, β) are strategically chosen to identify the successful envelope of controller parameters for each speed, which is contoured by low success rates (i.e., the boundary of X's in Fig. 4.7a-c).

The parameter space at the low step size of $\Delta L = 2.5$ mm (~ 1 cm/s) yields high success rates for most combinations of P_{ref} and β. When $\beta > 3.0$, success rate is 100% for all values of P_{ref}. Due to the high reliability of contour following at this speed, the success rate of many parameter combinations are inferred from the sparse search. At the tested step sizes, a $\beta = 0.5$ or less always results in failure. Success rate is lower towards the bottom left corner at this speed; here, the trials terminate due to the cup moving out and away from the edge (Fig. 4.8, Failure Mode I).

The parameter space at the intermediate step size of $\Delta L = 5.0$ mm (~ 2 cm/s) shows a reduction in the size of the success envelope compared to the low step size condition. Success rate notably decreases towards the top right corner at pair ($P_{ref} = 200$ Pa, $\beta = 3.0$); trials in this regime terminate due to the cup moving too far into the surface, resulting in the cup grasping the surface (Fig. 4.8, Failure Mode II).

At the highest step size condition, $\Delta L = 7.5$ mm (~ 3 cm/s), we find that the controller can reliably edge-follow only when $P_{ref} = 100$ Pa and $\beta = 2.0$, i.e. it succeeds in all three trials. These P_{ref} and β settings yield successful contour following at the three tested step sizes, shown in the Supplementary Video. With different P_{ref} and β settings, the controllers at the high step size yield at least one failure. Failures occur both inside and outside of the
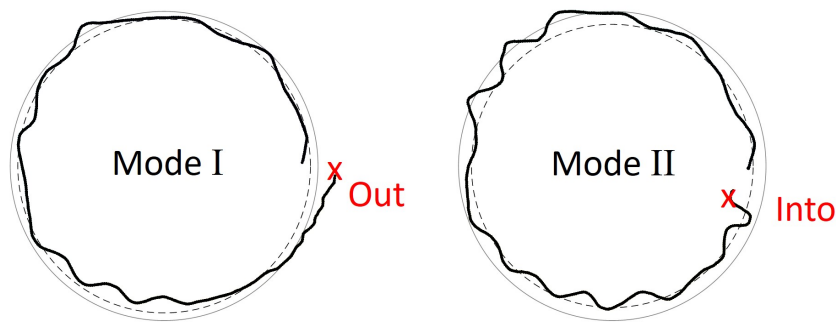
Figure 4.8: **Failure Modes.** I) Out from the disk center and away from the edge. II) Into the disk center and away from the edge.

object (Fig. 4.8a-b). These failure modes occur when $\bar{P}$ falls below the noise level P_n of 10 Pa or exceeds the grasp condition P_g of 15 kPa, rendering an accurate measurement of directionality impossible or leading to full engagement of the surface, respectively.

Performance on Other Planar Geometries

Due to the cup's structure and size, there are limits to how small or large a feature can be before the cup is unable to track its edge. To determine the geometric limits of the cup, contour following is tested on disks and holes of decreasing size as well as sharp internal and external corners. $\Delta L = 0.5$ mm while $P_{ref} = 100$ Pa and $\beta = 2.0$. We find that the cup is able to track a 12 mm diameter disk, but a 10 mm disk proves challenging. The cup is able to track a 2 mm hole, the smallest hole tested. These same controller parameters are tested on convex and concave corners. We find that the suction cup performs well on the edge of external corners with angles α of 15° or greater. However, the cup is unable to successfully follow internal corners greater than 190°.

Beyond primitive features, arcs and corners can be concatenated to form compound geometries. Contour following is tested on three distinct compound geometries: a volute, decreasing semi-circles, and decreasing semi-squares. We find that the Smart Suction Cup successfully follows the edges of these three compound geometries, as seen in Fig. 4.9, and
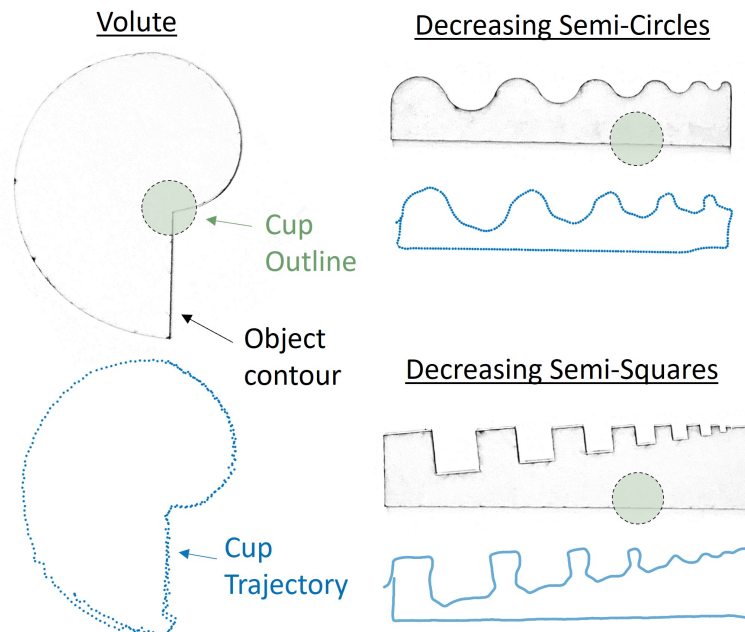
Figure 4.9: **Successful contour following on compound geometries.** Each trajectory is placed below each test object and scaled to the same size. Dashed circles represent the size of the suction cup relative to the shapes.

shown in the Supplementary Video. However, we note that the exact shape of the robot's trajectory is slightly different from the object's shape – this is expected given trajectories observed on earlier disk trials.

Filleted Edge

In addition to simple and compound 2D geometries, we also explore the Smart Suction Cup's ability to follow a filleted edge. To do so, we run contour following on a variable fillet edge (Fig. 4.10). The trials start on the non-filleted portion of the edge and proceed to follow the filleted edge. Cross-sections at various distances along the variable fillet are illustrated in Fig. 4.10a. The maximum fillet radius is 16 mm.

Across five trials, top view trajectories show that the cup's trajectories stays on top of the filleted portion of the edge, which eventually leads to the cup moving out and away from the edge (Fig. 4.10b). The pressure differential drops to zero between 120 mm and 160 mm, with a mean of 137.5 ± 12.7 mm. Therefore, the Smart Suction Cup appears able to follow a fillet with a radius of about 14.5 mm or less.
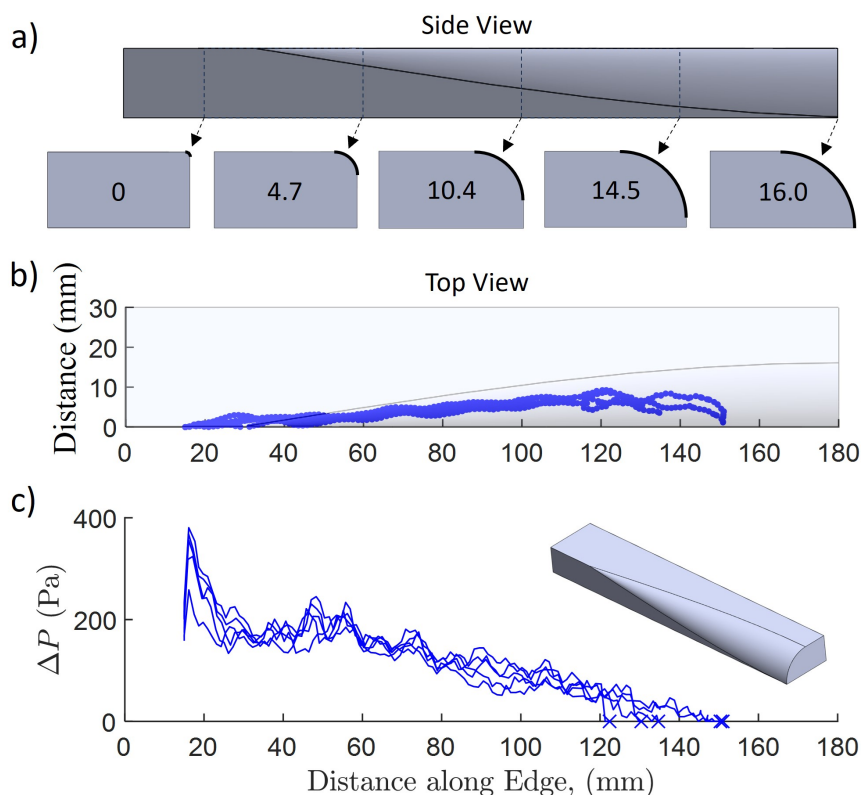
Figure 4.10: **Contour-following trials on a variable 3D fillet.** a) Side view and fillet radius size at given cross-sections. b) Top view trajectory of five trials. c) Pressure differential data goes to zero as fillet size increases.

4.5   Discussion

Understanding Performance on Disk

Through a parameter sweep, we observe success envelopes, as in Fig. 4.7, their size decreasing with larger steps. Shrinking originates from the bottom left and top right corners, where both P_{ref} and β approach their tested limits. In the bottom left corner, decreasing P_{ref} increases $\bar{r}$ (Fig. 4.6a), while decreasing β results in lighter oscillations (Fig. 4.6b); coupled together, they increase the likelihood of the cup veering out (Mode I, Fig. 4.8a). At low P_{ref}, a high β value improves success rate by providing corrections to prevent Failure Mode I. However, at a high step size, β is unable to compensate quickly enough. Biasing the cup into the edge with an intermediate value of P_{ref} therefore helps to prevent Mode I. From the top right corner, the success envelope rapidly shrinks as step size increases, often terminating in Failure Mode II (Fig. 4.8b). As $\bar{r}$ decreases with higher P_{ref}, the cup biases towards the disk center (Fig. 4.6a), while higher β yields stronger oscillations (Fig. 4.6b), increasing trajectory amplitude and the likelihood of over-correcting into the object.

The effects of P_{ref}, β, and ΔL are likely coupled in ways not captured in the present study, warranting further examination. This could also support the development of improved controller methods in future work. For example, to prevent Failure Mode II, vacuum Pulse Width Modulation (PWM) can be triggered when $\bar{P}$ exceeds a threshold, maintaining flow differential without surface grasping, as introduced in [102]. Alternatively, adaptive controller parameters show promise, like reducing step size to slow down the arm speed when $\bar{P}$ is especially high.

Speed and Reliability

We find that the continuous-sliding contour-following policy can yield reliable (3/3 trial successes) and rapid ($\sim$3 cm/s) performance on a disk. Contour following has been demonstrated at various speeds in prior literature. For instance, the TacTip completes one full revolution in 112 s around a 105 mm diameter disk, equivalent to 3.0 mm/s (7.5% s relative to its 40 mm body diameter) [107]. A 12-taxel, capacitive-based tactile sensor reaches 0.7 mm/s [110]. In contrast, our Smart Suction Cup reaches a top speed of 30 mm/s, about 130% s relative to its size, $_{out}$ = 23 mm (Fig. 4.1b). This performance difference may stem from factors like reduced computation time and increased sampling rate afforded by a lower-resolution sensor. Lepora et al., (2022) benchmark DIGIT's [108] and DigiTac's [109] contour-following ability but do not report trial completion times. Using common benchmarking methods, that include execution speed, for standardizing contour following assessment would assist in comparing performance in future work.
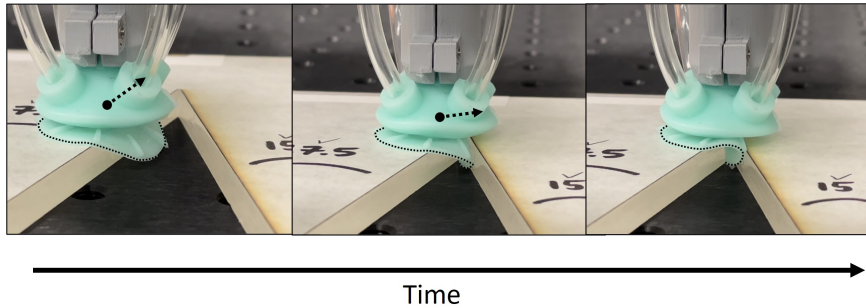
Figure 4.11: **Cup lip crimping.** The sequence of snapshots shows how the cup's lips fold in, resulting in flow blockage that misdirects the cup's motion.

Robustness to Various Geometries

The control policy tested appears robust, as it generalizes to various object geometries. However, one failure mode arises when attempting to navigate internal corners with $\alpha > 190°$: the lip wedges itself into the corner and then folds in on itself, covering the chambers (Fig. 4.11). Consequently, the cup likely cannot fully circumnavigate shapes like a "clover" or a "heart" due to their concave corners. One solution is to detect this failure mode and switch to a hopping controller, as proposed in [103]. Another failure mode occurs with a 10 mm disk, smaller than the cup's internal diameter, $_{in} = 11$ mm (Fig. 4.1c). Due to substantial flow leakage, $\bar{P}$ is insufficient to accurately measure or grasp most objects. Flow leakage diminishes ΔP, leading to less accurate estimation of $\hat{\mathbf{v}}$.

When looking at the compound geometries, our method succeeds on the "decreasing semi-circles" compound object, despite its inability to track the 10 mm disk. This may be because, as observed in Fig. 4.9 for the "decreasing semi-circles" object, the controller disregards and slides past the smallest arc, at the top right corner of the object. The cup behaves similarly with the smallest feature of the "decreasing semi-squares." We also note a distortion effect for almost all object corners, where the cup creates geometric artifacts. This is likely due to unmodeled flow conditions that change as the covered area of the cup varies widely at these intersections. However, this effect does not appear to disrupt the overall contour following task completion and is left as an area for future work.

The cup is able to track a filleted edge as well, but fails as the fillet radius increases. In this study, we keep vertical height constant while moving horizontally. As a result, larger radius fillets lead to a lower ΔP, making it more challenging to estimate $\hat{\mathbf{v}}$. Regulating the applied contact force may partially address this issue, since a higher contact force could increase overall flow blockage and result in a more noticeable flow differential. We plan to study Smart Suction Cup contour following on even more complex 3D geometries in future work.

4.6 Conclusion

This work is the first demonstration of contour following with the Smart Suction Cup. Through parametric studies, we tuned a controller that enable rapid and reliable contour following around a disk. This controller is robust to simple and complex geometries, including arcs and corners, as well as compound shapes and filleted edges. Successful tracing of contours serves as evidence that the Smart Suction Cup is a promising tool for rapid and robust tactile sensing applications. Future work will focus on object recognition and haptic exploration across more complex 3D geometries, addressing challenges in vision-obscured or high-uncertainty scenarios, such as retrieving objects from opaque or cluttered enclosures, or handling transparent and high-glare objects.

Chapter 5

Conclusions and Future Work

5.1 Conclusions

This dissertation explores adaptive control strategies that are possible when gripper contact is nonprehensile. It focuses on two different embodied agents performing two very different tasks: 1) a squirrel landing on a branch and 2) a suction cup haptically searching surfaces. By examining these two systems, I highlight the importance of morphological computation and focus particularly on the crucial role of adaptive control strategies in achieving robust interactions with objects and substrates in the environment.

In Chapter 2, we investigated the adaptive landing strategies of squirrels, directly observing how an exemplary biological system dynamically compensates for positioning errors. Our measurements revealed that squirrels exhibit rapid and precise landings, primarily utilizing their forelimbs to manage landing energy. As landing speed increased, squirrels demonstrate the ability to align velocity and force vectors along their limbs, likely to minimize joint torques for efficiency or to prevent injury. Variability in peak force and torque suggests that squirrels do actively control applied forces to adjust for landing errors. Specifically, we found that squirrels employ substantial braking forces when overshooting, and pull up forces when undershooting. The development of a squirrel-inspired robotic gripper highlighted the role of morphological computation in improving tolerance to positioning errors and energy management. However, this study also underscored the limitations of purely mechanical solutions, emphasizing the need for integrated sensing and adaptive control in robotic systems.

Chapters 3 and 4 introduced the Smart Suction Cup. In Chapter 3, we developed adaptive control strategies that leverage haptic signals to improve grasping success rates. Our controllers were tested on a set of challenging surfaces, specifically on adversarial objects, demonstrating the effectiveness of tactile sensing in enhancing robotic manipulation. Chapter 4 extended the Smart Suction Cup's capabilities. It explored the performance of contour-following, further showcasing the potential of integrating haptic feedback. Through the use of real-time adjustments based on sensory inputs, we show how a robot arm can adapt to objects of varying shapes and curvatures, a crucial ability for real-world applications. These

chapters highlight the synergy between clever mechanical design and sophisticated sensing and control strategies in achieving robust robotic interactions.

This work contributes to bridging the gap highlighted by Moravec's paradox, where tasks that are easy for humans, such as balance or object manipulation, prove challenging for robots. By combining the compliance and adaptability of soft structures with sophisticated sensing and motor control, we're moving closer to robotic systems that can match the dexterity of biological counterparts. The squirrel landing study demonstrates how biological systems seamlessly integrate morphological computation with rapid sensory processing and motor control. Meanwhile, the Smart Suction Cup exemplified how these principles can be applied to robotic systems, enabling them to adapt to varying surface conditions and object geometries. A holistic approach to embodied dexterity, integrating clever mechanical design with real-time sensory feedback and adaptive control, paves the way for more versatile and robust robotic interactions in unstructured environments. This work demonstrates that achieving true embodied dexterity in robotic systems requires not just innovative hardware design, but also the seamless integration of sensing and adaptive control strategies.

5.2 Future Work

Future work should focus on further integrating and refining the concepts explored in this dissertation. One promising direction is the integration of tactile sensors into the squirrel-inspired gripper to improve tolerance to landing errors during dynamic landings. This could involve developing compact, robust tactile sensors that can withstand impact forces and provide rapid feedback for real-time adjustments. Additionally, improving the motion control of the Smart Suction Cup is crucial. Currently, the suction cup lacks the ability to differentiate between scenarios when it should employ rotation, translation, or a combination of both. Future research should address this limitation by incorporating force-torque sensing, estimating suction cup deformation states, or developing models to identify surface curvatures and holes. These enhancements would greatly improve the cup's ability to navigate complex surfaces and adapt to varying geometries.

Beyond these specific improvements, several broader research directions emerge. Further studies of squirrel biomechanics could yield insights into energy management during dynamic maneuvers, potentially informing the design of more energy-efficient robotic systems. The squirrel gripper design could be extended to incorporate variable stiffness mechanisms, allowing for adaptive compliance in different landing scenarios. For the Smart Suction Cup, exploring multi-modal sensing by combining airflow-based tactile sensing with other modalities like deformation estimation could enhance its perceptual capabilities. Additionally, investigating learning algorithms that can optimize the use of morphological computation and sensory feedback in real-time could lead to even more robust and versatile robotic systems. Finally, exploring the application of these principles to other domains of robotics, such as legged locomotion or aerial manipulation, could broaden the impact of this work on embodied dexterity in diverse robotic platforms.

Bibliography

[1] N. H. Hunt, J. Jinn, L. F. Jacobs, and R. J. Full, "Acrobatic squirrels learn to leap and land on tree branches without falling," *Science*, vol. 373, no. 6555, pp. 697–700, 2021.

[2] K. Autumn, Y. A. Liang, S. T. Hsieh, W. Zesch, W. P. Chan, T. W. Kenny, R. Fearing, and R. J. Full, "Adhesive force of a single gecko foot-hair," *Nature*, vol. 405, no. 6787, pp. 681–685, 2000.

[3] Y. Song, Z. Dai, Z. Wang, and R. J. Full, "Role of multiple, adjustable toes in distributed control shown by sideways wall-running in geckos," *Proceedings of the Royal Society B*, vol. 287, no. 1926, p. 20200123, 2020.

[4] M. R. Cutkosky and R. D. Howe, "Human grasp choice and robotic grasp analysis," *Dextrous robot hands*, pp. 5–31, 1990.

[5] E. Pouydebat, G. Boulinguez-Ambroise, A. Manzano, V. Abdala, and D. Sustaita, "Convergent evolution of manual and pedal grasping capabilities in tetrapod s," in *Convergent Evolution: Animal Form and Function*.   Springer, 2023, pp. 323–389.

[6] D. Sustaita, E. Pouydebat, A. Manzano, V. Abdala, F. Hertel, and A. Herrel, "Getting a grip on tetrapod grasping: form, function, and evolution," *Biological Reviews*, vol. 88, no. 2, pp. 380–405, 2013.

[7] M. Graham and J. J. Socha, "Going the distance: The biomechanics of gap-crossing behaviors," *Journal of Experimental Zoology Part A: Ecological and Integrative Physiology*, vol. 333, no. 1, pp. 60–73, 2020.

[8] S. Toussaint, A. Llamosi, L. Morino, and D. Youlatos, "The central role of small vertical substrates for the origin of grasping in early primates," *Current Biology*, vol. 30, no. 9, pp. 1600–1613, 2020.

[9] J. A. Nyakatura, "Early primate evolution: insights into the functional significance of grasping from motion analyses of extant mammals," *Biological Journal of the Linnean Society*, vol. 127, no. 3, pp. 611–631, 2019.

[10] N. T. Dunham, A. McNamara, L. Shapiro, T. Phelps, A. N. Wolfe, and J. W. Young, "Locomotor kinematics of tree squirrels (sciurus carolinensis) in free-ranging and laboratory environments: Implications for primate locomotion and evolution," *Journal of Experimental Zoology Part A: Ecological and Integrative Physiology*, vol. 331, no. 2, pp. 103–119, 2019.

[11] R. L. Essner Jr, "Three-dimensional launch kinematics in leaping, parachuting and gliding squirrels," *Journal of Experimental Biology*, vol. 205, no. 16, pp. 2469–2477, 2002.

[12] J. Wölfer, T. Aschenbach, J. Michel, and J. A. Nyakatura, "Mechanics of arboreal locomotion in swinhoe's striped squirrels: A potential model for early euarchontoglires," *Frontiers in Ecology and Evolution*, vol. 9, p. 636039, 2021.

[13] J. D. Orkin and H. Pontzer, "The narrow niche hypothesis: gray squirrels shed new light on primate origins," *American Journal of Physical Anthropology*, vol. 144, no. 4, pp. 617–624, 2011.

[14] D. Youlatos, "Locomotor and postural behavior of sciurus igniventris and microsciurus flaviventer (rodentia, sciuridae) in eastern ecuador," 1999.

[15] A. Schmidt and M. S. Fischer, "The kinematic consequences of locomotion on sloped arboreal substrates in a generalized (rattus norvegicus) and a specialized (sciurus vulgaris) rodent," *Journal of Experimental Biology*, vol. 214, no. 15, pp. 2544–2559, 2011.

[16] J. W. Young and B. A. Chadwell, "Not all fine-branch locomotion is equal: Grasping morphology determines locomotor performance on narrow supports," *Journal of Human Evolution*, vol. 142, p. 102767, 2020.

[17] T. Feix, J. Romero, H.-B. Schmiedmayer, A. M. Dollar, and D. Kragic, "The grasp taxonomy of human grasp types," *IEEE Transactions on human-machine systems*, vol. 46, no. 1, pp. 66–77, 2015.

[18] G. Boulinguez-Ambroise, N. Dunham, T. Phelps, T. Mazonas, P. Nguyen, M. Bradley-Cronkwright, D. M. Boyer, G. S. Yapuncich, A. Zeininger, D. Schmitt, *et al.*, "Jumping performance in tree squirrels: Insights into primate evolution," *Journal of Human Evolution*, vol. 180, p. 103386, 2023.

[19] G. Byrnes, N. T.-L. Lim, and A. J. Spence, "Take-off and landing kinetics of a free-ranging gliding mammal, the malayan colugo (galeopterus variegatus)," *Proceedings of the Royal Society B: Biological Sciences*, vol. 275, no. 1638, pp. 1007–1013, 2008.

[20] K. E. Paskins, A. Bowyer, W. M. Megill, and J. S. Scheibe, "Take-off and landing forces and the evolution of controlled gliding in northern flying squirrels glaucomys sabrinus," *Journal of Experimental Biology*, vol. 210, no. 8, pp. 1413–1423, 2007.

[21] J. S. Scheibe, K. E. Paskins, S. Ferdous, and D. Birdsill, "Kinematics and functional morphology of leaping, landing, and branch use in glaucomys sabrinus," *Journal of Mammalogy*, vol. 88, no. 4, pp. 850–861, 2007.

[22] D. W. Haldane, M. M. Plecnik, J. K. Yim, and R. S. Fearing, "Robotic vertical jumping agility via series-elastic power modulation," *Science Robotics*, vol. 1, no. 1, p. eaag2048, 2016.

[23] J. K. Yim and R. S. Fearing, "Precision jumping limits from flight-phase control in salto-1p," in *2018 IEEE/RSJ international conference on intelligent robots and systems (IROS)*.   IEEE, 2018, pp. 2229–2236.

[24] J. K. Yim, B. R. P. Singh, E. K. Wang, R. Featherstone, and R. S. Fearing, "Precision robotic leaping and landing using stance-phase balance," *IEEE Robotics and Automation Letters*, vol. 5, no. 2, pp. 3422–3429, 2020.

[25] L. Jin, Y. Yang, B. O. T. Maldonado, S. D. Lee, N. Figueroa, R. J. Full, and S. Yang, "Ultrafast, programmable, and electronics-free soft robots enabled by snapping metacaps," *Advanced Intelligent Systems*, vol. 5, no. 6, p. 2300039, 2023.

[26] J. W. Young, "Convergence of arboreal locomotor specialization: morphological and behavioral solutions for movement on narrow and compliant supports," in *Convergent evolution: Animal form and function*.   Springer, 2023, pp. 289–322.

[27] B. Hesse, J. A. Nyakatura, M. S. Fischer, and M. Schmidt, "Adjustments of limb mechanics in cotton-top tamarins to moderate and steep support orientations: significance for the understanding of early primate evolution," *Journal of Mammalian Evolution*, vol. 22, pp. 435–450, 2015.

[28] A. R. Lammers and T. Gauntner, "Mechanics of torque generation during quadrupedal arboreal locomotion," *Journal of biomechanics*, vol. 41, no. 11, pp. 2388–2395, 2008.

[29] A. Schmidt, "Functional differentiation of trailing and leading forelimbs during locomotion on the ground and on a horizontal branch in the european red squirrel (sciurus vulgaris, rodentia)," *Zoology*, vol. 114, no. 3, pp. 155–164, 2011.

[30] R. H. Bonser, "Branching out in locomotion: the mechanics of perch use in birds and primates," *Journal of Experimental Biology*, vol. 202, no. 11, pp. 1459–1463, 1999.

[31] W. R. Roderick, D. D. Chin, M. R. Cutkosky, and D. Lentink, "Birds land reliably on complex surfaces by adapting their foot-surface interactions upon contact," *Elife*, vol. 8, p. e46415, 2019.

[32] B. Demes, W. L. Jungers, T. Gross, and J. Fleagle, "Kinetics of leaping primates: influence of substrate orientation and compliance," *American Journal of Physical Anthropology*, vol. 96, no. 4, pp. 419–429, 1995.

[33] B. Demes, J. Fleagle, and W. Jungers, "Takeoff and landing forces of leaping strepsirhine primates," *Journal of Human Evolution*, vol. 37, no. 2, pp. 279–292, 1999.

[34] B. Demes, T. M. Franz, and K. J. Carlson, "External forces on the limbs of jumping lemurs at takeoff and landing," *American Journal of Physical Anthropology: The Official Publication of the American Association of Physical Anthropologists*, vol. 128, no. 2, pp. 348–358, 2005.

[35] Z. Zhang, H. Yu, J. Yang, L. Wang, and L. Yang, "How cat lands: insights into contribution of the forelimbs and hindlimbs to attenuating impact force," *Chinese Science Bulletin*, vol. 59, pp. 3325–3332, 2014.

[36] X. Wu, B. Pei, Y. Pei, N. Wu, K. Zhou, Y. Hao, and W. Wang, "Contributions of limb joints to energy absorption during landing in cats," *Applied Bionics and Biomechanics*, vol. 2019, no. 1, p. 3815612, 2019.

[37] Z. Zhang, J. Yang, and H. Yu, "Effect of flexible back on energy absorption during landing in cats: a biomechanical investigation," *Journal of Bionic Engineering*, vol. 11, no. 4, pp. 506–516, 2014.

[38] S. Cox and G. Gillis, "Evidence toads may modulate landing preparation without predicting impact time," *Biology Open*, vol. 6, no. 1, pp. 71–76, 2017.

[39] S. M. Reilly, S. J. Montuelle, A. Schmidt, E. Naylor, M. E. Jorgensen, L. G. Halsey, and R. L. Essner Jr, "Conquering the world in leaps and bounds: hopping locomotion in toads is actually bounding," *Functional Ecology*, vol. 29, no. 10, pp. 1308–1316, 2015.

[40] E. Azizi, N. P. Larson, E. M. Abbott, and N. Danos, "Reduce torques and stick the landing: limb posture during landing in toads," *Journal of Experimental Biology*, vol. 217, no. 20, pp. 3742–3747, 2014.

[41] R. M. Alexander, "Energy-saving mechanisms in walking and running," *Journal of experimental biology*, vol. 160, no. 1, pp. 55–69, 1991.

[42] J. Chen, A. Peattie, K. Autumn, and R. Full, "Differential leg function in a sprawled-posture quadrupedal trotter," *Journal of Experimental Biology*, vol. 209, no. 2, pp. 249–259, 2006.

[43] R. J. Full, R. Blickhan, and L. H. Ting, "Leg design in hexapedal runners," *Journal of Experimental Biology*, vol. 158, no. 1, pp. 369–390, 1991.

[44] B. Wu, I. Akinola, J. Varley, and P. Allen, "Mat: Multi-fingered adaptive tactile grasping via deep reinforcement learning," *arXiv preprint arXiv:1909.04787*, 2019.

[45] P. McKinley, J. Smith, and R. Gregor, "Responses of elbow extensors to landing forces during jump downs in cats," *Experimental Brain Research*, vol. 49, pp. 218–228, 1983.

[46] P. McKinley and J. Smith, "Visual and vestibular contributions to prelanding emg during jump-downs in cats," *Experimental brain research*, vol. 52, pp. 439–448, 1983.

[47] X. Wu, B. Pei, Y. Pei, W. Wang, Y. Hao, and K. Zhou, "How do cats resist landing injury: insights into the multi-level buffering mechanism," *Journal of Bionic Engineering*, vol. 17, pp. 600–610, 2020.

[48] W. Lu, Q. Zhang, F. Qin, P. Xu, Q. Chen, H. Wang, F. Scarpa, and H.-X. Peng, "Hierarchical network structural composites for extraordinary energy dissipation inspired by the cat paw," *Applied Materials Today*, vol. 25, p. 101222, 2021.

[49] D. Xu, H. Zhou, X. Jiang, S. Li, Q. Zhang, J. S. Baker, and Y. Gu, "New insights for the design of bionic robots: adaptive motion adjustment strategies during feline landings," *Frontiers in Veterinary Science*, vol. 9, p. 836043, 2022.

[50] P. Provini, B. W. Tobalske, K. E. Crandell, and A. Abourachid, "Transition from wing to leg forces during landing in birds," *Journal of Experimental Biology*, vol. 217, no. 15, pp. 2659–2666, 2014.

[51] W. R. Roderick, M. R. Cutkosky, and D. Lentink, "Bird-inspired dynamic grasping and perching in arboreal environments," *Science Robotics*, vol. 6, no. 61, p. eabj7562, 2021.

[52] J. E. Seipel, P. J. Holmes, and R. J. Full, "Dynamics and stability of insect locomotion: a hexapedal model for horizontal plane motions," *Biological cybernetics*, vol. 91, no. 2, pp. 76–90, 2004.

[53] H. Geyer, A. Seyfarth, and R. Blickhan, "Spring-mass running: simple approximate solution and application to gait stability," *Journal of theoretical biology*, vol. 232, no. 3, pp. 315–328, 2005.

[54] R. Blickhan and R. Full, "Similarity in multilegged locomotion: bouncing like a monopode," *Journal of Comparative Physiology A*, vol. 173, pp. 509–517, 1993.

[55] M. Raibert, M. Chepponis, and H. Brown, "Running on four legs as though they were one," *IEEE Journal on Robotics and Automation*, vol. 2, no. 2, pp. 70–82, 1986.

[56] T. McGeer, "Passive dynamic walking," *The international journal of robotics research*, vol. 9, no. 2, pp. 62–82, 1990.

[57] S. Nauwelaerts and P. Aerts, "Take-off and landing forces in jumping frogs," *Journal of Experimental Biology*, vol. 209, no. 1, pp. 66–77, 2006.

[58] S. Yang, H. Chen, L. Zhang, Z. Cao, P. M. Wensing, Y. Liu, J. Pang, and W. Zhang, "Reachability-based push recovery for humanoid robots with variable-height inverted pendulum," in *2021 IEEE International Conference on Robotics and Automation (ICRA)*. IEEE, 2021, pp. 3054–3060.

[59] B. J. Van Hofslot, R. Griffin, S. Bertrand, and J. Pratt, "Balancing using vertical center-of-mass motion: A 2-d analysis from model to robot," *IEEE Robotics and Automation Letters*, vol. 4, no. 4, pp. 3247–3254, 2019.

[60] D. E. Orin, A. Goswami, and S.-H. Lee, "Centroidal dynamics of a humanoid robot," *Autonomous robots*, vol. 35, pp. 161–176, 2013.

[61] S.-H. Lee and A. Goswami, "A momentum-based balance controller for humanoid robots on non-level and non-stationary ground," *Autonomous Robots*, vol. 33, pp. 399–414, 2012.

[62] M. CARTMILL, "2 - pads and claws in arboreal locomotion," in *Primate Locomotion*, F. A. JENKINS, Ed. Academic Press, 1974, pp. 45–83.

[63] D. Kuang, S. Wang, S. Lee, L. Wang, and R. Full, "Kinematic paw adjustments of fox squirrels landing on curved surfaces," in *Society of Integrative and Comparative Biology Annual Meeting Exhibition Final Program and Abstracts*, 2023.

[64] D. Kosarov, "The reaction time of single motor units in the human muscle," *Agressologie*, vol. 20, no. 5, pp. 279–285, 1979.

[65] L. Birglen, T. Laliberté, and C. M. Gosselin, *Underactuated robotic hands*. Springer, 2007, vol. 40.

[66] R. Zufferey, J. Tormo-Barbero, D. Feliu-Talegón, S. R. Nekoo, J. Á. Acosta, and A. Ollero, "How ornithopters can perch autonomously on a branch," *Nature Communications*, vol. 13, no. 1, p. 7713, 2022.

[67] T. G. Chen, K. A. Hoffmann, J. E. Low, K. Nagami, D. Lentink, and M. R. Cutkosky, "Aerial grasping and the velocity sufficiency region," *IEEE Robotics and Automation Letters*, vol. 7, no. 4, pp. 10 009–10 016, 2022.

[68] J. Thomas, J. Polin, K. Sreenath, and V. Kumar, "Avian-inspired grasping for quadrotor micro uavs," in *International Design Engineering Technical Conferences and Computers and Information in Engineering Conference*, vol. 55935. American Society of Mechanical Engineers, 2013, p. V06AT07A014.

[69] A. Agrawal, S. Chen, A. Rai, and K. Sreenath, "Vision-aided dynamic quadrupedal locomotion on discrete terrain using motion libraries," in *2022 International Conference on Robotics and Automation (ICRA)*. IEEE, 2022, pp. 4708–4714.

[70] C. Gonzalez, V. Barasuol, M. Frigerio, R. Featherstone, D. G. Caldwell, and C. Semini, "Line walking and balancing for legged robots with point feet," in *2020 IEEE/RSJ International Conference on Intelligent Robots and Systems (IROS)*. IEEE, 2020, pp. 3649–3656.

[71] Q. Nguyen, M. J. Powell, B. Katz, J. Di Carlo, and S. Kim, "Optimized jumping on the mit cheetah 3 robot," in *2019 International Conference on Robotics and Automation (ICRA)*. IEEE, 2019, pp. 7448–7454.

[72] S. H. Jeon, S. Kim, and D. Kim, "Online optimal landing control of the mit mini cheetah," in *2022 International Conference on Robotics and Automation (ICRA)*. IEEE, 2022, pp. 178–184.

[73] P. Manoonpong, H. Rajabi, J. C. Larsen, S. S. Raoufi, N. Asawalertsak, J. Homchanthanakul, H. T. Tramsen, A. Darvizeh, and S. N. Gorb, "Fin ray crossbeam angles for efficient foot design for energy-efficient robot locomotion," *Advanced Intelligent Systems*, vol. 4, no. 1, p. 2100133, 2022.

[74] S. Rozen-Levy, W. Messner, and B. A. Trimmer, "The design and development of branch bot: a branch-crawling, caterpillar-inspired, soft robot," *The International Journal of Robotics Research*, vol. 40, no. 1, pp. 24–36, 2021.

[75] A. Chatterjee, A. Mo, B. Kiss, E. C. Gönen, and A. Badri-Spröwitz, "Multi-segmented adaptive feet for versatile legged locomotion in natural terrain," in *2023 IEEE International Conference on Robotics and Automation (ICRA)*. IEEE, 2023, pp. 1162–1169.

[76] S. J. Wang, D. Kuang, S. D. Lee, R. J. Full, and H. S. Stuart, "Squirrel-inspired tendon-driven passive gripper for agile landing," *IEEE (ICRA)*, 2024.

[77] T. M. Huh, K. Sanders, M. Danielczuk, M. Li, Y. Chen, K. Goldberg, and H. S. Stuart, "A multi-chamber smart suction cup for adaptive gripping and haptic exploration," in *2021 IEEE/RSJ International Conference on Intelligent Robots and Systems (IROS)*. IEEE, 2021, pp. 1786–1793.

[78] D. Morrison, A. W. Tow, M. Mctaggart, R. Smith, N. Kelly-Boxall, S. Wade-Mccue, J. Erskine, R. Grinover, A. Gurman, T. Hunn, *et al.*, "Cartman: The low-cost cartesian manipulator that won the amazon robotics challenge," in *2018 IEEE International Conference on Robotics and Automation (ICRA)*. IEEE, 2018, pp. 7757–7764.

[79] A. Zeng, S. Song, K.-T. Yu, E. Donlon, F. R. Hogan, M. Bauza, D. Ma, O. Taylor, M. Liu, E. Romo, *et al.*, "Robotic pick-and-place of novel objects in clutter with multi-affordance grasping and cross-domain image matching," *The International Journal of Robotics Research*, vol. 41, no. 7, pp. 690–705, 2022.

[80] W. Wan, K. Harada, and F. Kanehiro, "Planning grasps with suction cups and parallel grippers using superimposed segmentation of object meshes," *IEEE Transactions on Robotics*, vol. 37, no. 1, pp. 166–184, 2020.

[81] J. Mahler, M. Matl, X. Liu, A. Li, D. Gealy, and K. Goldberg, "Dex-net 3.0: Computing robust vacuum suction grasp targets in point clouds using a new analytic model and deep learning," in *2018 IEEE International Conference on robotics and automation (ICRA)*. IEEE, 2018, pp. 5620–5627.

[82] H. Cao, H.-S. Fang, W. Liu, and C. Lu, "Suctionnet-1billion: A large-scale benchmark for suction grasping," *IEEE Robotics and Automation Letters*, vol. 6, no. 4, pp. 8718–8725, 2021.

[83] Q. Shao, J. Hu, W. Wang, Y. Fang, W. Liu, J. Qi, and J. Ma, "Suction grasp region prediction using self-supervised learning for object picking in dense clutter," in *2019 IEEE 5th International Conference on Mechatronics System and Robots (ICMSR)*. IEEE, 2019, pp. 7–12.

[84] H.-G. Cao, W. Zeng, and I.-C. Wu, "Reinforcement learning for picking cluttered general objects with dense object descriptors," in *2022 International Conference on Robotics and Automation (ICRA)*. IEEE, 2022, pp. 6358–6364.

[85] S. Aoyagi, M. Suzuki, T. Morita, T. Takahashi, and H. Takise, "Bellows suction cup equipped with force sensing ability by direct coating thin-film resistor for vacuum type robotic hand," *IEEE/ASME Transactions on Mechatronics*, vol. 25, no. 5, pp. 2501–2512, 2020.

[86] H. J. Lee, S. Baik, G. W. Hwang, J. H. Song, D. W. Kim, B.-y. Park, H. Min, J. K. Kim, J.-s. Koh, T.-H. Yang, *et al.*, "An electronically perceptive bioinspired soft wet-adhesion actuator with carbon nanotube-based strain sensors," *ACS nano*, vol. 15, no. 9, pp. 14 137–14 148, 2021.

[87] E. Shahabi, F. Visentin, A. Mondini, and B. Mazzolai, "Octopus-inspired suction cups with embedded strain sensors for object recognition," *Advanced Intelligent Systems*, vol. 5, no. 2, p. 2200201, 2023.

[88] S. Doi, H. Koga, T. Seki, and Y. Okuno, "Novel proximity sensor for realizing tactile sense in suction cups," in *2020 IEEE International Conference on Robotics and Automation (ICRA)*. IEEE, 2020, pp. 638–643.

[89] S. Sareh, K. Althoefer, M. Li, Y. Noh, F. Tramacere, P. Sareh, B. Mazzolai, and M. Kovac, "Anchoring like octopus: biologically inspired soft artificial sucker," *Journal of the royal society interface*, vol. 14, no. 135, p. 20170395, 2017.

[90] S. T. Frey, A. T. Haque, R. Tutika, E. V. Krotz, C. Lee, C. B. Haverkamp, E. J. Markvicka, and M. D. Bartlett, "Octopus-inspired adhesive skins for intelligent and rapidly switchable underwater adhesion," *Science Advances*, vol. 8, no. 28, p. eabq1905, 2022.

[91] V. Müller, T.-L. Lam, and N. Elkmann, "Sensor design and model-based tactile feature recognition," in *2017 IEEE SENSORS*. IEEE, 2017, pp. 1–3.

[92] C. Eppner, S. Höfer, R. Jonschkowski, R. Martín-Martín, A. Sieverling, V. Wall, and O. Brock, "Lessons from the amazon picking challenge: Four aspects of building robotic systems." pp. 4831–4835, 2016.

[93] J. M. Romano, K. Hsiao, G. Niemeyer, S. Chitta, and K. J. Kuchenbecker, "Human-inspired robotic grasp control with tactile sensing," *IEEE Transactions on Robotics*, vol. 27, no. 6, pp. 1067–1079, 2011.

[94] K. Hang, M. Li, J. A. Stork, Y. Bekiroglu, F. T. Pokorny, A. Billard, and D. Kragic, "Hierarchical fingertip space: A unified framework for grasp planning and in-hand grasp adaptation," *IEEE Transactions on robotics*, vol. 32, no. 4, pp. 960–972, 2016.

[95] Y. Chebotar, K. Hausman, Z. Su, G. S. Sukhatme, and S. Schaal, "Self-supervised regrasping using spatio-temporal tactile features and reinforcement learning," in *2016 IEEE/RSJ International Conference on Intelligent Robots and Systems (IROS)*. IEEE, 2016, pp. 1960–1966.

[96] F. R. Hogan, M. Bauza, O. Canal, E. Donlon, and A. Rodriguez, "Tactile regrasp: Grasp adjustments via simulated tactile transformations," in *2018 IEEE/RSJ International Conference on Intelligent Robots and Systems (IROS)*. IEEE, 2018, pp. 2963–2970.

[97] R. Calandra, A. Owens, D. Jayaraman, J. Lin, W. Yuan, J. Malik, E. H. Adelson, and S. Levine, "More than a feeling: Learning to grasp and regrasp using vision and touch," *IEEE Robotics and Automation Letters*, vol. 3, no. 4, pp. 3300–3307, 2018.

[98] J. Mahler, M. Matl, V. Satish, M. Danielczuk, B. DeRose, S. McKinley, and K. Goldberg, "Learning ambidextrous robot grasping policies," *Science Robotics*, vol. 4, no. 26, p. eaau4984, 2019.

[99] V. Satish, J. Mahler, and K. Goldberg, "On-policy dataset synthesis for learning robot grasping policies using fully convolutional deep networks," *IEEE Robotics and Automation Letters*, 2019.

[100] K. Sanders, M. Danielczuk, J. Mahler, A. Tanwani, and K. Goldberg, "Non-markov policies to reduce sequential failures in robot bin picking," in *2020 IEEE 16th International Conference on Automation Science and Engineering (CASE)*. IEEE, 2020, pp. 1141–1148.

[101] S. Dasari, F. Ebert, S. Tian, S. Nair, B. Bucher, K. Schmeckpeper, S. Singh, S. Levine, and C. Finn, "Robonet: Large-scale multi-robot learning," *arXiv preprint arXiv:1910.11215*, 2019.

[102] T. M. Huh, K. Sanders, M. Danielczuk, M. Li, Y. Chen, K. Goldberg, and H. S. Stuart, "A multi-chamber smart suction cup for adaptive gripping and haptic exploration," in *2021 IEEE/RSJ International Conference on Intelligent Robots and Systems (IROS)*. IEEE, 2021, pp. 1786–1793.

[103] J. Lee, S. D. Lee, T. M. Huh, and H. S. Stuart, "Haptic search with the smart suction cup on adversarial objects," *IEEE Transactions on Robotics*, 2023.

[104] M. A. Plaisier, W. M. Bergmann Tiest, and A. M. Kappers, "Salient features in 3-d haptic shape perception," *Attention, Perception, & Psychophysics*, vol. 71, no. 2, pp. 421–430, 2009.

[105] S. J. Lederman and R. L. Klatzky, "Hand movements: A window into haptic object recognition," *Cognitive psychology*, vol. 19, no. 3, pp. 342–368, 1987.

[106] N. F. Lepora, K. Aquilina, and L. Cramphorn, "Exploratory tactile servoing with active touch," *IEEE Robotics and Automation Letters*, vol. 2, no. 2, pp. 1156–1163, 2017.

[107] N. F. Lepora, A. Church, C. De Kerckhove, R. Hadsell, and J. Lloyd, "From pixels to percepts: Highly robust edge perception and contour following using deep learning and an optical biomimetic tactile sensor," *IEEE Robotics and Automation Letters*, vol. 4, no. 2, pp. 2101–2107, 2019.

[108] M. Lambeta, P.-W. Chou, S. Tian, B. Yang, B. Maloon, V. R. Most, D. Stroud, R. Santos, A. Byagowi, G. Kammerer, *et al.*, "Digit: A novel design for a low-cost compact high-resolution tactile sensor with application to in-hand manipulation," *IEEE Robotics and Automation Letters*, vol. 5, no. 3, pp. 3838–3845, 2020.

[109] N. F. Lepora, Y. Lin, B. Money-Coomes, and J. Lloyd, "Digitac: A digit-tactip hybrid tactile sensor for comparing low-cost high-resolution robot touch," *IEEE Robotics and Automation Letters*, vol. 7, no. 4, pp. 9382–9388, 2022.

[110] U. Martinez-Hernandez, G. Metta, T. J. Dodd, T. J. Prescott, L. Natale, and N. F. Lepora, "Active contour following to explore object shape with robot touch," in *2013 World Haptics Conference (WHC)*. IEEE, 2013, pp. 341–346.